AN INVESTIGATION OF A SCALABLE FLIGHT CONTROL SYSTEM FOR A VARIABLE PITCH, FUEL POWERED, QUAD-ROTOR CRAFT

Submitted in the fulfilment of requirements of the degree of Master of Mechanical Engineering in the Faculty of Engineering and the Built Environment at Durban University of Technology

BYRON VAUGHN ROY NIELSEN

NOVEMBER 2023

Supervisor: Dr. M. Gilpin Date: 16 / 04 / 2024

Co–Supervisor: Dr. F. Ghayhoor Date: 16 / 04 / 2024

DECLARATION

I hereby declare that this investigation of a scalable flight control system for a variable pitch, fuel powdered, quad-rotor craft has been submitted in the fulfilment of the degree of the Master of Engineering Mechanical in the Faculty of Engineering and the Built Environment at Durban University of Technology.

I further declare that the report is my own work and that all the sources that were used or quoted, were given recognition by means of a complete reference.

BVR Nielsen

Signature

2024/04/15

Date

Mark Gilpin (Supervisor)

ACKNOWLEDGEMENTS

I would like to extend my heartfelt gratitude to my supervisors, Dr Mark Gilpin, and Dr Fahzad Ghayhoor, for their invaluable contributions and time invested in this work. Without their unwavering support and guidance, the realization of this project would have been unattainable. Thank you for making this endeavour possible.

ABSTRACT

Quadrotor platforms continue to face scalability issues that can be linked to factors such as energy density of polymer battery power sources and the limited efficiency of their fixed pitch propulsion systems.

This study employs a dual-method analysis, integrating both experimental and theoretical approaches, to explore the trade-offs between endurance and payload capacity in a quadrotor equipped with a scalable variable pitch rotor system. By applying this development framework, the key objective of this work is to broaden the scope of feasible mission profiles by clarifying the inherent constraints and compromises between endurance and payload capacity and illuminating factors contributing to efficiency.

In this pursuit, the first main aspect focused on empirically validating various rotor geometries using test bench system. Data collected is analysed using the computational tool MATLAB, whereas XFOIL simulates airfoil lift and drag characteristics. Rotor performance is then characterised through comparative analysis between experimental data and theoretical predictions made by the Blade Element Momentum Theory (BEMT) rotor model. From comparisons it was found that the BEMT model performance and behaviour remained consistent at varying rotor geometry scales and correlated well with empirical thrust results. It was also found that approximations for power output levels were marginally overestimated at high blade pitch angles – the possible causes of which are further explored in an article published in parallel to this work. [1]

The 6-DOF (degrees of freedom) nature of quadrotors in a dynamic environment is then explored using Simulink wherein a flight control system (FCS) architecture is formulated by integrating control laws with a BEMT rotor model. Comparative performance evaluations focusing on dynamic behaviour, thrust generation, and power efficiency are then realised by subjecting a standardised quadrotor airframe with varying rotor geometry and payload capacities to an idealized climb-to-hover (C2H) trajectory.

From comparisons of simulation tests, it was significant to find that varying rotor geometry and payloads yielded highly contrasting dynamic behaviours and efficiency performance in terms of thrust generation and power demands. Simulation data also indicated that the B04 rotor configuration was the most energy efficient and enabled superior climb rates and accelerations. By employing figures for simulated hovering power demands, abstracted endurance times are

shown to be greatly affected by the energy density and payload constraints between chemical battery systems and carbon fuels. Comparative analysis of rotor performance also revealed that the choice of hardware configuration may necessitate prioritising durability and responsiveness over efficiency. Moreover, mission profiles optimised for high dynamic responsiveness must ensure that FCS sensitivity does not exceed the strength constraints of mechanical subsystems or airframe structure.

Collectively, this work successfully established a robust framework for future research and early-stage development of scalable quadrotor platforms can be achieved by integrating variable pitch rotor systems with modularized quadrotor control system architectures. This framework provided key insights into improving quadrotor performance and efficiency, particularly through scalable rotor geometry and payload capacity.

TABLE OF CONTENTS

DECLARATION **ii**

ACKNOWLEDGEMENTS **iii**

ABSTRACT **iv**

TABLE OF CONTENTS **vi**

LIST OF TABLES **x**

LIST OF FIGURES **xi**

NOMENCLATURE **xiii**

1. INTRODUCTION **14**

1.1. Overview Of Rotorcraft Types and Applications 16

1.1.1. Conventional Single-Rotor Craft 16

1.1.2. Quadrotor Platforms 16

1.2. Research Problems & Aims 19

1.2.1. Energy Density 20

1.2.2. Payload Capacity and Scalability 20

1.2.3. Rotor Propulsion Efficiency 21

1.2.4. Control System Scalability 23

1.2.5. Use Cases – Life Preservation 23

1.3. Research Framework & Methodology 24

2. QUADROTOR CONTROL MODELLING **26**

2.1. Orientation & Translation of Fixed Pitch Quadrotors 26

2.2. Orientation & Translation of Variable Pitch Quadrotors 27

2.3. Newton-Euler Equations for X-Type Quadrotors 28

2.3.1. Coordinate Rotation Matrix 28

2.3.2. Linear And Angular Velocity Transformation 29

2.3.3. Quadrotor Dynamics 29

3. ROTOR AERODYNAMICS MODELLING **31**

3.1. Blade Element Momentum Theory (BEMT) 31
3.2. Rotor Solidity, Inflow Velocity, Lift Slope and Blade Area 32
3.3. Airfoil Analysis 32
3.3.1. Ground Effect 33
3.4. Conservation Of Angular Momentum 33
4. ROTOR PERFORMANCE CHARACTERIZATION 35
4.1. Rotor Test System 36
4.1.1. Technical Description & Specifications 37
4.1.2. Rotor Blade Specifications 38
4.1.3. Test Bench Control Circuit 39
4.1.4. Operational Principles 39
4.1.5. Collective Pitch Measurement & Calibration 40
4.1.6. Voltage and Current Measurement & Sensor Calibration 41
4.1.7. Rotor RPM Measurement & Calibration 44
4.1.8. Thrust Measurement & Load Cell Calibration 44
4.2. Test Methodology & Data Processing Workflow 46
4.2.1. Test Sample Collection 46
4.2.2. Initial Rotor Power Output 46
4.2.3. Sample Pre-Processing and Signal Conditioning 48
4.3. XFOIL Airfoil Analysis 50
4.4. Rotor Modelling 52
4.5. Performance Comparisons – BEMT Vs. Experiments 53
4.5.1. Thrust Comparison 55
4.5.2. Power Output Comparison 55
5. MODELLING & SIMULATION 56
5.1. Body Forces & Angular States 58
5.1.1. Body Forces 58
5.1.2. Actuator Forces 60
5.1.3. Angular Displacement, Velocity & Acceleration 62

5.2. Axis Coordinate Transformations & Linear States 64
5.3. Flight Control System (FCS) 65
5.3.1. PID Control 67
5.3.2. FCS Output States 68
6. EVALUATION AND IMPLEMENTATION 70
6.1. Evaluation Framework & Scope 70
6.1.1. Performance Criteria Identification 70
6.1.2. Evaluation Aims & Analysis Scope 70
6.2. Evaluation Methodology 71
6.2.1. Flight Trajectory Generation 71
6.2.2. Boundary Conditions, Simulink Settings & Nomenclature 73
6.3. Simulation Results 73
6.3.1. Dynamic Performance 74
6.3.2. Thrust Performance 75
6.3.3. Power Consumption & Efficiency 76
7. DISCUSSION 80
7.1. Power System Selection 80
7.2. Geometry Considerations and Application Scope 81
7.3. PID Control Response Vs Acceleration 82
8. CONCLUSION 83
8.1. Empirical Validation of Models and Simulations 83
8.2. Rotor Geometry Affects Efficiency. 84
8.3. Control System Scalability 85
8.4. Considerations and Opportunities for Future Work 85
REFERENCES 87
Appendix A: XFOIL LIFT & DRAG 91
Appendix B: ROTOR PERFORMANCE COMPARISON, B03 92
Appendix C: ROTOR PERFORMANCE COMPARISON, B04 93

Appendix F: DYNAMIC PERFORMANCE, TEST SCENARIO 2 **94**

Appendix G: THRUST AND POWER OUTPUT, TEST SCENARIO 2 **95**

Appendix H: POWER OUTPUT COMPARISON, TEST SCENARIO 2 **96**

APPENDIX I: PROPERTIES OF ROTOR SYSTEMS CALCULATED IN SOLIDWORKS **97**

Appendix J: PROPERTIES OF AIRFRAMES CALCULATED IN SOLIDWORKS **98**

Appendix K: SIMULING PID AUTO-TUNER ILLUSTRATION **99**

LIST OF TABLES

Table 1.1: Type Classification 18
Table 4.1: Rotor Bench Specifications Overview 37
Table 4.2: Rotor Blade Specifications 38
Table 4.3: Pitch Angle Interpolation 40
Table 4.4: WCS1500 Specifications Overview 42
Table 4.5: MAUCH HS-200-HV Specifications 42
Table 4.6: MAVIN NA-50 Specifications Overview 45
Table 4.7: T-Motor V10L Motor Constants [65] 47
Table 4.8: Initial Power Consumption 48
Table 4.9: Rotor Blade B02, N$r = 3000rpm, Pini \ = 249.04W$ 48
Table 5.1: Thrust and Moment Equations, Fixed Pitch Vs Varaible Pitch 59
Table 5.2: Linearized Equations Of Moiton 60
Table 5.3: Actuator Force Equations 61
Table 5.4: Linearized Equations for Angular Motion 63
Table 5.5: Linearized Equations of Linear Motion 65
Table 6.1: Summarized Simulation Results 74

LIST OF FIGURES

Figure 1.1: Single Rotorcraft System [9] 16
Figure 1.2: DJI Air 2S [10] 17
Figure 1.3: Quadrotor Forces & Moments 18
Figure 1.4: Fixed Pitch Propeller Efficiency [30] 22
Figure 2.1: Quadrotor Interial & Body Frames [53] 26
Figure 4.1: Test & Sample Processing Methodology 35
Figure 4.2: Rotor Test Bench 36
Figure 4.3: Rotor Test Bench 37
Figure 4.4: Rotor Blade Geometry 38
Figure 4.5: Illustration Of The Rotor Bench Control System 39
Figure 4.6: Rotor Test Bench Free Body Diagram 39
Figure 4.7: Collective Pitch Dial Guage 40
Figure 4.8: Winson WCS1500 [58] 41
Figure 4.9: MAUCH HS-200-HV [59] 42
Figure 4.10: MAVIN NA-50 Load Cell [63] 45
Figure 4.11: inital Power Consumption 47
Figure 4.12: Thrust & Power VS Pitch Angle 50
Figure 4.13: XFOIL Analysis Illustrative Workflow 51
Figure 4.14: XFOIL Lift & Drag Polar Accumulation Plots 52
Figure 4.15: MATLAB Modelling Illustrative Workflow 53
Figure 4.16: Rotor Performance Comparison, B05 54
Figure 5.1: Control System Architecture Overview 56
Figure 5.2: Simulink Control System Model 57
Figure 5.3: Simulink Body Force Model 58
Figure 5.4: Quadrotor Motion & Orientation 59
Figure 5.5: Simulink Actuator Force Model 61
Figure 5.6: Simulink Angular Acceleration Model 62
Figure 5.7: Simulink Airframe Inertia Model 64
Figure 5.8: Simulink Linear State Model 64
Figure 5.9: Simulink Flight Controller 66
Figure 5.10: Simulink Trajectory Generation [68] 66
Figure 5.11: PID Controller Illustration [69] 67

Figure 5.12: Simulink PID Control Block [70] 68
Figure 6.1: Simulated Climb Trajectory 72
Figure 6.2: Dynamic Performance, Test Scenario 1 74
Figure 6.3: Thrust And Power Output, T1 75
Figure 6.4: Variation of rotor power demand to forward flight speed [14] 77
Figure 6.5: Power Output Comparison, T1 78
Figure 6.6: Power Per Unit Mass Comparison for Climb & Hover 79
Figure 7.1: Energy Density battery chemistries and carbon fuels [5] 81
Figure 8.1: XFOIL Lift & Drag Polar Accumulation Plots 91
Figure 8.2: Rotor Performance Comparison, B03 92
Figure 8.3: Rotor Performance Comparison, B04 93
Figure 8.4: Dynamic Performance, Test Scenario 2 94
Figure 8.5: Thrust And Power Output, Test Scenario 2 95
Figure 8.6: Power Output Comparison, Test Scenario 2 96

NOMENCLATURE

Description	Symbol	Unit
Rotor Area / Rotor Annulus	A_r	m^2
Blade Length	l_b	m
Air Density	ρ, ρ_{ISASL}	Kg/m^3
Number Of Blades	N_b	i
Pitch Angle, Angle of Attack (AoA)	θ_{ix}, θ_i	Kg/m^3
Rotor Speed / Head Speed	N_r	r/s
Rotor Annulus Radius	$R_o, R_B, R_{min}, R_{max}$	m
Chord Length	B	m
Blade Thickness	C	m
Rotational Speed, Tip Speed	ω_r, ω_b	rad/s
Radial Position Increment	r_i	–
Reynolds Number	Re	Kg/m^3
Energy	L	$Kg.m^2/s^2$
Mass Inertia	I_b	$Kg.m^2$
Net Torque	τ_{net}	$N.m$
Angular Moment/ Torque	τ_B	$N.m$
Lift Slope Constant	α	–
Rotor Solidity	σ	N/m^2
Induced Velocity	v_{in}	m/s
Blade Section Increment	n_i	i
Thrust Coefficient	C_T	–
Power Coefficient	C_P	–
Lift Coefficient	C_L	–
Drag Coefficient	C_D	–
Sample Rate / Resolution	n_p, n_I, n_{raw}	i
Voltage	V_{ave}, V_m, V_s	V
Electrical Current	I_{sm}, I_m, I_s	A
Thrust	$T_f, T_{sm}, T_m, T_s, T_{poly}$	N
Power Output	P_s, P_{poly}	W
Gross Takeoff Weight (GTW)	m_{GTW}	kg
Rotor Drag Force	F_d	N
Rotor Drag Coefficient	q_r	–
Rotor Thrust Coefficient	k_r	–
Battery Energy Density	G_{LiPo}	Wh/kg
World Linear Coordinate Vector	ξ	–
Euler Angular Coordinate Vector	η	–
Axis Coordinate Transformation Matrix	W_η	–
Flight Control System	FCS	–
World Coordinate System	WCS	–
Body Coordinate System	BCS	–
Flight Control System	*FCS*	–
Body Dynamics Block	*PLANT*	–
Rotor Thrust State Block	*KT-UPDATE*	–
Climb-To-Height Trajectory	*C2H*	–

1. INTRODUCTION

The advent of miniaturized electronics in the early '60s catalysed the development of advanced aerospace tools and electronic flight control systems, thereby enhancing safety and operational capabilities. This technological leap was further accelerated by the onset of Industry 4.0, which integrated cross-sectoral innovations to drive economic growth and improve quality of life through automation. Concurrently, growing environmental concerns have necessitated more efficient and sustainable logistics solutions, leading to the democratization of advanced aerospace technologies like quadrotor-crafts due to reduced production costs. Despite these advancements, the aerospace industry continues to grapple with complex optimization challenges, reminiscent of those faced since the era of the Kittyhawk almost a century ago [2].

Building on the democratization of advanced aerospace technologies, quadrotors have gained significant traction in the commercial market which is expected to triple in size by 2027 [3, 4]. Their popularity stems from their versatility, cost-effectiveness, and ease of use, attributes made possible by the miniaturization of electronics and reduced production costs. These unmanned aerial vehicles are now ubiquitous in various sectors, serving a multitude of use-cases ranging from aerial photography and surveillance to logistics and delivery services. The quadrotor's adaptability and operational efficiency make it a cornerstone in the evolving landscape of commercial aerospace applications.

Notwithstanding their demonstrated efficacy, quadrotors persistently encounter scalability limitations such as energy density and propulsion efficiency [5]. Consequently, the conundrum of optimizing these platforms to broaden their mission capabilities, while concurrently adhering to performance benchmarks, necessitates balancing the trade-offs between endurance, payload capacity, cost, and complexity [6-8]. With these challenges in mind, this work focuses on how rotor geometry and payload capacity variations affect performance characteristics and dynamic behaviours in a quadrotor with content summarized respectively below.

Chapter 1 provides a brief overview of existing conventional single rotor systems and modern quadrotor platforms. By identifying their characteristics, applications, benefits, and limitations, the research problems and scope is then formulated.

Chapters 2 – 3 introduce theoretical formulations governing the aerodynamic nature of a variable pitch rotor system and define the body dynamics of a quadcopter. This section crucial

for empirical tests (§4) and the development of the control system used in Simulink simulations (§5).

Section 4 focuses on a comprehensive empirical validations of varying rotor geometries to develop a quantitative overview of theoretical predictions made by the Blade Element Momentum Theory (BEMT) model (§3). Details related to the data processing methodology using MATLAB, and the airfoil computational analysis performed using XFOIL are then discussed. Empirical comparisons are then used to establish insights into reliability and accuracy of the BEMT model rotor which is integrated into the FCS simulated in the Simulink simulation.

Chapter 5 presents quadrotor control systems in Simulink, integrating control laws with variable pitch Blade Element Momentum Theory (BEMT) rotor systems. The chapter delineates the architecture of the control system, covering function blocks such as CMD, FCS, PLANT, and KT-UPDATE and provides linearized equations for body forces, angular states, and motion. Assumptions related to airframe and rotor inertia are discussed, along with the transformation of angular to linear states. The chapter also outlines the role of PID controllers in the Flight Control System (FCS), detailing error state calculations and output limitations.

Chapter 6 presents a rigorous evaluation framework aimed at understanding the interplay between rotor geometry and payload capacity in quadrotors, focusing on their impact on efficiency and endurance. Utilizing a single climb-to-height trajectory and constrained rotor speed, the study tests three rotor geometries under two payload scenarios. Using simulated outputs, comparative analysis highlights the differences between scenarios.

Chapters 7 – 8 provides a comprehensive analysis of quadrotor performance, emphasizing control system adaptability, rotor geometry, and payload capacity. It highlights the trade-offs between fuel and battery-based power systems, affecting endurance and cargo capabilities. Different rotor variants are assessed for specific applications, and the impact of PID tuning on system responsiveness is discussed. The findings offer a framework for optimizing quadrotor performance, aiding in hardware selection and mission planning. This chapter also outlines how empirical validation and simulation showed the significance of rotor geometry scalability and how it affects efficiency and performance. Type text here

1.1. Overview Of Rotorcraft Types and Applications

This section provides a condensed introductory summary of rotorcraft development and outline specifics related to modern commercially available quadrotor-craft, their applications as well as underlying sub-systems.

1.1.1. Conventional Single-Rotor Craft

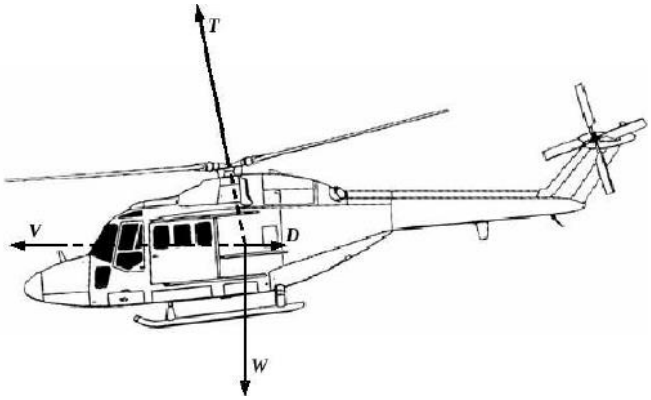

Figure 1.1: Single Rotorcraft System [9]

Single-rotor systems, commonly found in traditional helicopters, are predominantly used in applications requiring high payload capacities and extended flight durations. These systems excel in tasks such as search and rescue operations, aerial surveying, and heavy cargo transportation. Additionally, their ability to hover and execute vertical take-offs and landings adds to their versatility, making them a preferred choice for a wide range of commercial, military, and emergency response applications.

In single rotor systems such as helicopters, thrust is generated by increasing the collective, or blade pitch angle of the main rotor blades. As illustrated in Figure 1.1, lateral accelerations in the horizontal plane of motion (V) are achieved by tilting the rotor swashplate to alter the angle of the thrust vector (T) relative to mass centroid vector (W). The torque moment generated by the main rotor system is counteracted by either inducing a tangential torque moment generated by a secondary tail rotor or with the use of a coaxial rotor rotating in the same rotation plane as the main rotor. In hovering flight, yaw changes are achieved by varying the moment balance between the main rotor and the thrust force of the tail rotor.

1.1.2. Quadrotor Platforms

Most commercially available Quadrotors are employed in aerial photography, surveillance, and small-scale logistics. Like their single-rotor counterparts, quadrotors share capabilities by being

able to hover, execute vertical take-offs and landings, and navigate in confined spaces. Their adaptability and simpler mechanical design make them well-suited for tasks that require agility and quick deployment, such as drone racing, agricultural monitoring, and emergency response scenarios.

Figure 1.2: DJI Air 2S [10]

Quadrotor-craft platforms (Figure 1.2) the were first conceived in 1922 by Etienne Oehmichen [11] and consist of a 4-rotor frame layout in either a X or + frame. The general configurations consist of two sets of fixed pitch counter-rotating rotors that are driven by BLDC motors powered from LiPo batteries. More advanced platforms have also incorporated hybrid gasoline-electric generation systems to charge onboard batteries and extend range [12]. Depending on the mission profile, the interfacing and control of the quadrotor can vary. For basic operations, radio transmitter interfaces are commonly used. However, for more advanced mission profiles and autonomous operations, integration with sophisticated flight control systems like the HEX Cube Orange is often employed [13].

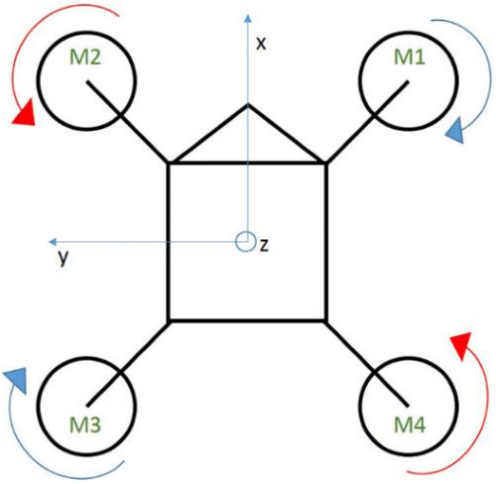

Figure 1.3: Quadrotor Forces & Moments

As is illustrated in Figure 1.3, altitude changes (Z-Axis) rely on thrust induced from all rotors combined. Pitch and roll and attitude adjustments are enabled by altering the thrust balance between counter-rotating rotors pairs about X|Y-Axes relative to the COG (centre of gravity). Varying moment couples from opposing rotors enables yaw orientations about the Z-Axis. See §2, P26 for more detail overview regarding control methodology. To highlight the applications for commercial quadcopter platforms, common quadrotor-craft will be classified according to Table 1.1.

Table 1.1: Type Classification

Description	Classification		
	Type 1	Type 2	Type 3
Endurance / Range	15 – 30min	30min – 1hr	> 1hr
Power Requirement	< 2kW	2 – 4kW	> 4kW
Lift Capacity / GTW	0 – 1kg	1 – 4kg	> 4kg
Application / Use	Hobby, Photography, Misc.	Pro. Photography Surveillance Rapid Transport	Surveillance, Surveying Transport, Crop Management Search and Rescue

***Information presented in this table is intended for illustrative purposes.**

In this basic comparison, it can be observed that payload capacity scales with flight endurance which in turn enables more demanding mission profiles. Applications for Type 1 class quadrotors generally focus more on cost efficiency, whereas Types 2 – 3 prioritises higher endurances and payload capacities to extend operational range or enable more sophisticated mission profiles. Platforms in classes Type 2-3 are sometimes also outfitted with bespoke optical sensors or optimized for further enhanced capabilities such as operating in hazardous

environments. From these basic comparisons it will later be shown in §6, (P70) how payload capacity and hardware selection affects flight behaviours and energy efficiency and constrains mission profile selection.

1.2. Research Problems & Aims

Before exploring how limitations noted above translate to practical implications highlighted in sections below – It will be noted that the complexity of aerodynamic systems, characterized by their non-linear behaviors and interdependent variables, cannot be overstated. This work aims to provide insights that are particularly useful for early-stage development efforts. Therefore, the content, references, and comparisons are tailored to be directly relevant to the specific focus of endurance, efficiency, and propulsion systems in quadrotors.

In this study, "application scalability" refers to the mission profile that dictates an aircraft's endurance and payload capacity. These factors are primary design constraints that influence hardware selection, dynamic behaviour, and overall airframe performance [6]. However, further analysis in §6.3, P73 reveals that these platforms encounter limitations in scalability, particularly when tasked with missions requiring high endurance (> 1hr) and significant payload capacity. Conversely, it is shown that flight endurance limitations are exacerbated by high energy demands when operating at slow speeds. This issue is further compounded by the efficiency limitations of fixed-pitch propulsion systems commonly used in electric quadcopters.

To optimize quadrotor endurance and payload capacity, several key factors must be considered. These include refining the airframe design to accommodate necessary payloads, reducing parasitic aerodynamic drag, and enhancing the efficiency of power delivery and drivetrain systems. However, these optimizations face inherent limitations of which practical implications are identified respectively below and will be discussed further on in this subsection:

1. Limited energy density of chemical batteries constrains the amount of energy that can be stored onboard which limits flight endurance potential.
2. Payload constraints incurred by chemical batteries to augment flight endurance results in higher payloads, reducing rotor efficiency and useful cargo capacity.
3. Propulsion efficiency of fixed-pitch rotor systems is limited to sensitive design criteria and flight profiles.

1.2.1. Energy Density

Energy density is quantified as energy stored per unit mass and volume and is an important factor to consider since its finite availability constrains flight endurance – a term which is defined as the maximum operational duration or range achievable by an aircraft [14].

Chemical lithium-polymer (LiPo) batteries used in quadcopters noted in §1.1.2 have a much lower energy density compared to fuel-based systems. Work comparing energy sources for aerospace applications notes that current LiPo battery technologies on average reach $0.2\ kWh/kg$, whereas more recent developments from CATL - a Chinese based battery OEM promise up to $0.5\ kWh/kg$ using a "*condensed matter*" chemistry architecture. Even though these figures are impressive, they pale in comparison to gasoline which can deliver up to $12\ kWh/kg$ [5, 15]. While further work exploring theoretical energy densities of chemical batteries does show promise, the commercial potential of these solutions is expected to be years away [16, 17]. As will be outlined in respective sections below - energy density is a foundational aspect that constrains mission profiles and compromises made between endurance, payload capacity and dynamic performance characteristics discussed later in §6, (P70).

1.2.2. Payload Capacity and Scalability

From a fundamental perspective, the principle of energy conservation dictates that the work done is proportional to mass and acceleration [18]. To sustain flight, endurance will be dependent on the energy depletion rate – the capacity of which is dependent on the energy stored onboard as outlined previously. Given that all components will contribute to airframe mass – powertrains, hardware, and instrument configurations must be considered on the basis that their mass contributions will also affect energy consumption rates and thus flight endurance [6].

Focusing first on powertrains - In battery-powered quadrotors, the mass allocated for energy storage remains constant throughout the flight, whereas power output declines with depletion. This is because battery mass remains constant regardless of charge level. In contrast, fuel-powered platforms have the advantage of consistent power availability. Additionally, the total mass of the aircraft decreases as fuel is consumed, effectively reducing the power required to maintain speed. Increasing battery energy capacity to offset flight endurance limitations has a significant impact on payload capacity. This is especially true when compared to fuel-powered systems, as energy density is a function of mass and volume, as outlined in §1.2.1, (P20).

Works comparing alternative energy sources for UAV applications shows that fuel powered platforms are expected to maintain longer flight duration is illustrated from recent developments in the quadrotor industry [19, 20]. By employing fuel powered range extenders to charge onboard batteries, the New Atlas reports that the *HYBRiX 2.1* quadrotor platform developed by the Spanish startup *Quaternium*; "*features a gasoline/battery-electric hybrid drive system that reportedly gives it a flight time of up to four hours per fill/charge*", further extending the 4 hour record reported in 2017 [21, 22]. While these endurance figures are impressive, cargo capacity is limited to 10kg. The contrast in performance differences between electric-hybrid and fuel powered quadrotors is illustrated in an article published in 2017 by Drone Rush [23] reporting that the *Belias* – a two-stroke ICE powered quadrotor platform developed by SOAPDrones was able to maintain similar hover times to that of the *HYBRiX 2.1* but could be scaled for payload capacities in excess of 200kg. While payload data from tests were not available, it is reasonable to expect that the *Belias* will outperform the *HYBRiX 2.1* as abstracted performance figures show in §7.1, P80.

From the endurance comparisons highlighted above, its further apparent that the payload capacity trade-off $(m_{gtw} \gtrsim 40 - 60\%\ estimated^{*})$ sacrificed by electric-hybrid systems like the *HYBRiX 2.1* and other solutions [24, 25] to attain higher endurances will limit the commercial potential for applications outside of surveillance and light logistics support. Whereas platforms like the *Belias* are expected to provide highly scalable mission profiles by leveraging the superior energy density of carbon-based fuels.

Focusing more on scalability aspects of quadrotors – From the comparisons shown in §6, (P70) suggest that operational efficiency and dynamic performance of quadrotors is crucially dependent on optimal selection of rotor geometry.

1.2.3. Rotor Propulsion Efficiency

As the scope of this work focuses on validating the scalability of a quadrotor flight control system using variable-pitch rotor elements. The comparisons below are concisely formatted to highlight key aspects related to the focus on endurance and efficiency, as well as challenges faced with fixed-pitch rotors.

As previously discussed in §1.1.2 (P16), quadrotors with fixed-pitch propulsion systems achieve manoeuvrability and stabilization by rapidly modulating the speed of opposing rotors. From energy conservation this practically equates to effort from BLDC stators to counteract the inertial forces generated by the motor hub and rotor blades. Incorporating this reasoning into

the mission profiles outlined in Table 1.1 (P18), both Blade Element Momentum Theory (BEMT) and additional studies suggest that rotor efficiency diminishes at low forward flight speeds while maintaining altitude. This decrease in efficiency is attributed to the increased energy expenditure required by the rotors to displace air, particularly when the rotorcraft is operating outside the ground effect zone. [14, 26-29]

Focusing on the scalability of quadrotors, evidence from empirical performance comparisons shown in §6, (P70) demonstrate that minor variances in rotor geometry significantly impacts mission profiles, and indicate that operational efficiency and dynamic performance are closely tied to payload capacity and rotor geometry.

In this work, the term "*disk loading*" – defined as the thrust per unit area of the rotor disk in actuator-disk theory [27] – is used in early design studies as a simplified factor that characterizes rotor performance relative to energy consumption (§4, P35) related to drag (see §3, P31). Optimal rotor configurations strive to minimize disk loading by harmonizing rotor speed with airfoil geometry. The goal is to maximize lift forces across the rotor blade while simultaneously reducing drag. With this in mind – fixed-pitch rotors offer less flexibility since disk loading can only be varied within an optimal speed range (Figure 1.4), deviations of which exacerbates efficiency losses [30]. In contrast, variable-pitch rotors offer the flexibility to mitigate high disk loading with the benefit of blade pitch adjustments [31-33].

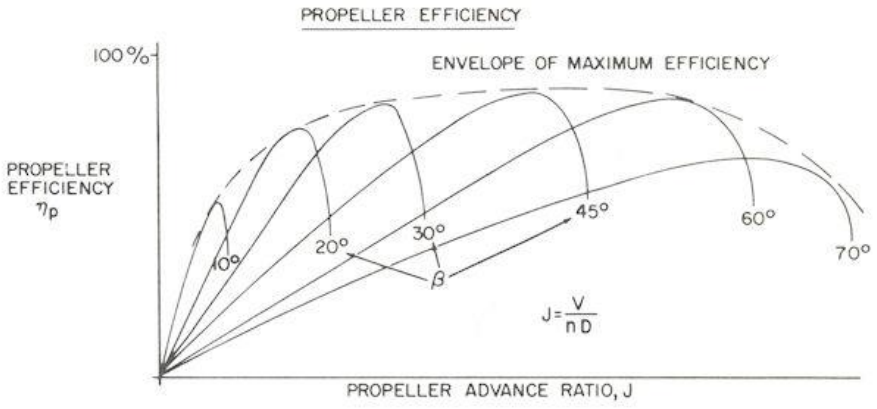

Figure 1.4: Fixed Pitch Propeller Efficiency [30]

Recent works examining the integration of variable-pitch propulsion systems into quadrotor platforms suggest that this propulsion technology shows potential in mitigating challenges noted above faced by quadrotor platforms shown in §1.2.2 (P20). Work from *Wu* [34] agrees with that of *Pang* [35]who concluded that "*vibration turned out to be a prominent concern in airframe design*". Its also interesting to find that endurance assessments closely align with

abstracted endurance figures approximated in this work as discussed in §1.2.2, (P20). Investigating dynamic performance of small-scale variable pitch quadcopters, *Cutler* [37] points out that mechanical complexity of variable pitch systems remains challenging [36, 38, 39].

It's evident from these efforts that several technical challenges highlighted must be addressed before this approach can be commercially viable. The section below further outlines these issues by focusing on scalability aspects of quadrotor control systems.

1.2.4. Control System Scalability

As previously discussed, integrating fuel-powered, variable-pitch rotor systems into quadrotors offers a promising avenue for overcoming scalability limitations.

For large-scale quadrotors designed for intensive missions, varying payload capacities and endurance capabilities are expected. Although these variants differ in mission profiles and performance specifications, as outlined in §1.2.2, they share similar design principles and operational mechanics. This commonality suggests the feasibility of developing a Flight Control System (FCS) designed for scalability.

The impact of these factors on control responses is crucial, especially for quadrotors deployed in high-intensity mission profiles that require robust control authority, or extent to which a control system can influence the motion and stability of a vehicle. It appears that a scalable approach to control system development is not well understood, as evidenced by the limited research available on the subject.

Research presented in sections §1.2.1–1.2.3 primarily addresses the practical challenges of incorporating variable-pitch rotors, such as mechanical complexity and reliability. Studies by *Pang*, *Abhishek*, and *Wu* [34-36] developed and tested prototypes with single payload and rotor configurations, making them incomparable to the efforts in this work. Additionally, empirical tests (§4, P35) revealed that both simulated airfoil performance and the Blade Element Momentum Theory (BEMT) rotor model are sensitive to geometry definitions and boundary conditions. [34-39]

1.2.5. Use Cases – Life Preservation

According to a report by the International Organization for Migration, over 22,500 migrants have been declared dead or missing worldwide since 2014, with over half of these fatalities

occurring during Mediterranean crossing attempts. [40]. More recently, up to 90 migrants are feared to have drowned off the Libyan coast [41]. A great deal of lives could have been saved if the solution mentioned in the article by The Verge [42] was scaled to lift about 54kg (weight of single life jacket taken at 0.6Kg [43]), and had a range capability of 224km to patrol a popular migrant route between Scaglietti and Tripoli [44].

1.3. Research Framework & Methodology

The objective of this study is to develop a scalable Flight Control System (FCS) for a fuel-powered quadrotor with variable-pitch rotors, targeting high-endurance applications. In this context, the research methodology described in this section was focused to answer three main questions in §6.1 (P70) and repeated here for clarity.

1. Which rotor configuration provides the highest acceleration and vertical climb speed for the least power consumption?
2. How does payload capacity affect power demands and efficiency?
3. How does the control system and airframe response and behaviour change during flight?

To achieve this, the research strategy was designed to align the validation and data collection phases, minimizing the risk of scope deviation, and ensuring that observations are empirically grounded. Although the initial goal was to implement the FCS in a full-scale prototype, simulation-based validation was deemed more practical due to constraints on time and budget.

While software-based modelling and simulation techniques offer detailed insights into the issues discussed earlier, comparisons in this work suggests that aerodynamic performance remains a sensitive aspect for aircraft, often necessitating empirical validation to ensure dependable results [45]. However, this study focused on empirical evaluations to validate model performance, particularly concerning variations in rotor geometry and payload capacity. The assessments were conducted on a medium-sized quadrotor equipped with a variable-pitch rotor system, utilizing MATLAB and XFOIL for the analysis.

The development of a MATLAB-based rotary propulsion system hinges on integrating momentum theory with elemental airfoil flow principles [14, 27]. Traditionally, airfoil performance metrics like lift and drag coefficients are empirically determined through wind tunnel tests [46]. Given constraints on cost and equipment availability, simulation software like Ansys Fluent or Ansys CFX can also be employed. These tools offer either sequential (One-

Way Coupling) or parallel (Two-Way Coupling) analysis methods, depending on the relevance of fluid-structure interaction (FSI) effects [47, 48].

For this study, the Blade Element Momentum Theory (BEMT) model leverages XFOIL, a widely used wind tunnel emulator known for its user-friendliness, reliability, and computational efficiency. XFOIL is utilized to simulate airfoil (C_L) and drag (C_D) coefficients through code based on potential flow panel methods and integral boundary layer formulations for predicting flow separation. However, it's worth noting that the solver's assumptions of two-dimensional, inviscid, and incompressible flow may not fully capture real-world conditions that could involve three-dimensional or compressible effects [45, 47, 49].

The Simulink based quadrotor control system architecture (§5, P56) referenced from a book by Carillo and work by Ferry [50, 51] was extensively modified to integrate variable pitch control laws. The BEMT rotor models were designed to simulate rotor thrust forces. To ensure accuracy, these models used data and blade dimensions that were validated through tests, closely representing real-world performance. Furthermore, airframe geometry was standardised and assumed to be rigid with the uniform density tuned to reach a specific payload target. Air properties are further constrained to sea-level elevations according to ISA [52].

In a dynamic environment, the scalability aspects of the control system were validated using three distinct rotor variants across two payload scenarios. Given that this work places a particular emphasis on evaluating how endurance and efficiency are impacted at different scales, the climb-to-height (C2H) flight trajectory was deliberately chosen to induce maximum power demands (§6.2.1, P71).

2. QUADROTOR CONTROL MODELLING

This section will provide a basic overview of quadrotor control theory which will be later used as a basis for the scalable FCS architecture evaluated later in §6, P70. Equations and theory for the mathematical modelling of the quadrotor craft are based on Newton-Euler equations for an X-type quadrotor as referenced in a textbook by Carrillo [51], thus concise details are provided to highlight key points. Vectorised matrix forms of equations are linearised before being integrated into the model explained in § 5, P56.

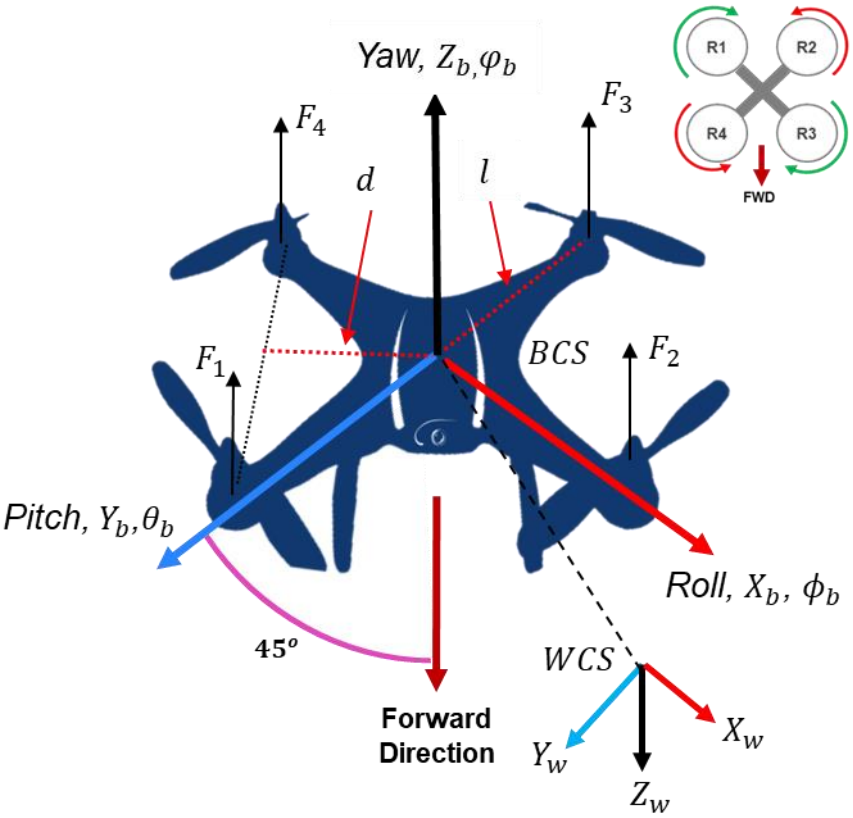

Figure 2.1: Quadrotor Interial & Body Frames [53]

2.1. Orientation & Translation of Fixed Pitch Quadrotors

Quadrotors are considered 6-DOF (degrees of freedom) systems by being able to translate and rotate $(\phi_b, \theta_b, \varphi_b)$ about the body coordinate system (BCS) axes $[X_b \quad Y_b \quad Z_b]^T$. For quadrotors using fixed pitch rotor systems, thrust (f_i) is a function of the thrust coefficient (k) and rotor speed (ω_r) such that,

$$f_i = k\,\omega_i^2 \qquad 2.1$$

In a hovering state where $[\dot{X}_b \quad \dot{Y}_b \quad \dot{Z}_b]^T = 0.0\, m/s, Z_b = constant$ given that thrust forces oppose gravity. In Newtonian terms, thrust required to maintain hover can be defined as $T_f = m_b g - m_b \ddot{Z}_b$. Altitude Z_b thus depends on the vertical acceleration as the vectorized form below shows.

$$T_f = k \sum_{i=1}^{4} \omega_i^2 \,,\; T^B = \begin{bmatrix} 0 \\ 0 \\ T \end{bmatrix} \tag{2.2}$$

As the rotor system is assumed to be rigid, yaw movement about the $BCS\ Z_b$ axis depends on torque τ_{M_i} induced by rotor systems, which are defined as the sum of rotor drag forces (q_r) and angular moments of inertia (I_r) shown in Eq. 2.3.

$$\tau_{M_i} = \sum_{i=1}^{4} q_r \omega_i^2 + I_r \dot{\omega_i^2} \tag{2.3}$$

Because angular velocity is usually small in comparison to the torque related to drag forces, $\dot{\omega_i^2} = 0$. [51]

$$\tau_{M_i} = \sum_{i=1}^{4} q_r \omega_i^2 \tag{2.4}$$

Assuming $\sum M_{COG} = 0$, roll and pitch and yaw $(\phi_b, \theta_b, \varphi_b)$ moments about BCS reference frame axes are enabled by altering thrust force f_i acting along length l. From Eq. 2.1 and 2.4 – angular moments (τ_B) of the body is shown to be,

$$\tau_B = \begin{bmatrix} \tau_\phi \\ \tau_\theta \\ \tau_\varphi \end{bmatrix} = \begin{bmatrix} lk\,(-\omega_1^2 + \omega_3^2) \\ lk\,(-\omega_4^2 + \omega_2^2\,) \\ q\,(\omega_1^2 - \omega_2^2 + \omega_3^2 - \omega_4^2) \end{bmatrix} \tag{2.5}$$

2.2. Orientation & Translation of Variable Pitch Quadrotors

In variable pitch rotor systems, thrust is dependent on blade pitch angle as discussed in §5.1.2 (P60). In this paper it will be assumed that a single drivetrain will power all rotors systems at constant speed ($\omega_r = constant$), thus thrust coefficients (k_i, q_i) will vary with changes in blade pitch angle. Furthermore, for X-Type quadrotors, the forward direction relative to the BCS is rotated in Z_b by 45^o or $\pi/4$ radians (Figure 5.5), which means thrust forces which enable pitch and roll moments ($\tau_\phi\,, \tau_\theta$) act at the distance $lSin(\pi/4)$ from the body mass centroid. Eq. 2.3 and 2.5 can then be rewritten to become [51],

$$T_f = \omega_r^2 \sum_{i=1}^{4} k_i\,,\; T^B = \begin{bmatrix} 0 \\ 0 \\ \omega_r^2\,(k_1 + \; k_2 + k_3 + k_4) \end{bmatrix} \tag{2.6}$$

$$\tau_B = \begin{bmatrix} \tau_\phi \\ \tau_\theta \\ \tau_\varphi \end{bmatrix} = \begin{bmatrix} l\,Sin\left(\frac{\pi}{4}\right)\omega_r^2\,(-k_1 + k_3) \\ l\,Sin\left(\frac{\pi}{4}\right)\omega_r^2\,(-k_1 + k_3) \\ \omega_r^2\,(q_1 - \; q_2 + q_3 - q_4) \end{bmatrix} \tag{2.7}$$

2.3. Newton-Euler Equations for X-Type Quadrotors

The linear position of a quadrotor craft about the inertial (BCS) frame axes relative to a stationary point (Figure 2.1, P26) on earth (WCS) is defined by $\xi = [x, y, z]^T$. Euler angles $\eta = [\phi, \theta, \varphi]^{\mathrm{T}}$ about the body centre of mass along BCS axes define angular orientations for pitch (ϕ), roll (θ) and yaw (φ) of the quadrotor-craft as [51].

$$\xi = \begin{bmatrix} x \\ y \\ z \end{bmatrix},\; \eta = \begin{bmatrix} \phi \\ \theta \\ \varphi \end{bmatrix},\; q = \begin{bmatrix} \xi \\ \eta \end{bmatrix} \tag{2.8}$$

Linear $\dot{\xi} = [\dot{x}, \dot{y}, \dot{z}]^T$ and angular $\dot{\Omega} = [p, q, r]^T$ velocities about the BCS axes are further defined as

$$\dot{\xi} = \begin{bmatrix} \dot{x} \\ \dot{y} \\ \dot{z} \end{bmatrix},\;\; \dot{\Omega} = \begin{bmatrix} p \\ q \\ r \end{bmatrix} \tag{2.9}$$

2.3.1. Coordinate Rotation Matrix

A rotation matrix (Eq. 2.10) is used to transform axes coordinates from $BCS \rightarrow WCS$ to enable the quadrotor to orientate itself relative to a stationary point in the WCS.

$$R_\phi = \begin{bmatrix} 1 & 0 & 0 \\ 0 & Cos\,\phi & Sin\,\phi \\ 0 & -Sin\,\phi & Cos\,\phi \end{bmatrix}, R_\theta = \begin{bmatrix} Cos\,\theta & 0 & -Sin\,\theta \\ 0 & 1 & 0 \\ Sin\,\theta & 0 & Cos\,\theta \end{bmatrix}, R_\varphi = \begin{bmatrix} Cos\,\varphi & Sin\,\phi & 0 \\ -Sin\,\phi & Cos\,\varphi & 0 \\ 0 & 0 & 1 \end{bmatrix} \tag{2.10}$$

Global coordinates (WCS) are ordered according to X-Y-Z which means that BCS coordinates are evaluated with North-East-Down (NED) in Z-Y-X order where $S_x = Sin(x)$ and $C_x = Cos(x)$. Conversely, WCS can also be transformed to BCS using $R^{-1} = R^T$ which is important to facilitate trajectory corrections during flight [51, 53].

$$R = R_\varphi R_\theta R_\phi = \begin{bmatrix} C_\varphi C_\theta & C_\varphi S_\theta S_\phi - S_\varphi C_\phi & C_\varphi S_\theta C_\phi + S_\varphi C_\phi \\ S_\varphi C_\theta & S_\varphi S_\theta S_\phi + C_\varphi C_\phi & S_\varphi S_\theta C_\phi - C_\varphi S_\phi \\ -S_\theta & S_\phi C_\theta & C_\theta C_\phi \end{bmatrix} \quad 2.11$$

2.3.2. Linear And Angular Velocity Transformation

Euler angular velocities ($\dot{\eta}$) in the body frame are found from the inverse product of the transformation matrix W_η (Eq. 2.12) about the inertial frame, and angular velocity vector $[p, q, r]^T$(Eq. 2.9).

$$W_\eta = \begin{bmatrix} -Sin\,\theta & 0 & 1 \\ Cos\,\theta\,Sin\;\phi & Cos\,\phi & 0 \\ Cos\,\theta\,Cos\,\phi & -Sin\,\phi & 0 \end{bmatrix} \quad 2.12$$

$$\dot{\eta} = W_\eta^{-1}\Omega, \begin{bmatrix} \dot{\phi} \\ \dot{\theta} \\ \dot{\varphi} \end{bmatrix} = \begin{bmatrix} -Sin\,\theta & 0 & 1 \\ Cos\,\theta\,Sin\,\varphi & Cos\,\phi & 0 \\ Cos\,\theta\,Cos\,\phi & -Sin\,\theta & 0 \end{bmatrix}^{-1} \begin{bmatrix} p \\ q \\ r \end{bmatrix} \quad 2.13$$

$$\Omega = W_\eta \dot{\eta}, \quad \begin{bmatrix} p \\ q \\ r \end{bmatrix} = \begin{bmatrix} 1 & 0 & -Sin\,\theta \\ 0 & Cos\,\phi & Cos\,\theta\,Sin\,\varphi \\ Cos\,\theta\,Cos\,\phi & -Sin\,\theta & Cos\,\theta\,Cos\,\phi \end{bmatrix}^{-1} \begin{bmatrix} \dot{\phi} \\ \dot{\theta} \\ \dot{\varphi} \end{bmatrix} \quad 2.14$$

2.3.3. Quadrotor Dynamics

Applying Newtons second law, linear accelerations (Eq. 2.15) in world coordinate system (WCS) reference frame are defined as the sum of thrust forces (T_f) in the BCS reference frame, gravitational mass (mg) and drag forces (F_d) acting on the airframe body of the quadrotor. Acceleration of the body relative to the BCS can then be obtained by substitution as shown in Eq. 2.17.

$$m\ddot{\xi} = mg - RT_f - F_d \quad 2.15$$

$$\begin{bmatrix} \ddot{X} \\ \ddot{Y} \\ \ddot{Z} \end{bmatrix} = \begin{bmatrix} 0 \\ 0 \\ g \end{bmatrix} - \frac{1}{m} \begin{bmatrix} C_\varphi S_\theta & S_\varphi C_\phi + C_\varphi S_\theta S_\phi & S_\varphi S_\phi - C_\varphi S_\theta S_\phi \\ -S_\varphi C_\theta & C_\varphi C_\phi - S_\varphi S_\theta S_\phi & C_\varphi S_\phi + S_\theta S_\varphi C_\varphi \\ S_\theta & -S_\varphi C_\theta & C_\theta C_\phi \end{bmatrix} \begin{bmatrix} 0 \\ 0 \\ k(\omega_1^2 + \omega_2^2 + \omega_3^2 + \omega_4^2) \end{bmatrix} - \frac{1}{m} \begin{bmatrix} A_x & 0 & 0 \\ 0 & A_y & 0 \\ 0 & 0 & A_z \end{bmatrix} \begin{bmatrix} \dot{X} \\ \dot{Y} \\ \dot{Z} \end{bmatrix} \quad 2.16$$

Angular accelerations (Eq. 2.17) acting on body about the BCS reference frame is considered as the sum of gyroscopic forces due to body inertia with angular velocity (Ω), torque forces (τ_B) from rotor systems (Eq. 2.7), and gyroscopic forces generated by the inertia of rotor blades $\tau_R = J_r \dot{\theta} \omega_r$ which rotate in the Z_b relative to the BCS.

$$I\dot{\Omega} = -\Omega \times \Omega I + \tau_B + \tau_R \quad 2.17$$

$$\begin{bmatrix} \dot{p} \\ \dot{q} \\ \dot{r} \end{bmatrix} = \begin{bmatrix} \frac{(I_{yy}-I_{zz})qr}{I_{xx}} \\ \frac{(I_{zz}-I_{xx})pr}{I_{yy}} \\ \frac{(I_{xx}-I_{yy})pq}{I_{zz}} \end{bmatrix} - J_r\omega_r \begin{bmatrix} \frac{q}{I_{xx}} \\ -\frac{p}{I_{yy}} \\ 0 \end{bmatrix} + \begin{bmatrix} \frac{\tau_\phi}{I_{xx}} \\ \frac{\tau_\theta}{I_{yy}} \\ \frac{\tau_\varphi}{I_{zz}} \end{bmatrix} \quad 2.18$$

Given Eq.2.14, angular accelerations in the WCS reference frame can thus be obtained as shown in Eq. 2.18. It will be noted that linearised forms of equations above are implemented in the Simulink as discussed in Section §5.1.1, P58.

3. ROTOR AERODYNAMICS MODELLING

Rotorcraft propulsion theory used to develop the MATLAB-based model (§5, P56) single-rotor systems incorporate established BEMT theory referenced from Bramwell, et al. [14] and Johnson [26]. To simulate maximum power demand scenario, the rotor is assumed to be in a hovering condition using rigid, untwisted blades with a uniform inflow velocity.

3.1. Blade Element Momentum Theory (BEMT)

Coefficients for thrust (Eq. 3.1) and power (Eq. 3.2), C_T & C_P which are core rotor performance metrics are obtained by integrating over the blade length from radius $R_o \rightarrow R_{max}$ at a given angle of attack θ_i form lift and drag coefficients $C_D,\ C_L$ obtained from XFOIL (§3.3, P32).

Rotor power output is defined from coefficients of airfoil profile drag dC_{Po} (Eq. 3.3) to overcome drag acting on the blade, and induced power dC_{Pi} (Eq. 3.4) to generate lift. Since velocity ω_r (Eq. 3.8) increases with radius station r_i, dC_{Po} and dC_{Pi} are integrated over the blade span at blade angle increment θ_i, with $n_i = 100$ blade sections.

$$C_T = \int_{R_o}^{Rmax} \frac{1}{2}\sigma C_L r_i^2 dr \quad 3.1$$

$$C_P = dC_{Pi} + dC_{Po} \quad 3.2$$

$$dC_{Po} = \int_{R_o}^{Rmax} \frac{1}{2}\sigma C_D r_i^3 dr \quad 3.3$$

$$dC_{Pi} = \int \lambda dC_T \quad 3.4$$

$$dC_T = \frac{1}{2}\sigma a(\theta_i r_i^2 - \lambda r_i)dr \quad 3.5$$

From the equations above and assuming air density as $\rho = 1.224 kg/m^3$ – rotor thrust T_r (Eq. 3.6), and power consumption P_r (Eq. 3.7) is then calculated by:

$$T_r = C_T \rho A_r (\omega_r R_{max})^2 \quad 3.6$$

$$P_r = C_P \rho A_r (\omega_r R_{max})^3 \quad 3.7$$

$$\omega_r = \frac{2\pi N_r}{60} \quad 3.8$$

3.2. Rotor Solidity, Inflow Velocity, Lift Slope and Blade Area

Rotor solidity σ (Eq. 3.9) defines thrust force per unit area of the annulus and is the function of no. of blades N_b, chord length c, and rotor tip radius R_{max}.

$$\sigma = \frac{N_b c}{\pi R_{max}} \tag{3.9}$$

Combining blade element and momentum theory [27], for a rotor in a hovering condition with non-uniform inflow, induced velocity λ (Eq. 3.10) is calculated using,

$$\lambda = \frac{\sigma a}{16}\left[\sqrt{1 + \frac{32}{\sigma a}\theta_i r_i} - 1\right] \tag{3.10}$$

Airfoil lift slope a (Eq. 3.11) defined from the ratio of lift coefficient C_L (output from XFOIL) to incidence angle α.

$$a = \frac{C_L}{\alpha} \quad (\alpha = 5.7) \tag{3.11}$$

3.3. Airfoil Analysis

Airfoil performance characterized in terms of lift and drag coefficients is traditionally evaluated empirically from measurements obtained in wind tunnel testing [23]. Due to limited cost and access to test equipment, airfoil flow behaviour can also be simulated using software tools such as Ansys Fluent or Ansys CFX which offer sequential (One-Way Coupling) or parallel (Two-Way Coupling) analysis schemes depending on the significance of the FSI (fluid structure interaction) effect [24,25].

In this case, the BEMT rotor model (§4.4, P52) will rely on a well-established wind tunnel emulator XFOIL known for its ease of use, robustness, and computational efficiency. In this work, XFOIL is used to simulate the airfoil lift (C_l) and drag (C_d) coefficients using code developed using potential flow panel and integral boundary layer formulation methods to predict flow separation. Since the solver assumes flow to be two-dimensional, inviscid, and incompressible it may not accurately represent real-world scenarios with three-dimensional or compressible effects. [21,24,26]

Lift (C_L) and drag (C_D) coefficients for rotor blades were analyzed using XFOIL [54] set for viscous flow analysis. $N_{crit} = 9$ to simulate an average wind tunnel. The airfoil section NACA number is determined from blade geometry measurements shown in Table 4.2, P38.

Reynolds number (Re) for a given chord length (c) is calculated from tip velocity (V_{tip}). Properties for air are according to the International Standard Day at Sea-level (ISASL) where kinematic viscosity is taken as $v_{kin} = 1.5111\text{e}-5\ \text{m}^2/s$ and the speed of sound $n_{ISASL} = 343.0\ m/s$.

$$Re = \frac{V_{tip} c}{v_{ISASL}} \tag{3.12}$$

$$V_{tip} = \omega_r R_{max} \tag{3.13}$$

$$n_{mach} = \frac{V_{tip}}{n_{ISASL}} \tag{3.14}$$

More information related to the function of the program and its operations are available in the project folder [55]. XFOIL Configuration is further discussed in §4.3, P50.

3.3.1. Ground Effect

Proximity of ground relative to the rotor is significant to consider as ground effect is known to reduce induced rotor power requirements caused by pressure waves which are reflected upwards. Experimental tests conducted by Cheeseman and Bennet [56] [14] approximates the thrust ratio as a function of rotor radius (R_r) to height above the ground (Z_b).

$$\frac{T_r}{T_\infty} = \frac{1}{\left(1-\left(\frac{R}{4Z}\right)^2\right)} \tag{3.15}$$

"*It is found that the power, expressed as a proportion of that required in the absence of the ground, is as low as 0.5 when the rotor height to rotor radius is about 0.4, a typical value for the point of takeoff*". (Seddon [57], P33)

While ground-effect is not considered in the scope of this this work, it's important to note that ground effect can influence takeoff power demands by approximately 30%. Therefore, if the simulation or analysis requires higher precision, the impact of the ground effect should be considered.

3.4. Conservation Of Angular Momentum

From conservation of energy [18], as a body or mass rotates about a point, a net torque τ_{net} (Eq. 3.16) induces a rotating motion in a body, and changes in τ_{net} induce angular acceleration. For simplification, in this work we assume constant rotor head speed (N_r), therefore ω_b and

τ_{net} are constant, conserving momentum. Balanced torques result in no angular acceleration, therefore $\tau_{net} = 0$.

$$L = I_b \omega_b \tag{3.16}$$

$$\tau_{net} = \frac{\Delta L}{\Delta t} = 0 \tag{3.17}$$

4. ROTOR PERFORMANCE CHARACTERIZATION

Experimental validation of the simulated rotor system involves comparing the performance of a physical rotor system described in (§4.1, P36) under controlled conditions to approximations made by BEMT rotor model (§3.1, P31). While mathematical models and simulations can provide valuable insights, geometry definitions and boundary conditions can greatly affect accuracy and performance as will be shown in §6.2.2, P73. This section focuses on characterising the performance aspects of the rotor system experimentally and theoretically.

- §4.1 Discusses technical details relating to the rotor test system used for experimentation, the Arduino code implementation for sample collection as well as calibration procedures.
- §4.2 Outlines the test methodology and data processing workflow (illustrated in Figure 4.1) employed for comparisons to the BEMT rotor model outputs.
- §4.3 Provides an overview of the airfoil analysis performed using XFOIL
- §4.4 Describes the evaluation of various rotor systems using the BEMT rotor model.
- §4.5 Shows performance comparisons between experiments and theoretical rotor models

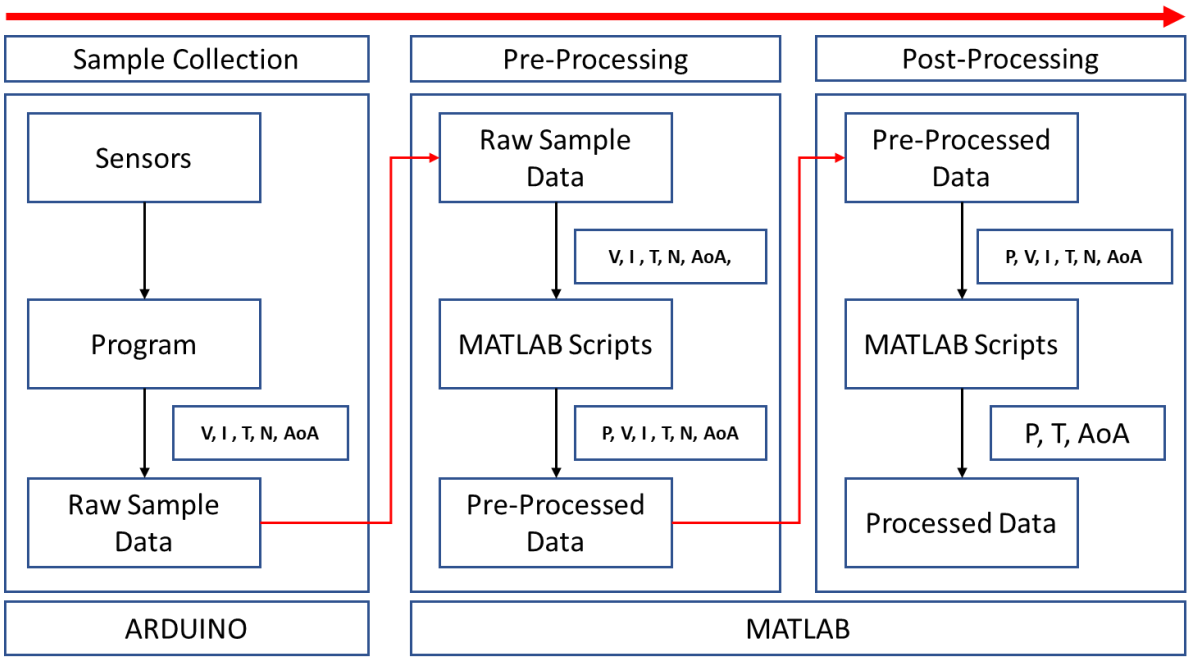

Figure 4.1: Test & Sample Processing Methodology

Note Regarding Logic Control Elements and Coding

To ensure reliability and accuracy of sample data – externally developed Arduino libraries facilitate the calibration of test equipment. Equations for calculations are referenced where relevant.

For conciseness regarding sections below on sensor calibration & data conversion – measurement accuracies and data conversions is limited by the 10bit resolution of the ATmega328 microprocessor used on the Arduino Nano. Analog and Digital inputs are automatically scaled to 10bits.

- Analog inputs are scaled linearly using the internal 5V reference (V_{ref}) where 5V = 1023 bits.
- Digital PWM signals range from 1200-2500µs and are scaled from 0 – 1023bits. Explanations on data conversions and processing will follow respectively.

4.1. Rotor Test System

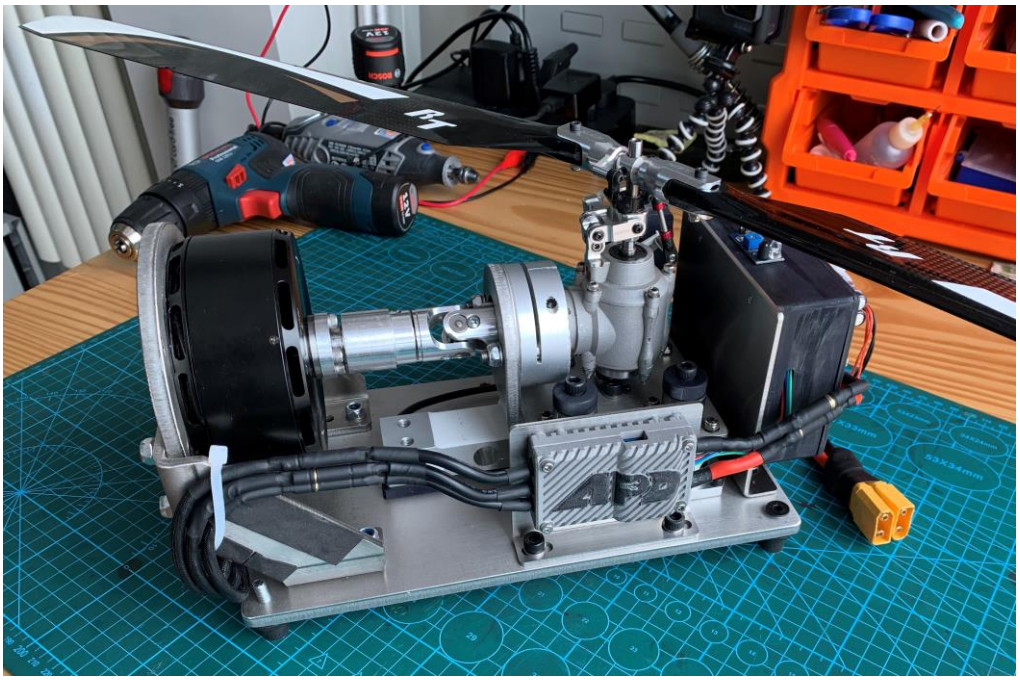

Figure 4.2: Rotor Test Bench

The strategy for comparisons in this work was dependent on empirical testing rather than relying on reference data. In this case, a desktop-sized rotor test system (Figure 4.2) was developed to chart the performance characteristics of three sets of rotor blades (Table 4.2, P38)

at specific speeds. Test results will then be used to validate the Blade Element Momentum Theory (BEMT) rotor model.

4.1.1. Technical Description & Specifications

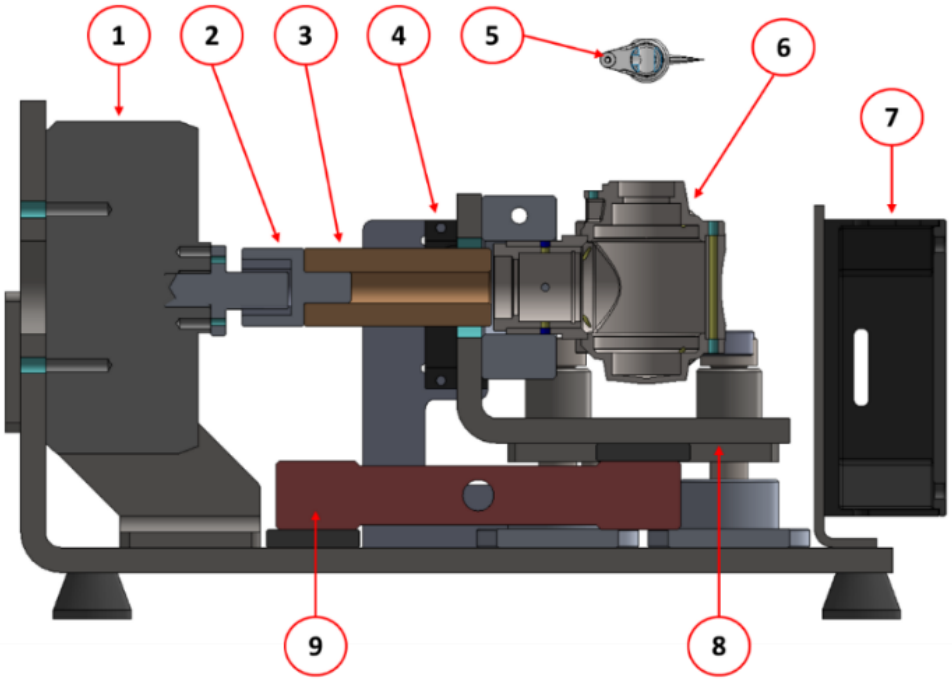

Figure 4.3: Rotor Test Bench

As shown in Figure 4.3, the rotor test scale system consists of an 170KV T-Motor BLDC (1) connected to the shaft a custom built 90º bevel gearbox (6) with a one-way slip bearing (2) and universal joint (3). A servo (4) controls collective pitch of the rotor (5). The rotor rests on bracket bolted to a load cell (9). An IR sensor is used to measure rotor head speed. Voltage and current are measured using a MCS1500 Hall-Effect current sensor.

Table 4.1: Rotor Bench Specifications Overview

Description	Min	Max
Power Output (kW)	2	8
Motor Speed (r/s)	0	6000
Rated Head Speed (r/s)		3000
Blade Pitch Angle (Deg)	- 5.0 ($\pm$1.0)	+35.0 ($\pm$1.0)
Thrust Load Capacity (Kg)		50 ($\pm$0.01)
Construction Materials		304 Stainless Steel & Aluminium
Gear Ratio		1:1

4.1.2. Rotor Blade Specifications

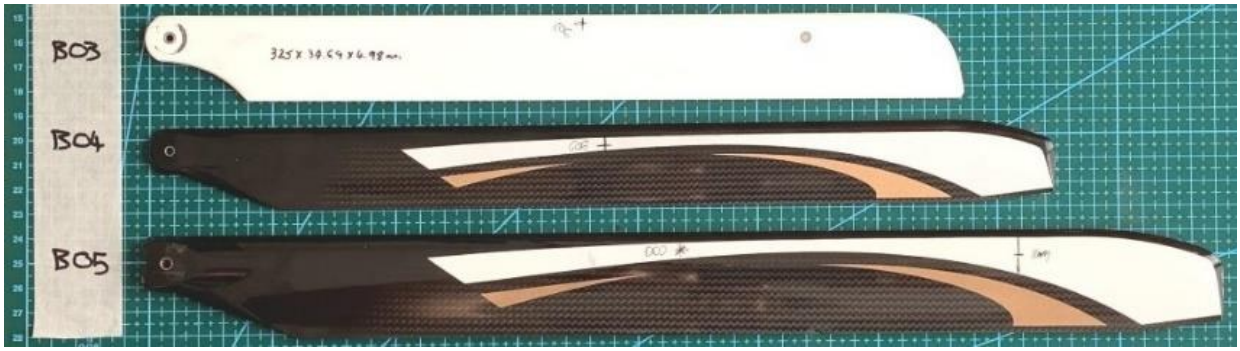

Figure 4.4: Rotor Blade Geometry

Figure 4.4 provides an overview of the rotor blades tested in this work as discussed in §4.2. P46.

Table 4.2: Rotor Blade Specifications

N	R_{max} (mm)	R_F (mm)	C (mm)	B (mm)	b (mm)	NACA	m_b (g)	R_{cog}(mm)
B03	325.00	243.75	34.69	4.98	9.00	0014	26.4	167.50
B04	360.00	270.00	34.00	4.50	10.00	0014	31.4	176.00
B05	430.00	322.50	42.00	5.75	11.00	0014	72.6	207.50

Table 4.2 contains rotor blade specifications obtained from physical measurements using digital vernier calipers.

4.1.3. Test Bench Control Circuit

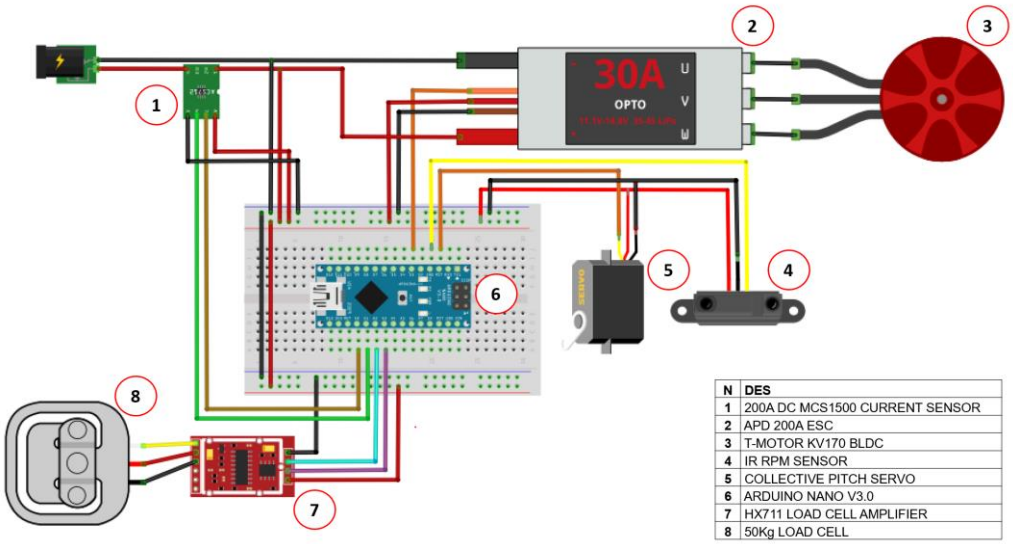

N	DES
1	200A DC MCS1500 CURRENT SENSOR
2	APD 200A ESC
3	T-MOTOR KV170 BLDC
4	IR RPM SENSOR
5	COLLECTIVE PITCH SERVO
6	ARDUINO NANO V3.0
7	HX711 LOAD CELL AMPLIFIER
8	50Kg LOAD CELL

Figure 4.5: Illustration Of The Rotor Bench Control System

Figure 4.5 provides an illustration of electronics used for data acquisition and control of the rotor test bench.

4.1.4. Operational Principles

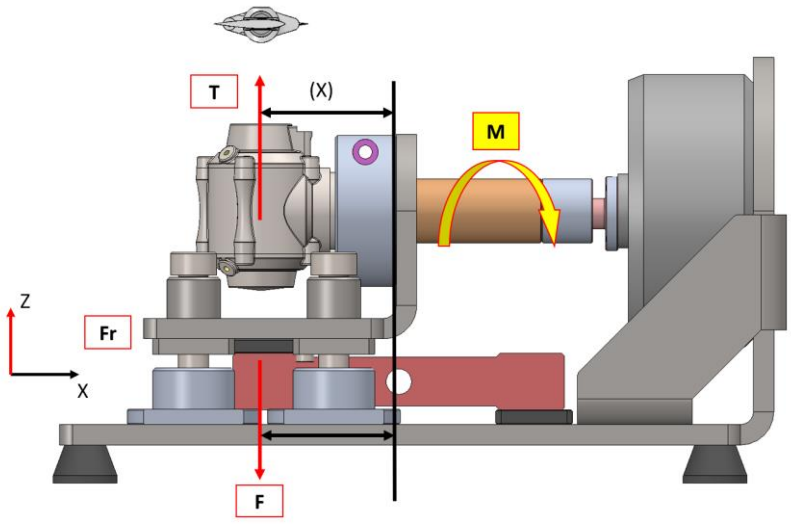

Figure 4.6: Rotor Test Bench Free Body Diagram

As is shown in Figure 4.6 above, the load cell is positioned so that thrust force T (3) is transmitted to the load cell via reactionary force F(1) along the Z-axis. Bearing guides sliding on rigidly mounted guides isolate residual reactionary forces F_r. (2) or moments M (4) about X|Y axes to prevent torsional forces acting on the load cell.

4.1.5. Collective Pitch Measurement & Calibration

Pitch is calibrated using a mechanical dial indicator (Figure 4.7) because it yields robust calibration results ($\theta_{err} = \pm 1.0^{o}$) and simplifies integration by eliminating the need for signal conditioning to compensate for noise in electronic solutions like 3-axis accelerometers.

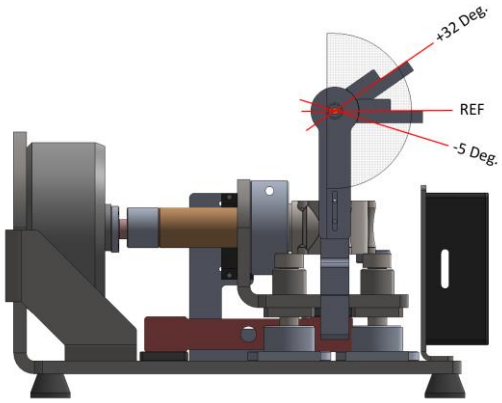

Figure 4.7: Collective Pitch Dial Guage

Code Implementation – Blade Pitch Angle Measurement

The Arduino Servo library was used to set and monitor the servo position. Servo position is obtained by converting the PWM (µs) into a 10bit range which is then scaled to degrees using a linear interpolation function (Eq. 4.1) as is shown in Table 4.3, below.

Table 4.3: Pitch Angle Interpolation

Description	Setpoint 1 / Min	Setpoint 2 / Max
Resolution (bit)		1024
Servo PWM Range, γ (µs)	1200	2500
Blade Pitch Angle, θ (Deg.)	– 5.0 (±1.0)	– 32.0 (±1.0)

$$\theta_{ix} = \theta_{min} + \left(\frac{\gamma_i - \gamma_{min}}{\gamma_{max} - \gamma_{min}}\right)(\theta_{max} - \theta_{min}) \qquad 4.1$$

Due to mechanical constraints of the pitch mechanism as well as blade specifications, pitch angle (θ_i) is limited to a maximum of $\theta_{max} \approx +32.0^{o} (\pm 1.0^{0})$.

Calibration Procedure

1. Set rotor speed to $N_r = 2500$ RPM,
2. TARE the load cell to zero thrust readout $T_r = 0.0$N,
3. Adjust indicated collective pitch (θ_i) so that $T_r \approx 0.0$N,

4. Install dial indicator and measure minimum / initial servo PWM output γ_{min} setpoint with indicated pitch set to $\theta_i \approx -5.0^o$,
5. Set $\theta_i \approx +32.0^o$ and measure servo PWM setpoint γ_{max},
6. Adjust constants θ_{max}, θ_{min} (44) so that serial outputs match indicated angles on dial,
7. Increment the angle to ensure readouts are accurate and repeatable.

SPECIAL NOTES & ASSUMPTIONS

- The angular displacement relationship between the servo and blade pitch mechanism is assumed to be linear,
- Pitch tolerances are defined as $\theta_i \approx \pm 1.0^o$ to compensate for servo linkage slop,
- The smallest theoretical pitch increment is limited to $\theta_i \approx \pm 0.17^o$ (180Deg. / 1024 bits).

4.1.6. Voltage and Current Measurement & Sensor Calibration

This section focuses on voltage and current measurement & calibration procedures of the rotor test system mentioned in §4.1 (P36). For efficiency purposes – raw data processing & signal conditioning methods are further outlined in §4.2.3 (P48). More information related to the function of the program and its operations are available in the project folder [55].

Current Measurement

A Winson MCS1500 Hall-effect current sensor with specifications outlined in Table 4.4 [58] was chosen to match the rated current specifications of the motor the BLDC motor shown in Figure 4.5, P39.

Figure 4.8: Winson WCS1500 [58]

Table 4.4: WCS1500 Specifications Overview

Description	Setpoint 1 / Min	Setpoint 2 / Max
Current Range (A)	0.0	200
Sensitivity (mV/A)	11	
Measurement Offset (V)	Vcc – 0.3	
Vcc Output Range (V)	0 – 5.0	

Voltage Measurement

A MAUCH HS-200-HV voltage sensor board with specifications outlined in Table 4.5 was used for voltage measurement. Despite its capacity for current measurement, noise interference led to calibration failures, as detailed on the manufacturer's website [59]. More information related to the function of the program and its operations are available in the project folder [55].

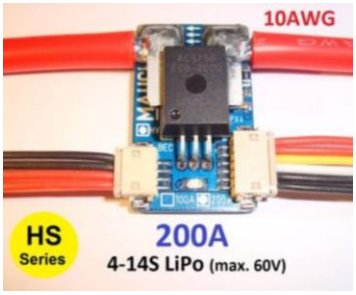

Figure 4.9: MAUCH HS-200-HV [59]

Table 4.5: MAUCH HS-200-HV Specifications

Description	Setpoint 1 / Min
Voltage Divider (mV/V)	18.111
Sensitivity (mV/V)	$\pm$0.1
Voltage Rating Measurement (V_{max}, V_{min})	0 – 60
Voltage Output Range (V_{cc})	0 – 3.3

Code Implementation – Voltage Measurement

Unless explicitly defined in the code, the Arduino ADC will automatically scale any analog input voltage according to the internal voltage reference $V_{ref} = 5.0$ V. The MAUCH HS-200-HV voltage divider configured to output $V_{cc} = 3.3$ V at $60V$ which is different to the Vcc of the WCS1500 current sensor. (Table 4.4)

A linear interpolation function was used to scale the 10bit analog pin voltage (A_{vi}) to voltage measurement range of the sensor (V_{max}, V_{min}), see Table 4.5.

Through trial and error in calibration, voltage measurements (V_{out}) were normalised by adding a theoretical offset $V_{max} = 20.0$ which equates to scaling $V_{out} = 1.67\ (5.0 \rightarrow 3.3\ V)$. This scaling step is required because the internal MAP function for IDE assumes $5.0V$ is 1024bit.

Code Implementation – Current Measurement

A current measurement library by A. Shamshiri [60] was integrated into the master program where current (I_{out}) is calculated according as shown below in Eq. 4.4.

Code Implementation – Power Measurement

A simple averaging function was used for sample conditioning for Current (I_{out}) and voltage (V_{out}) measurements. Power Output (P_{BLDC}) is then calculated according to Ohms law using Eq. 4.2.

$$P_{BLDC} = V_{out} \,.\, I_{out} \tag{4.2}$$

$$V_{out} = V_{max} + \left(\frac{(A_{vi} - A_{v1})}{(A_{v2} - A_{v1})}\right) (V_{max} - V_{min}) \tag{4.3}$$

$$I_{out} = I_{offset} - I_{ini} \tag{4.4}$$

Calibration Procedure

The rotor test bench was connected to a UNIT-T UTP 60V DC lab power supply in conjunction with a UNI-T UT207B Clamp meter and followed the following protocol.

1. Measure current and voltage I_{min} and V_{min} for $N_r \rightarrow 0\ RPM$,
2. Increment rotor speed $N_r = 500\ RPM$ and wait for sensor readings to stabilise.
3. Record the average indicated current (I_m) and voltage (V_m) from the DC power supply and multi-meter,
4. Repeat until $N_r \rightarrow 2500\ RPM$ (Table 4.1, P37),
5. Process measurements to obtain mean values from readings,
6. Adjust constants of linear interpolating functions (Eq. 4.3) and initial offsets.
7. Verify output readings from serial monitor.

SPECIAL NOTES & ASSUMPTIONS

- Sensors are assumed perfectly linear outputs as per manufacturers specifications [58, 61].
- Current tolerances are within $I_{out} \approx \pm 0.1$A,
- Voltage tolerances are within $V_{out} \approx \pm 0.1$V,

4.1.7. Rotor RPM Measurement & Calibration

BLDC motors operate generating a magnetic flux to either attract or repulse flux produced by permanent magnets installed on the rotor. As the magnet approaches a stator coil or pole-pair, the flux induces a back-EMF voltage pulse, and is produced for every pole pair present.

The APD F3-200 ESC can be configured to output pulses for electrical revolutions which are then converted to mechanical RPM (N_r) using the method described below. Specifications for motor constants are found in documentation on the manufacturers website. [62]

Code Implementation – RPM Measurement

Rotor head-speed is measured by determining the duration of each rotation using the ATmega328 internal clock as a time reference. Rotor speed N_r is updated for each program loop along with the current clock time (t_{clc}). When the IR sensor pin state is HI the time duration (Δt_d) is calculated as:

$$\Delta t_d = t_{clc} - t_{prev} \tag{4.5}$$

The motor constant (M_c) is calculated by dividing the number of poles (N_{poles}) by the number of stator pole pairs (N_{pairs}):

$$M_c = \frac{N_{poles}}{N_{pairs}} \tag{4.6}$$

Rotor speed (N_r) can then be calculated using the the product of the sample time t_s (µs) and motor constant (M_c) by dividing by the time duration (Δt_d) to complete a single revolution:

$$N_r = \frac{t_s M_c}{\Delta t_d} \tag{4.7}$$

Calibration Procedure

RPM readings were verified using a strobe light application from a mobile phone.

SPECIAL NOTES & ASSUMPTIONS

- Rotor speed tolerances are assumed to be within $N_r \approx \pm 10.0$ RPM of indicated measurements.

4.1.8. Thrust Measurement & Load Cell Calibration

Load cells are transducers that use strain gauges that allow the magnitude of external forces to be measured electronically.

Figure 4.10: MAVIN NA-50 Load Cell [63]

Common load cell configurations utilise a Wheatstone bridge strain gauge (Figure 4.10) comprised of 4 resistors. Using Ohm's Law, force magnitude is measured by calculating the difference between the reference excitation voltage and output voltage. An HX711 ADC amplifier is used to interface with the control system as outlined in [64]. More information related to the function of the program and its operations are available in the project folder [55].

Table 4.6: MAVIN NA-50 Specifications Overview

Description	Min	Max
Power Output (kW)	2	8
Motor Speed	0	6000
Rated Head Speed (rpm)		3000
Blade Pitch Angle (Deg.)	- 5.0 (±1.0)	+35.0 (±1.0)
Load Capacity (Kg)		50 (±0.01)
Construction	Stainless Steel & Aluminium	
Gear Ratio	1:1	

Code Implementation – Thrust Measurement

In the master program, the load cell is initialised using the calibration factor as obtained previously. Even though the rotor produces a gyroscopic forces counter torque moments (§2.3.2, P29) produced by the drivetrain, a small resultant force is still registered by the load cell requiring the reading to be zeroed after the head speed is reached.

Calibration Procedure

The calibration factor is obtained using an automated utility available in the standard HX711 library [64].

1. Tare the load cell with no external load,
2. Place a calibrated mass of 100g on the load cell,
3. Obtain calibration factor from serial monitor,

4. Repeat 10 times to obtain a median value.

4.2. Test Methodology & Data Processing Workflow

As processing & conditioning data outputs from experimental rotor tests are closely related to MATLAB simulations and later comparisons, both sections are combined in this section and discussed respectively for the sake of simplification.

4.2.1. Test Sample Collection

Three blade sets were tested at constant speed ($N_r = 1000 \rightarrow 2500\, rpm$) with a collective pitch of $\theta_{ix} = 0^o - 14^o$ to observe how power consumption changes with varying blade pitch angles. Sample data was processed and conditioned in MATLAB before being compared to BEMT approximations outlined in §4.4 (P52). The sample collection and processing procedure is summarized below.

1. Set rotor to specific speed with $\theta_{ix} = 0^o$,
2. TARE load cell to zero readout $T_r, = 0.0$kg
3. Collect $n_I, \geq 10$ samples for ($V_{sm}, I_{sm,} T_{sm}, \theta_{ix}$) at pitch increment θ_{ix} ,
4. Increase pitch $\theta_{ix} + 0.25^o$ and repeat for $\theta_{ix} = 0^o \rightarrow 14^o$,

Samples are imported into MATLAB where a 4th degree polynomial curve fitting method is used to extrapolate mean values of all measured variables (V_{BLDC} , P_{BLDC}, T_{BLDC} , I_{BLDC}, θ_r) to calculate rotor shaft output power and is discussed in §4.4 (P52).

4.2.2. Initial Rotor Power Output

The BEMT rotor model only considers aerodynamic forces acting of the rotor blades – thus only the theoretical rotor power output (P_{BEMT}) is considered at the rotor shaft. To compare power outputs of the BEMT model to experiments, the initial power (P_{ini}) demand required to operate the test bench must be determined. Given that tests are performed at constant speed, momentum is conserved (§3.4, P33), thus the contribution to increased power demands are purely related to the effort (current draw) from the motor to maintain constant speed when subjected to increasing aerodynamic forces.

To isolate losses from the drivetrain (inertia, friction etc.), an initial test is performed with rotor blades removed to establish a baseline actual rotor shaft power output P_{ini} assuming gearbox efficiency $\eta_g = 98\,\%$.

Table 4.7: T-Motor V10L Motor Constants [65]

R_m (Ω)	I_o (A)	I_{max} (A)	K_v (RPM/V)	η_{bldc} (%)
0.008	4.4	196	170	94.0

Table 4.7 shows BLDC motor efficiency η_{bldc} calculated according to Hendershot and Miller [66] employing motor constants obtained from manufacturer specifications.

$$P_{ini} = P_{BLDC}\,.\,\eta_{sys} = constant \tag{4.8}$$

$$P_{BLDC} = V_i I_i \tag{4.9}$$

$$\eta_{sys} = \eta_g\,\eta_{BLDC} \tag{4.10}$$

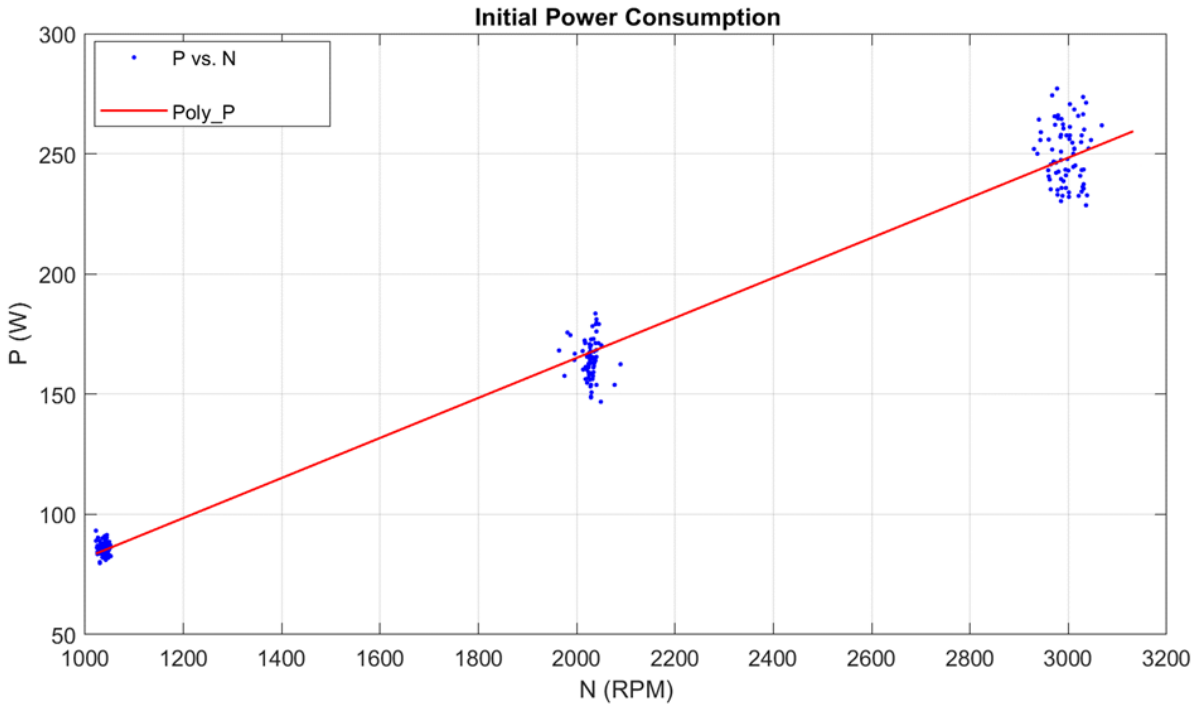

Figure 4.11: inital Power Consumption

As shown in Figure 4.11, three tests are performed to establish power output P_{BLDC} for rotor from $N_r = 1000 \rightarrow 3000\ rpm\ where\ n_I \geq 50$. then calculates mean values for the supply voltage to the ESC and current draw (V_{BLDC}, I_{BLDC}) according to Eq. 4.11. A 1st degree polynomial fitting method is then used to normalize (Eq. 4.11) according to $P_{ini} = p(x) = \sum_{k=0}^{n} p_k x^k$ shown in Table 4.8, below.

$$p(x) = 0.08316x - 1.32 \tag{4.11}$$

Table 4.8: Initial Power Consumption

N_r (rpm)	V_{BLDC}	I_{BLDC} (A)	P_{BLDC} (W)	P_{ini} (W)	η_{sys} (%)
1038.18	49.75	1.72	85.51	78.44	
2027.35	49.50	3.33	164.60	151.62	92.12
2995.90	49.31	5.05	249.04	229.42	

From Eq. (Eq. 4.12), power demand (P_{Ro}) resulting from drag forces acting on the rotor blade can be isolated and compared to the BEMT approximation (P_{BEMT}) shown in Table 4.9 where the observed error was $\Delta_{mean\ err} \approx 8\%$.

$$P_{Ro} = P_{sample\ (\theta_r=0^o)} - P_{\text{ini}\ (\theta_r=0^o)} \quad 4.12$$

Table 4.9: Rotor Blade B02, $N_r = 3000rpm, P_{ini} = 249.04W$

θ_r (Deg.)	η_{sys} (%)	P_{ini} (W)	P_{sample} (W)	P_{BEMT} (W)	P_{Ro} (W)	Δ_{err} (%)
0	0.93	249.04	277.24	11.76	9.07	-23.0
5			291.73	27.90	22.56	-19.0
10			397.27	91.45	120.82	32.0
13			453.46	159.82	173.13	8.0
***Tabulated data shortened for conciseness**					$\Delta_{mean\ err}$	**-8.0**

4.2.3. Sample Pre-Processing and Signal Conditioning

MATLAB is used to process raw sample data ($T_{sm}, I_{sm}, V_{sm,}, \theta_{ix}$) to calculate the indicated power consumption (Eq. 4.15) and thrust (Eq. 4.16) by the rotor system as illustrated in Figure 4.12, P50.

Over the duration of a test run for a single set of blades, voltage drop was observed to be consistently small ($\Delta V_{err} = 2 - 2.5\%$). Mean voltage, V_m (Eq. 4.13**)** is calculated by averaging accumulated raw samples V_{sm} for duration of the test run (n_p) at a constant speed of N_r using:

$$V_m = \frac{V_{sm}}{n_p},\ where\ n_p = sample\ range \quad 4.13$$

As blade pitch (θ_{ix}) increases, more work is done by the rotor to move air, consequently leading to higher current demands from the motor to maintain speed. Mean current (I_m) is calculated at each pitch increment (θ_{ix}) from:

$$I_m = \frac{I_{sm}}{n_I}\ \ at\ \theta_{ix}\ where\ n_I \geq 10 \quad 4.14$$

Where n_I is the sample range collected at increment θ_{ix}.

Using the mean voltage (Eq. 4.13) and current (Eq. 4.14), rotor power output (P_s) can then be calculated by applying Ohm's Power Law:

$$P_s = V_m I_m,\ at\ \theta_{ix} \tag{4.15}$$

Using the same sample range for Eq. 4.16, Rotor thrust T_r is calculated by converting mean thrust (T_{sm}) samples accumulated at increment θ_{ix} into Newtons ($g = 9.810\ m/s^2$) and then averaging over n_I (21):

$$T_r = \frac{gT_{sm}}{n_I},\ at\ \theta_{ix}\ where\ n_I \geq 10 \tag{4.16}$$

Due to the 10bit resolution limitation of the *ATmega 328* microcontroller used in the Arduino Nano, the indicated pitch angle resolution was limited to $\theta_{ix} \pm 0.25^o$. Discrete outputs of θ_{ix} that didn't correspond to integers ($\theta_{ix} \notin Z$) were approximated in MATLAB by applying a 3rd degree polynomial curve fitting method [28] as it was challenging to perform a direct comparison to theoretical approximations described in §3.1 (P31). The polynomial form is represented as $\theta_i(x) = p(x) = \sum_{k=0}^{n} p_k x^k$ (Eq. 4.17). Results for thrust and power consumption (T_{Poly}, P_{Poly}) were obtained as shown in Figure 4.12, P50.

$$p(x) = p_n x^n + p_{n-1} x^{n-1} + \ldots + p_2 x^2 + p_1 + p_0 \tag{4.17}$$

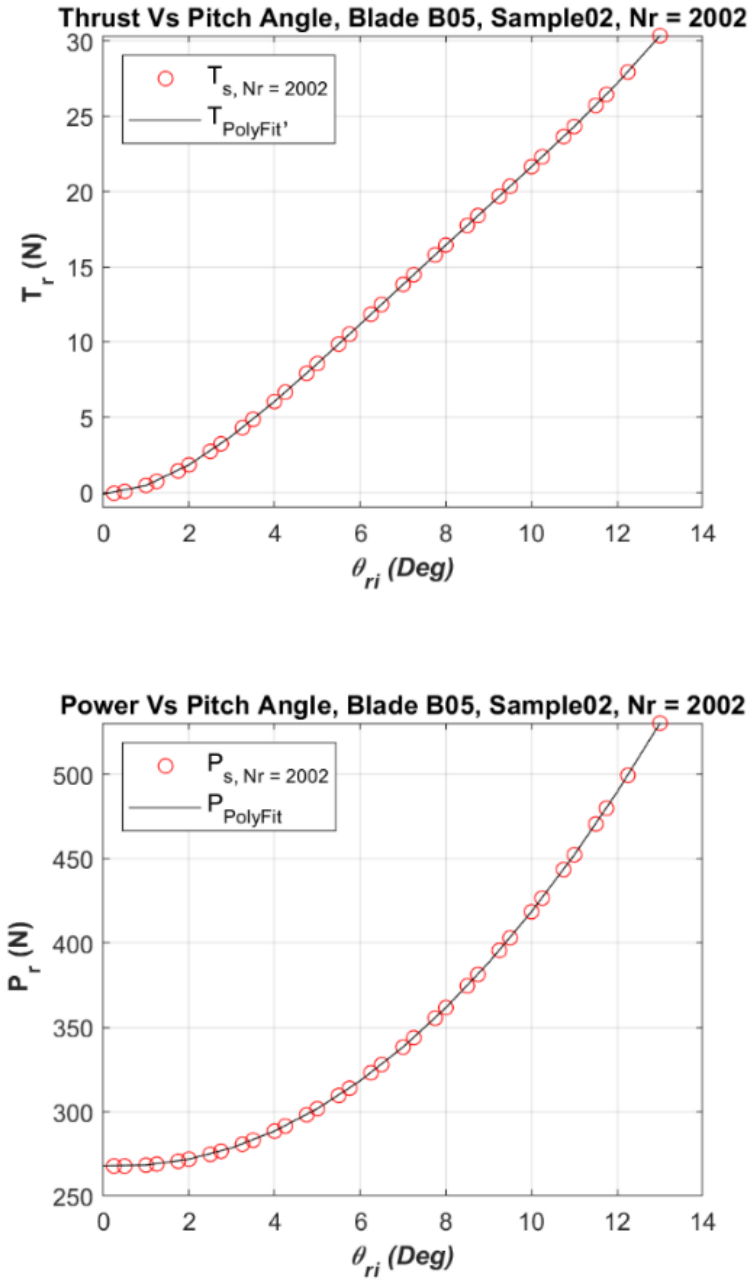

Figure 4.12: Thrust & Power VS Pitch Angle

4.3. XFOIL Airfoil Analysis

Analysing the theoretical performance characteristics of rotors (§4.2.2, P46) necessitated the development of a two-step method. The first step being empirical validation as discussed in §4.2, the second focuses on modelling a rotor system that represents the test environment which will enable direct performance comparisons to be made. The BEMT rotor model is dependent on airfoil lift and drag coefficients (§3.3, P32) matching the test environment in which Re, $M_B = const$, XFOIL performs a polar analysis (Figure 4.13) of the airfoil, accumulating lift and drag coefficients at pitch angles θ_{ix}. MATLAB [67] then evaluates the performance (§4.5,

P53) of the BEMT rotor model (§3, P31) using data defined in Table 4.2, (P38) and the output from XFOIL. More information related to the function of the program and its operations are available in the project folder [55].

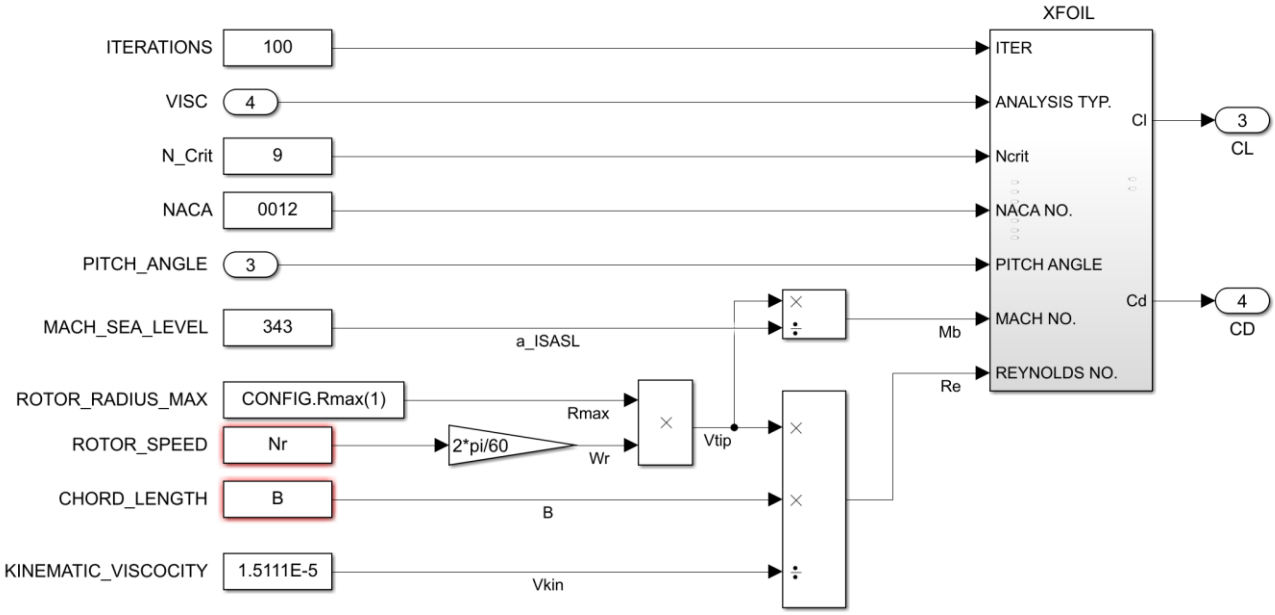

Figure 4.13: XFOIL Analysis Illustrative Workflow

The illustration depicted in Figure 4.13 outlines the workflow of variables and configuration parameters required by XFOIL to perform an air foil analysis. Following below are the respective commands which configure XFOIL to perform a polar accumulation to calculate lift and drag coefficients, (C_l, C_d) also shown in an example Figure 4.14 (P52). Further details relating to definitions are available in the associated XFOIL documentation [49].

1. NACA – Airfoil number (Table 4.2, P38)
2. OPER: Operation selection,
3. ITER: Number iterations = 100,
4. VISC – Set viscous analysis mode to active,
5. RE – Input Reynolds Number (Re),
6. MACH – Set Critical Mach number (a_B),
7. SEQP – Select sequential polar analysis mode,
8. PACC – Set to polar accumulation active,
9. ASEQ – Set pitch angle range and increment ($0^o \rightarrow 13^o, \theta_{ix} + 1.0^0$),

Reynolds number is determined from $Re = V_r B / v_{kin}$, where $v_{kin} = 1.5111E^{-5}$ (kinematic viscosity of air at ISASL), tip velocity $V_r = \omega_r R_{max}$ and chord length B (Table 4.2, P38). The

Mach number is calculated from $a_B = V_r/a_{ISASL}$, where the Mach number for air at sea level is $a_{ISASL} = 343\ m/s$. XFOIL then proceeds to accumulate the lift and drag polars according to the command configuration an example is show in Figure 8.1.

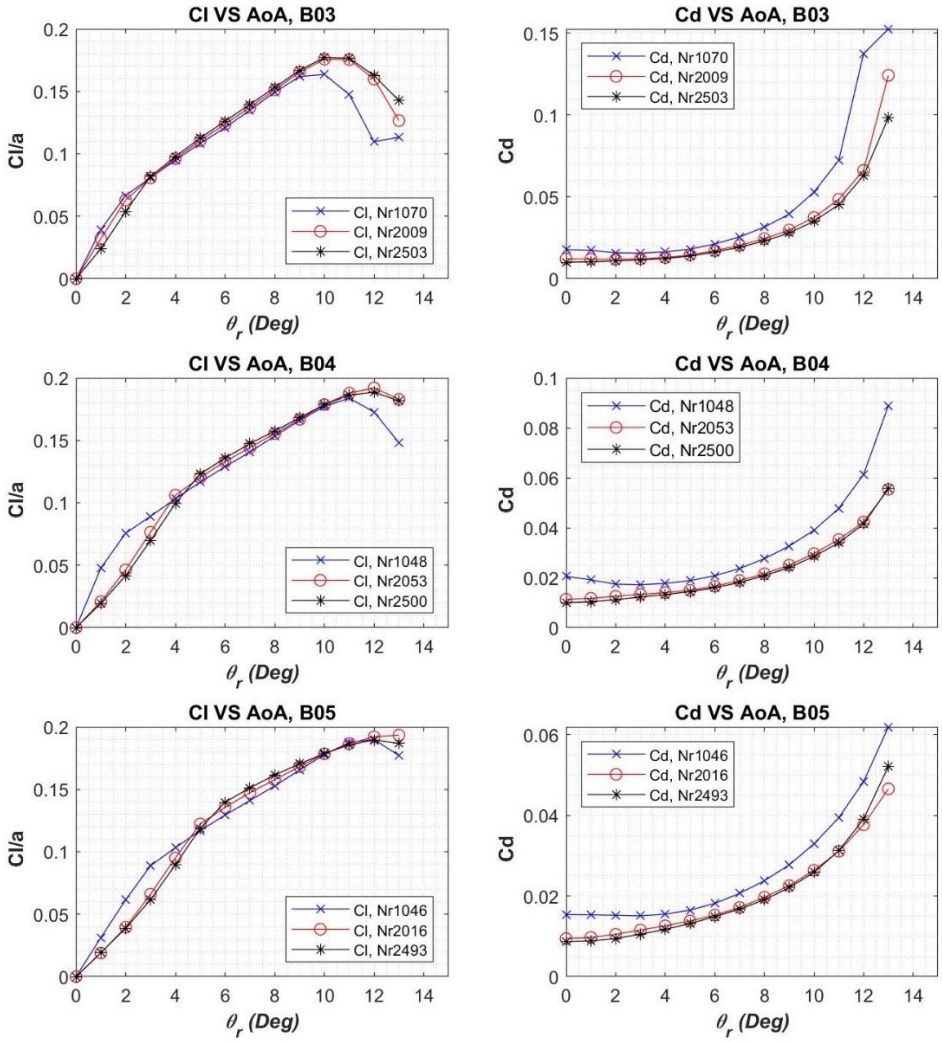

Figure 4.14: XFOIL Lift & Drag Polar Accumulation Plots

4.4. Rotor Modelling

Rotor thrust and power output is determined for each pitch increment of $\theta_{ix} = 1.0^o$ using a MATLAB-based rotor model described in §3 (P31). Code originally developed by Bell [29] was extensively modified to integrate XFOIL outputs and optimized to automatically accumulate sequential calculations as illustrated in Figure 4.15 (P53).

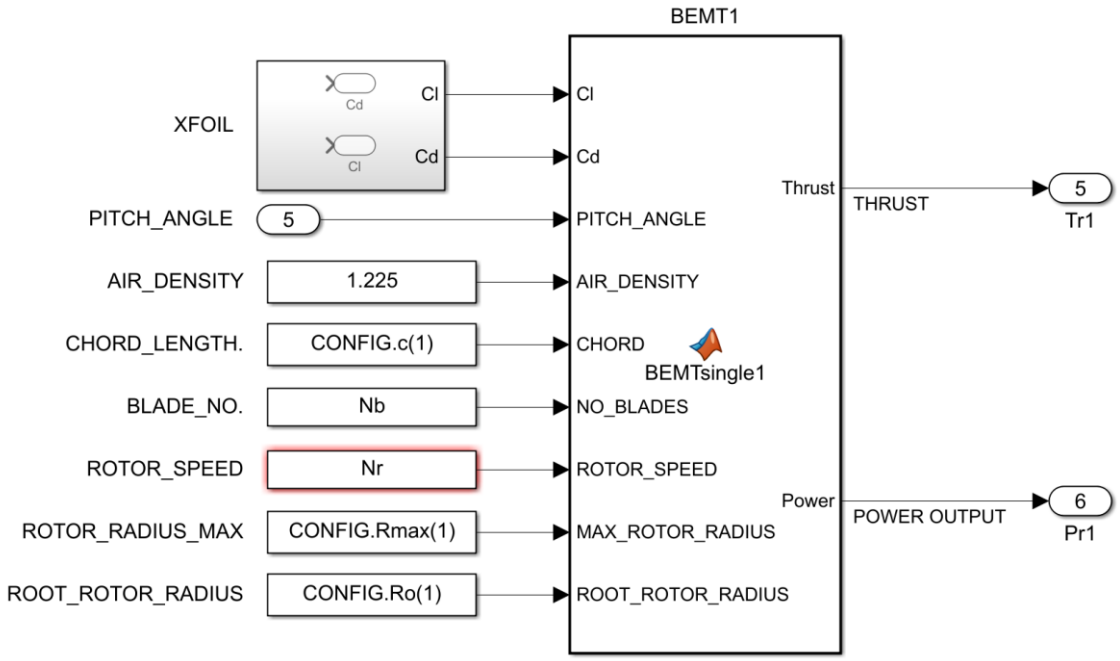

Figure 4.15: MATLAB Modelling Illustrative Workflow

The analysis method follows the respective steps below according to the workflow illustrated in Figure 4.1, P35.

1. Import lift and drag coefficients from XFOIL text file,
2. Define blade specifications (Table 4.2, P38),
    i. Number of blades N_b,
    ii. Rotor Max Radius R_{max} (m),
    iii. Rotor root radius R_o (m),
    iv. Chord length B (m),
3. Air density, $\rho_{ISASL} = 1.225\ kg/m^3$,
4. Pitch angle range, $\theta_{ix} = 0^o - 13^o$ (deg),
5. Rotor Speed N_r (r/s).

4.5. Performance Comparisons – BEMT Vs. Experiments

The primary goal of this work is to accurately simulate a scalable quadrotor platform with a variable pitch rotor system, using the Blade Element Momentum Theory (BEMT) rotor model. This model, which interacts with the flight control system, aims to closely emulate real-world behaviour. The performance of this model is evaluated based on its ability to match empirical data, specifically thrust, and power comparisons. This data will later inform the formulation of

a basic framework for boundary conditions and payload capacity limitations, as discussed further in §6. P70).

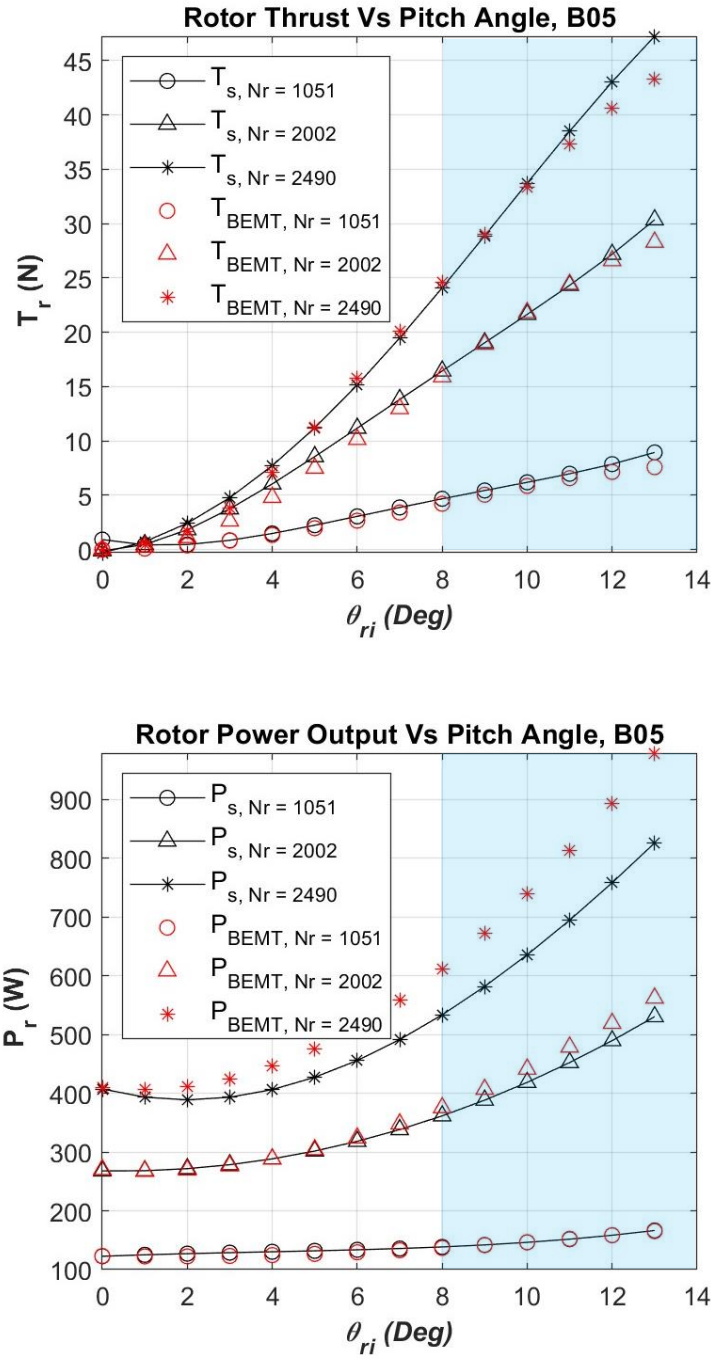

Figure 4.16: Rotor Performance Comparison, B05

Following the meticulous methodology outlined in earlier in §4.2, P46, three sizes for rotors (Table 4.2, P38) were tested at various speeds. Sample data is collected and processed in MATLAB. For consciousness the comparison of B05 is shown (Figure 4.16, P54), plots for

B03 & B04 are shown in Appendix D and E. Further interesting findings related to comparisons are summarized in §7, P80.

4.5.1. Thrust Comparison

As can be seen in Figure 4.16, theoretical approximations for thrust output by BEMT and XFOIL closely matched experimental data (T_{BEMT}, T_{sample}) at speeds ($N_r = 1000 \rightarrow 2500$ rpm) and rotor pitch angles ($\theta_i = 0^o \rightarrow 13^o$) for all rotor blades tested (Table 2). The consistency of the MATLAB-based rotor model's performance, particularly in terms of thrust and power output, is noteworthy when considering the variations in geometry and speeds that were tested.

This consistency implies that the simulated environment in MATLAB closely aligns with the conditions observed in the experimental tests. In other words, the results obtained from the MATLAB simulation closely resemble those obtained from physical testing. This alignment suggests that the simulated and real-world environments share a high degree of similarity, indicating the dependability and precision of the MATLAB model in predicting the thrust performance of the rotor system.

4.5.2. Power Output Comparison

Operating rotor blades at speeds $N_r \approx 1000 \rightarrow 2000$ rpm, theoretical power consumption estimates (P_{BEMT}**)** were observed to follow experimental test results (P_{sample}), as $P_{sample} \approx P_{BEMT}$ within a pitch range of $\theta_i = 0^o \rightarrow 7^o$. At larger pitch angles ($\theta_i \approx 7^o \rightarrow 13^o$), theoretical power outputs are overestimated ($P_{BEMT} > P_{sample}$) for all rotor blades tested at all speed ranges. To try and establish deviations observed for power output mentioned prior, a further investigation was conducted and published in parallel to this work relating to "*XFOIL Performance Validation for Medium-Scale Variable Pitch UAV Rotor Systems*". [1]

5. MODELLING & SIMULATION

This section introduces how the quadrotor control laws (§2, P26) are integrated with the variable pitch BEMT (§3.1, P31) rotor systems within the Simulink environment. Information relating to boundary conditions, settings and comparisons are detailed further in §6 (P70).

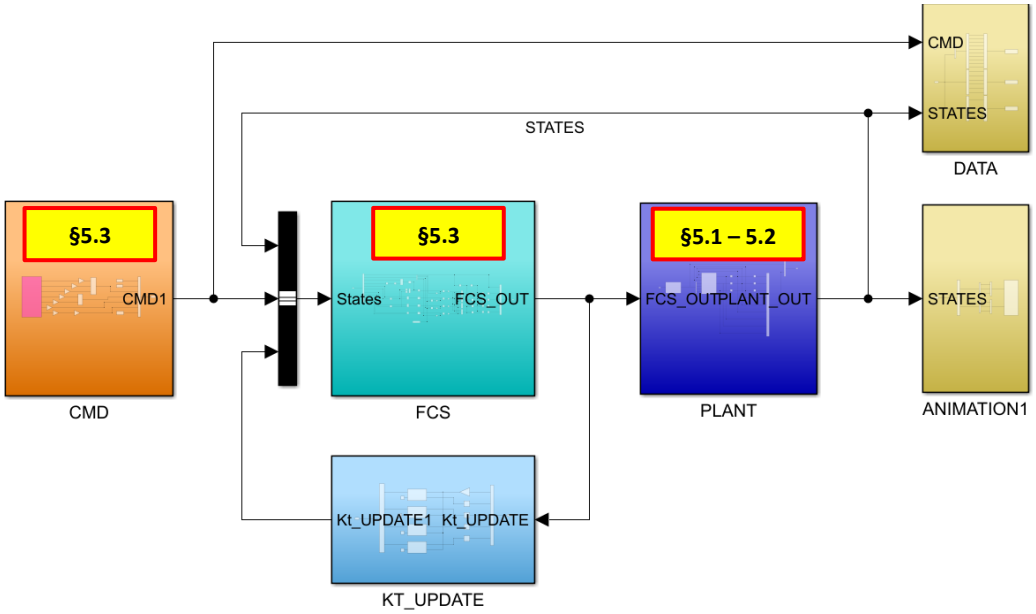

Figure 5.1: Control System Architecture Overview

The illustrations shown in Figure 5.2 provides a high-level overview of the control system model architecture and state flows used in this work. A brief explanation of each function blocks follows below in reference to Figure 5.1,

1. **CMD:** Outputs trajectory coordinates, body orientation, and rotor head speed states to **FCS**,
2. **FCS:** Given input from CMD and FCS, PID control loops then update rotor pitch angle states to **PLANT**,
3. **PLANT:** From FCS, body force vectors are updated from which angular states of the body relative to the body coordinate (BCS) reference. Linear states are then approximated for the displacement, velocity, and acceleration and converted to the world reference coordinate (WCS) system using Euler-Lagrange rotations.
4. **KT-UPDATE:** BEMT rotor model updates thrust and torque coefficients – used to stabilize model performance.

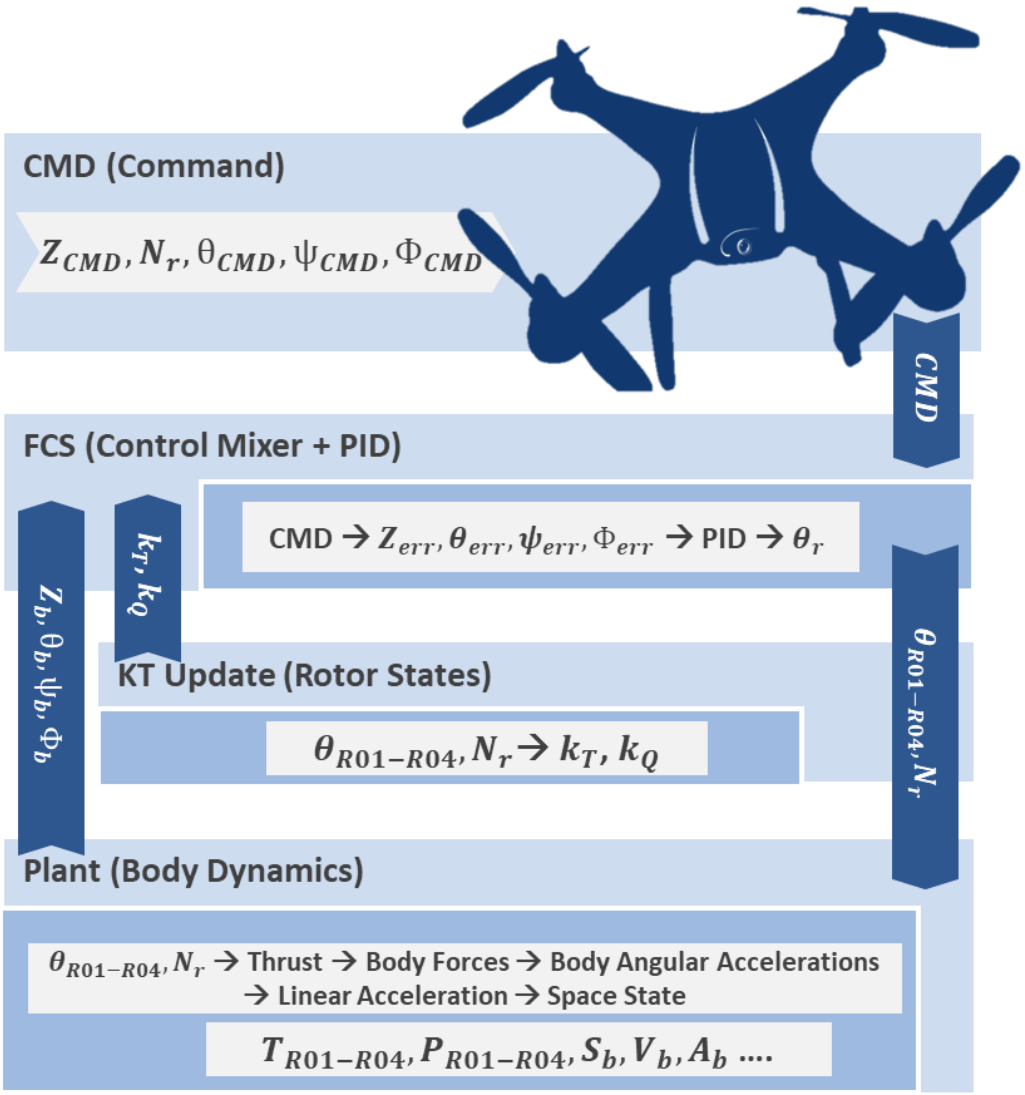

Figure 5.2: Simulink Control System Model

Before discussing details related to the architecture, it will be noted that the control architecture is referenced from related works Carrillo and Ferry [50, 51] in this work (Figure 5.1) was extensively modified to integrate variable pitch rotor elements aimed at achieving the scope defined in §6.1 (P70). Advanced trajectory tracking and correction functionality which relies on use of accelerometers, gyros, barometers are omitted for simplicity.

5.1. Body Forces & Angular States

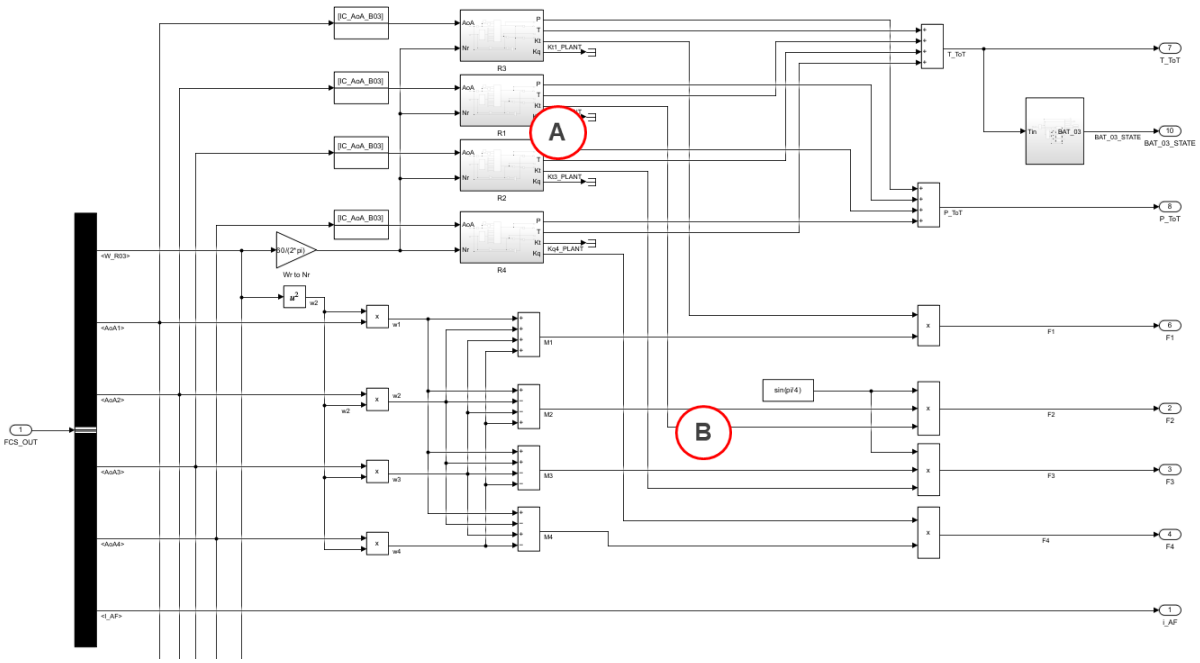

Figure 5.3: Simulink Body Force Model

5.1.1. Body Forces

Quadrotors are considered 6-DOF (degrees of freedom) systems by being able to translate and rotate $(\phi_b, \theta_b, \varphi_b)$ about $X_b|Y_b|Z_b$ axes. In a hovering state where $[\dot{X}_b \quad \dot{Y}_b \quad \dot{Z}_b]^T = 0.0\ m/s$, and $Z_b = constant$, thrust forces oppose gravity so that $T_f = F_4 = m_b g - m_b \ddot{Z}_b$. Altitude Z_b thus depends on the magnitude F_4. In this work it is assumed that a single power unit drives all variable pitch rotor systems, thus $\omega_r = constant$. Thrust along the Z_b axis varies with pitch θ_r, altering coefficients k_r, therefore $T_f = f(\omega_r, \theta_{r_i} k_{r_i})$ as Eq. 5.1 shows [51]. The fixed pitch thrust term in Eq. 2.1 and 2.6 can then be written as,

$$T_f = \omega_r^2 \sum_{i=1}^{4} \theta_{r_i} k_{r_i}, \; T^B = \begin{bmatrix} 0 \\ 0 \\ \omega_r^2 \left(\theta_{r_1} k_{r_1} + \theta_{r_2} k_{r_2} + \theta_{r_3} k_{r_3} + \theta_{r_4} k_{r_4}\right) \end{bmatrix} \qquad 5.1$$

Table 5.1: Thrust and Moment Equations, Fixed Pitch Vs Varaible Pitch

Des.	Constant	Variable	Altitude Cont.
Fixed Pitch	k_{r_i}	ω_{r_i}	$T_f = k_{r_i} \sum_{i=1}^{4} \omega_{r_i}$ $\tau_b = l k_{r_i} \sum_{i=1}^{4} \omega_{r_i}$
Variable Pitch	ω_{r_i}	θ_{r_i}, k_{r_i}	$T_f = \omega_r^2 \sum_{i=1}^{4} k_{r_i} \theta_{r_i}$ $\tau_b = l\omega_r^2 \sum_{i=1}^{4} q_{r_i} \theta_{r_i}$

****Note: Equations in this table are intended to aid in explanation and therefore not numbered. For $\omega_{r_i}, i \rightarrow$ rotor number.**

Roll, Pitch and Yaw orientation $(\phi_b, \theta_b, \varphi_b)$ for the quadrotor about the $X_b|Y_b|Z_b$ axes is dependent on the moments (τ_b) resulting from thrust forces acting at length l (Figure 5.4).

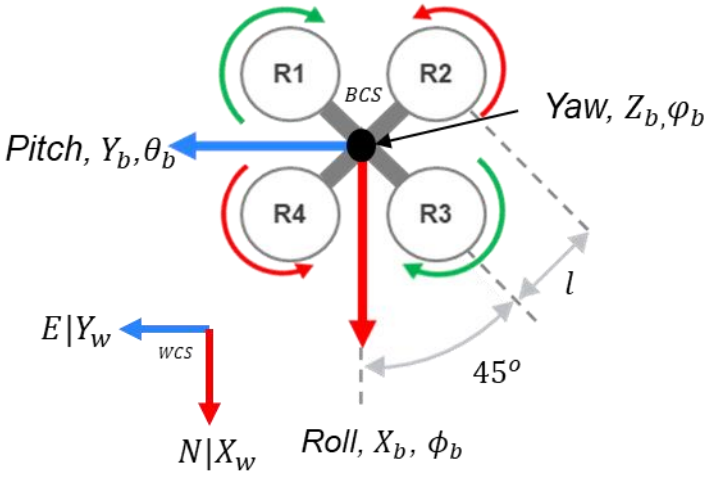

Figure 5.4: Quadrotor Motion & Orientation

Using hover assumption mentioned earlier, angular moments are $[\tau_\phi \quad \tau_\theta \quad \tau_\varphi]^T = f(\omega_r, \theta_{r_i} k_{r_i}, l, q_{r_i})$ which means the general form is changed so that $\tau_b = T_f l = cl\theta_{r_i}\omega_r^2$ $(c \rightarrow k_i, q_i)$, thus Eq. 2.7 becomes,

$$\tau_b = \begin{bmatrix} \tau_\phi \\ \tau_\theta \\ \tau_\varphi \end{bmatrix} = \begin{bmatrix} Sin\left(\frac{\pi}{4}\right) l\omega_r^2 \ (\theta_1 k_1 - \theta_2 k_2 - \theta_3 k_3 + \theta_4 k_4) \\ Sin\left(\frac{\pi}{4}\right) l\omega_r^2 \ (\theta_1 k_1 + \theta_2 k_2 - \theta_3 k_3 - \theta_4 k_4) \\ \omega_r^2 \ (\theta_1 q_1 - \ \theta_2 q_2 + \theta_3 q_3 - \theta_4 q_4) \end{bmatrix} \qquad 5.2$$

In this work, linearized forms of Eq. 5.1 and 5.2 are used in the model (Figure 5.3) and are referenced in Table 5.2 [51].

Table 5.2: Linearized Equations Of Moiton

Des.	Axis	Unit	Equations of Motion	
Climb Thrust	Z_b	N	$U_1 = \omega_r^2\ (\theta_1 k_1 + \ \theta_2 k_2 + \theta_3 k_3 + \theta_4 k_4)$	5.3
Roll Thrust	ϕ_b		$U_2 = Sin\left(\frac{\pi}{4}\right) \omega_r^2\ (\theta_1 k_1 - \theta_2 k_2 - \theta_3 k_3 + \theta_4 k_4)$	5.4
Pitch Thrust	θ_b		$U_3 = Sin\left(\frac{\pi}{4}\right) \omega_r^2\ (\theta_1 k_1 + \theta_2 k_2 - \theta_3 k_3 - \theta_4 k_4)$	5.5
Yaw Thrust	φ_b		$U_4 = \omega_r^2\ (\theta_1 q_1 - \ \theta_2 q_2 + \theta_3 q_3 - \theta_4 q_4)$	5.6
Roll Torque	ϕ_b	$N.m$	$\tau_\phi = Sin\left(\frac{\pi}{4}\right) l\omega_r^2\ (\theta_1 k_1 - \theta_2 k_2 - \theta_3 k_3 + \theta_4 k_4)$	5.7
Pitch Torque	θ_b		$\tau_\theta = Sin\left(\frac{\pi}{4}\right) l\omega_r^2\ (\theta_1 k_1 + \theta_2 k_2 - \theta_3 k_3 - \theta_4 k_4)$	5.8
Yaw Torque	φ_b		$\tau_\varphi = \omega_r^2\ (\theta_1 q_1 - \ \theta_2 q_2 + \theta_3 q_3 - \theta_4 q_4)$	5.9

****Note: Yaw force $U_4 = \ \tau_\varphi\ since\ \dot{\omega_i^2} = 0$ as per Eq. 2. 1**

FCS outputs pitch angles for rotors, θ_{ri} and rotor speed N_r which are passed to and the actuator block (See B, Figure 5.3) to calculate the forces ($U_{1\ \rightarrow\ 4}$) acting on the body using Eq. 5.3 – 5.6.

5.1.2. Actuator Forces

Shown in Figure 5.3 (A), the magnitude of body forces (Eq. 5.3 – 5.6) are dependent on the thrust generated by rotors and must satisfy the general thrust equation $f_i = k\omega_i^2$ (Eq. 2.6) which are required to calculate angular accelerations later (§5.1.3, P62). For a given inputs, $\theta_{ri}\ N_r$, the BEMT rotor model (§3.1, P31) solves for k_i and q_i (Eq. 5.12, 5.13) using lookup tables to interpolate C_l, C_d ($Range\ of\ \theta_{ri} = 0^o \rightarrow 13^o$) and constants shown in Eq. 5.10 5.11. (Figure 5.5).

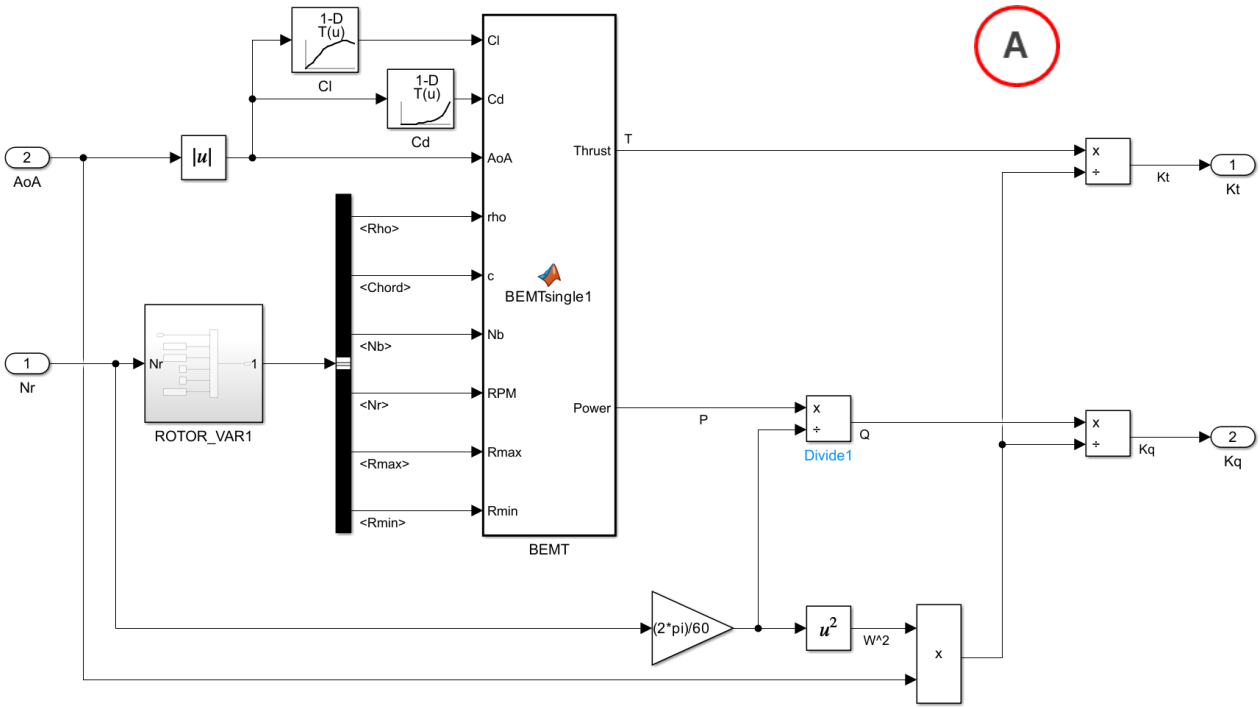

Figure 5.5: Simulink Actuator Force Model

Notes With Regards To Simulink Rotor Model Parameters

- $B, n_b, R_{max}, R_{\min}$ are referenced from rotor geometry specified in Table 4.2, P38,
- Air density $\rho_{ISASL} = 1.225\ kg/m^3$ and is assumed to be constant.
- Lookup tables for C_l, C_d are referenced from the XFOIL airfoil analysis (§4.3, P53) which was conducted for the rotor performance experiments.
- Coefficients k_{r_i}, q_{r_i} are in the form $[k_{r_i}, q_{r_i}]/\theta_{ri}$ where θ_{ri} is cancelled out during the calculation of body forces shown in Eq. 5.3 – 5.6 to satisfy Eq. 2.6. Variable θ_{ri} can thus be considered as a magnitude used to convey rotor thrust force magnitudes to the PLANT body dynamics models shown in §5.1.3 below.

Table 5.3: Actuator Force Equations

Des.	Sym.	Unit	Function	
Thrust	T_{ri}	N	$T_{ri}, P_{ri} = f(N_r, C_l, C_d, \rho_{ISASL}, B, n_b, R_{max}, R_{\min})$	5.10
Power	P_{ri}	W		5.11
Torque Coeff.	q_i	–	$q_i = \tau_{ri}/\theta_{ri}\omega_r^2$	5.12
Thrust Coeff.	k_i	–	$k_i = T_{ri}/\theta_{ri}\omega_r^2$	5.13

5.1.3. Angular Displacement, Velocity & Acceleration

With body forces vectors (§5.1.1 - 5.1.2) acting on the body defined, angular displacement, velocity and accelerations are be calculated as shown in Figure 5.6 (A – C).

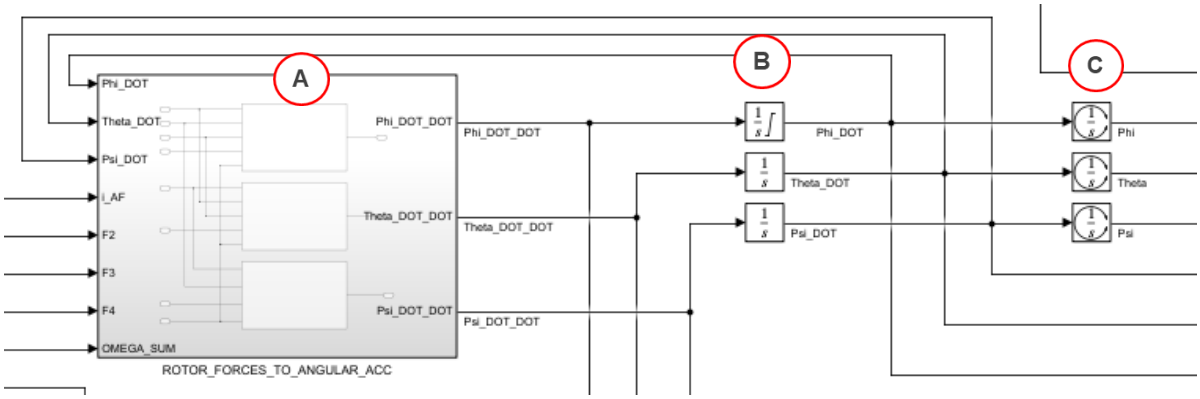

Figure 5.6: Simulink Angular Acceleration Model

Angular accelerations ($\ddot{\phi}, \ddot{\theta}, \ddot{\varphi}$) acting on the body are a function of gyroscopic effects induced by body and rotor mass inertia as well as torques induced during changes in orientation as the vectorized form shows in Eq. 5.14 (Table 5.4). [51]

$$\begin{bmatrix} \ddot{\phi} \\ \ddot{\theta} \\ \ddot{\varphi} \end{bmatrix} = \begin{bmatrix} \frac{(I_{yy}-I_{zz})\dot{\theta}\dot{\varphi}}{I_{xx}} \\ \frac{(I_{zz}-I_{xx})\dot{\phi}\dot{\varphi}}{I_{yy}} \\ \frac{(I_{xx}-I_{yy})\dot{\phi}\dot{\theta}}{I_{zz}} \end{bmatrix} - J_r\omega_r \begin{bmatrix} \frac{\dot{\theta}}{I_{xx}} \\ -\frac{\dot{\phi}}{I_{yy}} \\ 0 \end{bmatrix} + \begin{bmatrix} \frac{\tau_\phi}{I_{xx}} \\ \frac{\tau_\theta}{I_{yy}} \\ \frac{\tau_\varphi}{I_{zz}} \end{bmatrix} \qquad 5.14$$

Shown in Figure 5.6 (A), body torques ($\boldsymbol{\tau_\phi, \tau_\theta, \tau_\varphi}$) are calculated given inputs ($\boldsymbol{F_{1\to4}}$, $\boldsymbol{I_{xx}}$, $\boldsymbol{I_{yy}}$, $\boldsymbol{I_{zz}}$, $\boldsymbol{J_r}$, $\boldsymbol{\omega_r}$) according to Eq. 5.7 – 5.9 after which angluar accelerations are determined from Eq. 5.15, 5.18 and 5.21 (Table 5.4).

Table 5.4: Linearized Equations for Angular Motion

Des.	Axis	Unit	Equations of Motion	
Roll Acc.		Rad/s^2	$\ddot{\phi}_b = \frac{(I_{yy}-I_{zz})\dot{\theta}\dot{\varphi}-J_r\omega_r\dot{\theta}+lU_2}{I_{xx}}$	5.15
Roll Vel.	ϕ_b	Rad/s	$\dot{\phi}_b = \int \ddot{\phi}_b$	5.16
Roll Dis.		Rad	$\phi_b = \int \dot{\phi}_b$	5.17
Pitch Acc.		Rad/s^2	$\ddot{\theta}_b = \frac{(I_{zz}-I_{xx})\dot{\phi}\dot{\varphi}-J_r\omega_r\dot{\phi}+lU_3}{I_{yy}}$	5.18
Pitch Vel.	θ_b	Rad/s	$\dot{\theta}_b = \int \ddot{\theta}_b$	5.19
Pitch Dis.		Rad	$\theta_b = \int \dot{\theta}_b$	5.20
Yaw Acc.		Rad/s^2	$\ddot{\varphi}_b = \frac{(I_{xx}-I_{yy})\dot{\phi}\dot{\theta}+U_4}{I_{zz}}$	5.21
Yaw Vel.	φ_b	Rad/s	$\dot{\varphi}_b = \int \ddot{\varphi}_b$	5.22
Yaw Dis.		Rad	$\varphi_b = \int \dot{\varphi}_b$	5.23

Integration is performed to calculate angular velocity (Eq. 5.16, 5.19, 5.22) and angular displacement (Eq. 5.17, 5.20, 5.23) states respectively as illustrated in Figure 5.6 (B→C). (Table 5.4)

Notes With Regarding Airframe and Rotor Inertia Approximations

- To simplify the evaluation outlined in §6 (P70), pitch distance between rotors is fixed. Airframe density is assumed to uniform as to enable different payloads (m_{af}) capacities to be evaluated more efficiently. A symmetrical airframe geometry about X|Y-Axes ($I_{xx} = I_{yy}$) with 3 different masses was modeled in Solidworks from which inertia (I_{xx}, I_{yy}, I_{zz}) was measured. Given airframe geometry is constant, inertia will vary linearly for the given input m_{af} (Figure 5.7) where $I_{xx,yy} = 0.0228m_{af} + 2.0e^{-4}$ and $I_{zz} = 0.0193m_{af} + 7.0e^{-5}$, refer to Appendix J.

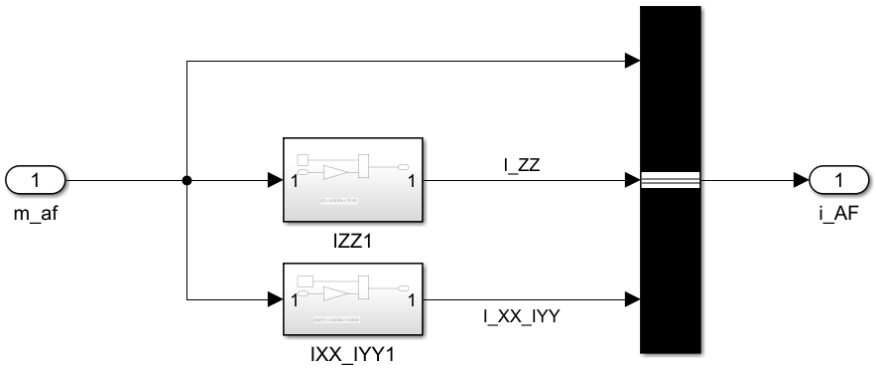

Figure 5.7: Simulink Airframe Inertia Model

- Given the complexity of the variable pitch rotor linkage system, rotor inertia (J_r) is estimated using a parametric Solidworks model with uniform density. The Simulink model assumes the rotor is cylindrical solid with $J_r = \frac{1}{2} n_b m_b R_{max}^2$. Constants m_b, R_{max} are according to blade geometry as per Table 4.2 (P38) with n_b representing the number of blades per rotor – Data for rotor propeties also shown in Appendix I

5.2. Axis Coordinate Transformations & Linear States

As is illustrated in Figure 5.8 (A – D), from angular displacements in the body axis (§5.1.3), acceleration (B), velocity (C), and displacement (D) states are calculated relative to the world reference axis.

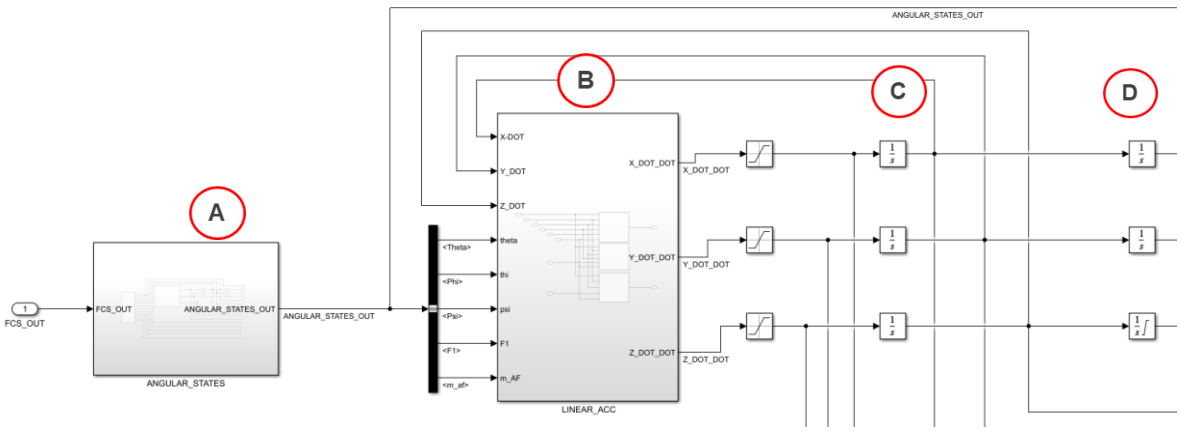

Figure 5.8: Simulink Linear State Model

As previously stated in §2 (P26), rotational Euler angles $[R_\varphi \quad R_\theta \quad R_\phi]^T$ are applied to $[\ddot{X}_b \quad \ddot{Y}_b \quad \ddot{Z}_b]^T$ so that accelerations are converted from the BCS → WCS reference frame according to the vectorized form of Eq. 5.27. [51]

$$\begin{bmatrix} \ddot{X} \\ \ddot{Y} \\ \ddot{Z} \end{bmatrix} = \begin{bmatrix} 0 \\ 0 \\ g \end{bmatrix} - \frac{1}{m} \begin{bmatrix} C_\varphi S_\theta & S_\varphi C_\phi + C_\varphi S_\theta S_\phi & S_\varphi S_\phi - C_\varphi S_\theta S_\phi \\ -S_\varphi C_\theta & C_\varphi C_\phi - S_\varphi S_\theta S_\phi & C_\varphi S_\phi + S_\theta S_\varphi C_\varphi \\ S_\theta & -S_\varphi C_\theta & C_\theta C_\phi \end{bmatrix} \begin{bmatrix} 0 \\ 0 \\ F_1 \end{bmatrix} - \frac{1}{m} \begin{bmatrix} A_x & 0 & 0 \\ 0 & A_y & 0 \\ 0 & 0 & A_z \end{bmatrix} \begin{bmatrix} \dot{X} \\ \dot{Y} \\ \dot{Z} \end{bmatrix} \quad 5.24$$

Using linearized equations from Table 5.5, the Simulink model (Figure 5.8, B) calculates acceleration (Eq. 5.25, 5.28, 5.31) for given inputs ($\phi_b, \theta_b, \varphi_b, F_1, m_{af}, \dot{X}_b \dot{Y}_b, \dot{Z}_b$). After integration, velocity (Eq. 5.26, 5.29, 5.32) and displacement (Eq. 5.27, 5.29, 5.33) states are then output to FCS. [51]

Table 5.5: Linearized Equations of Linear Motion

Des.	Axis	Unit	Equations of Motion	
X Acc.		m/s^2	$\ddot{X}_b = \frac{R_\phi U_1 - A_x \dot{X}_b}{m_{af}}$	5.25
X Vel.	X_b	m/s	$\dot{X}_b = \int \ddot{X}_b$	5.26
X Dis.		m	$X_b = \int \dot{X}_b$	5.27
Y Acc.		m/s^2	$\ddot{Y}_b = \frac{R_\theta U_1 - A_y \dot{Y}_b}{m_{af}}$	5.28
Y Vel.	Y_b	m/s	$\dot{Y}_b = \int \ddot{Y}_b$	5.29
Y Dis.		m	$Y_b = \int \dot{Y}_b$	5.30
Z Acc.		m/s^2	$\ddot{Z}_b = \frac{m_{af} g - R_\varphi U_1 - A_z \dot{Z}_b}{m_{af}}$	5.31
Z Vel.	Z_b	m/s	$\dot{Z}_b = \int \ddot{Z}_b$	5.32
Z Dis.		m	$Z_b = \int \dot{Z}_b$	5.33

Notes With Regards To Linear States And Constants

- Because simulated speeds are low, body drag is not observed to have significant effects on comparisons later discussed, thus coefficients are normalized to $A_{x,y,z} = 0.001$ and assumed constant.

5.3. Flight Control System (FCS)

In basic terms, the flight control system (FCS) is responsible for maintaining stability and controlling the flight direction by adjusting the speed of the individual rotors based on input from various sensors (like gyroscopes, accelerometers, etc.) and the commands from the pilot or autopilot system. To enhance stability and responsiveness when operating in various flight

conditions, PID are often incorporated. In advanced quadrotors, control systems are also able to automate tasks such as altitude hold, GPS position hold, and return-to-home functions.

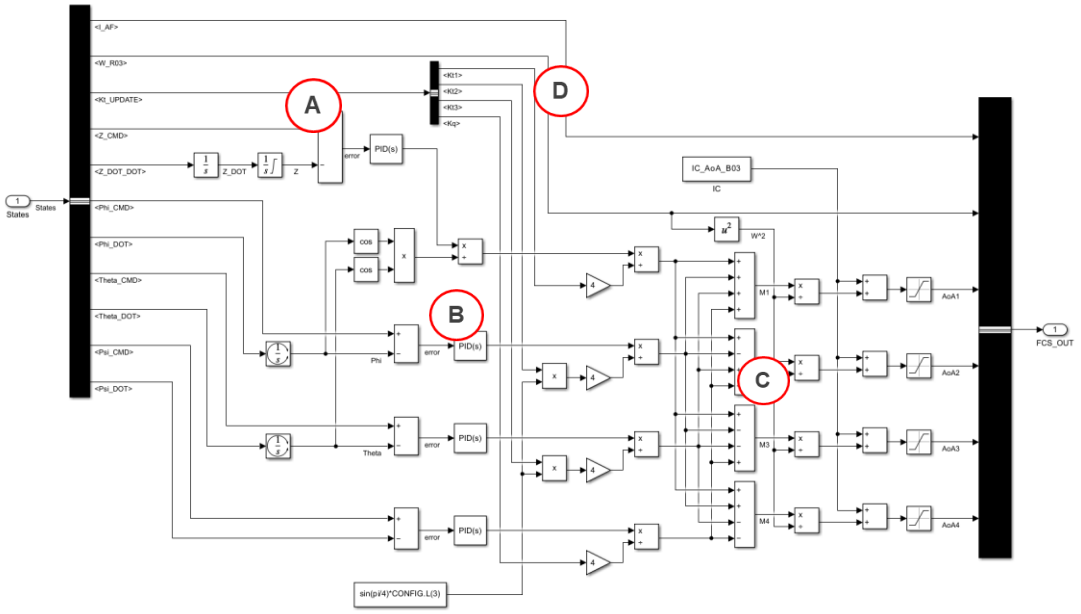

Figure 5.9: Simulink Flight Controller

The command (CMD) input scheme is dependent on the control functionality desired the control system. In this work CMD inputs are designed to emulate a manually controlled transmitter (Figure 5.10) which is similarly used that used for most quadrotors today.

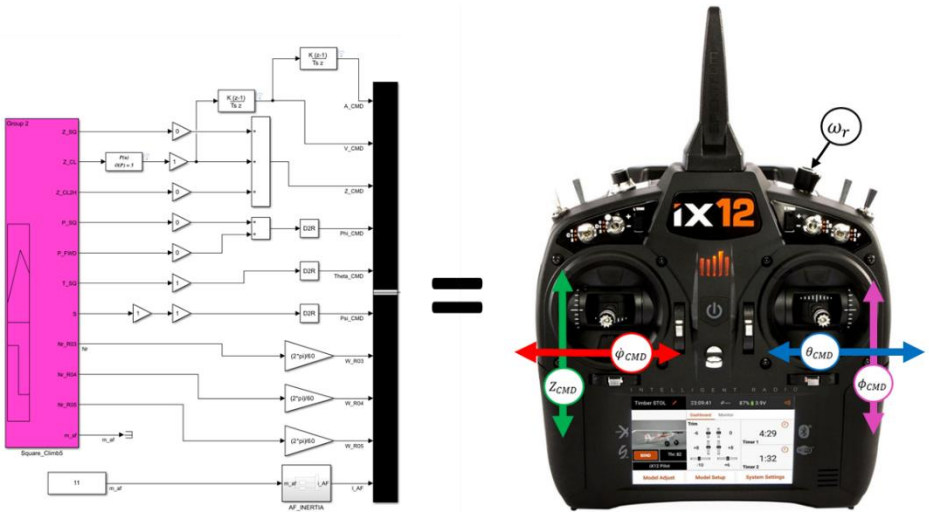

Figure 5.10: Simulink Trajectory Generation [68]

Attitude control (Roll, Pitch and Yaw) thus remains identical to conventional 6-DOF quadrotor, while altitude (Climb/Collective) control is representative to a helicopter which uses a variable pitch rotor at constant head speed.

To Aid In Simplifying The Explanations Following Below;

- Error states output from PID's $\phi_{err}, \theta_{err}, \varphi_{err}, Z_{err}$ are denoted by "err",
- Body states $\dot{\phi}_b, \dot{\theta}_b, \varphi_b, Z_b$ denoted "b" refer to body states output from PLANT outlined in §5.1 – 5.2,
- Command states $\phi_{cmd}, \theta_{cmd}, \varphi_{cmd}, Z_{cmd}$ denoted by "cmd" refer to commanded (CMD) input states.

5.3.1. PID Control

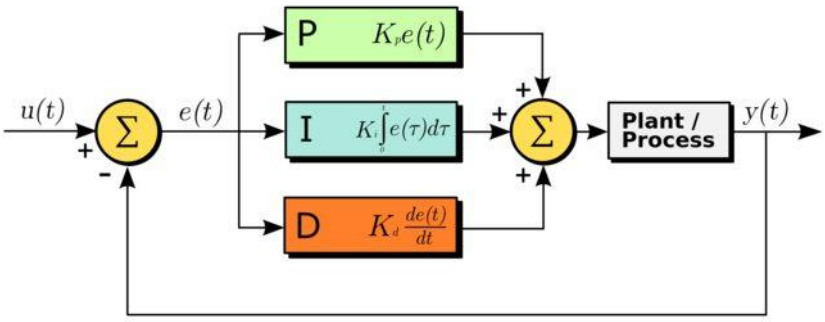

Figure 5.11: PID Controller Illustration [69]

A PID (Proportional, Integral, Derivative) controllers is a control loop feedback mechanism that calculates the difference between a desired setpoint and input, and then attempts to minimize the error by adjusting the process control inputs. The net effect is to enhance stability in dynamic systems with high frequency. In reference to Figure 5.11,

- Proportional term $P = K_P e(t)$ determines the reaction to the current error by producing an output value that is proportional to the current error value.
- Integral term $I = K_I \int_0^1 e(\tau)\, d\tau$ finds the reaction based on the sum of recent errors and is proportional to both the magnitude of the error and the duration of the error.
- Derivative term $D = K_D \frac{de(t)}{dt}$ calculates the reaction to the rate at which the error has been changing and is proportional to the rate of change of the error.

The sum of these three actions (PID) is used to stabilize roll, pitch, yaw and climb states $\phi_b, \theta_b, \dot{\varphi}_b, Z_b$ reflecting the command input scheme mentioned earlier.

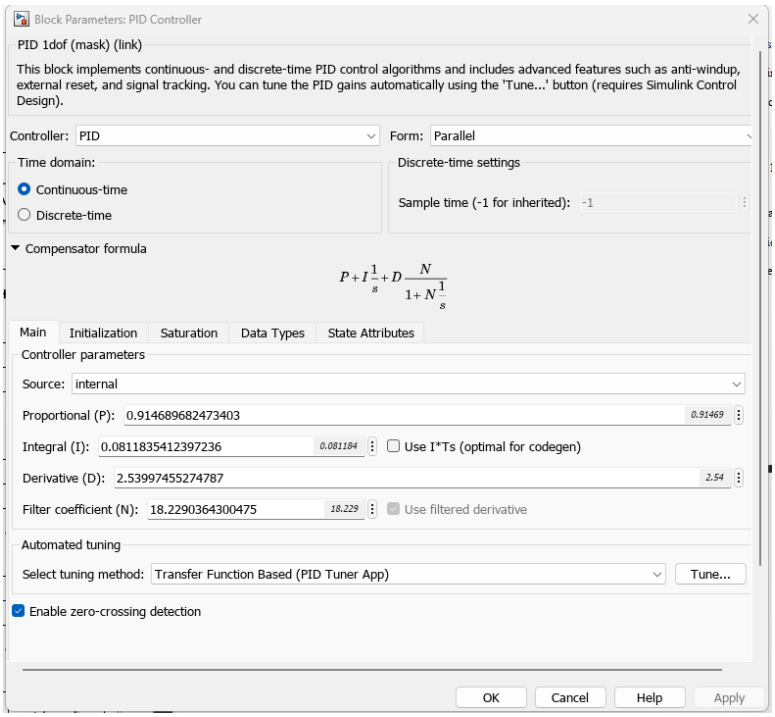

Figure 5.12: Simulink PID Control Block [70]

Shown in Figure 5.12, the Simulink the PID function used is in the form $y(t) = \sum P + I\frac{1}{s} + \frac{DN}{1} + \frac{N}{s}$. The filter coefficient N is associated with the derivative term and is used to filter out high-frequency noise that can cause the derivative term to react excessively, leading to instability in the control system. Filter coefficients and PID gains (K_P, K_I, K_D, N) are obtained using Simulink's built in PID tuner.

5.3.2. FCS Output States

Previously shown in Table 5.1 (P59) fixed pitch control systems based on previous works [50] the desired output from FCS is ω_{r_i}. However, in this work, the desired output is θ_{r_i}. In reference to Figure 5.9 from A – C, the respectively process follows as;

1. Using integration blocks states $[\phi_b, \theta_b, Z_b]$ are obtained given inputs $[\dot{\phi}_b, \dot{\theta}_b, \ddot{Z}_b]$
2. Errors $[\phi_{err}, \theta_{err}, \varphi_{err}, Z_{err}]$ output from PID controllers are then calculated subtracting $[\phi_b, \theta_b, \varphi_b, Z_b]$ from $[\phi_{cmd}, \theta_{cmd}, \varphi_{cmd}]$,
3. Pitch angles $\theta_{r_{1-r_4}}$ can then be calculated by rearranging Eq. 5.3, 5.7 – 5.9.

Notes With Regards To PID Controllers And States

- Thrust and torque coefficients ($k_{r_1 \to r_3}, q_{r_1 \to r_3}$) are obtained from KT-UPDATE (Figure 5.9, D) which is identical to the model shown in §5.1.2, P60. Due to limited time,

alternative methods to update coefficient states directly from plant could not be found as explained in §8.3, P85. The addition of this stability method does not change the nature of the underlying physics components, given that the FCS deployed in a real world.

- Pitch angles $\theta_{r_{1-r_4}}$ are constrained by $\lim_{x \to 13^o} \theta_{r_i}(x)$ to ensure PID controllers are unable to drive FCS outputs beyond the data range of lookup tables C_l, C_d (§5.1.2).
- PID controller gains were tuned individually for each rotor variant with mass set to $\boldsymbol{m_{GTW}} = 9kg$ with the reference signal and time period according to the trajectory outlined in §6.2.1, P71.
- The Simulink PID auto-tuner application was set to optimize for a "balanced response" and adjusted so that the overshoot remained within 15-20% as is illustrated in Appendix K.

6. EVALUATION AND IMPLEMENTATION

Aircraft development is a complex, iterative process focused at targeting specific goals or capabilities which are contingent upon maximising both endurance and efficiency. Endurance pertains to an aircraft's ability to sustain flight for long durations and is dependent on factors such as fuel capacity and aerodynamics. Efficiency relates to fuel consumption and operational aspects like payload capacity and speed.

6.1. Evaluation Framework & Scope

Performance can be defined in multiple ways and is subject to ambiguity. As mentioned before, the quadrotor model developed in this work offers resolution and complexity sufficient for early-stage development. From this perspective, the evaluation in this section will primarily focus on the scaling of rotor geometry and payload capacity in relation to efficiency and endurance. The aim is to gain insights into how these factors influence flight behaviour.

6.1.1. Performance Criteria Identification

To understand the selection of performance criteria discussed later in this section, it must be understood how rotor geometry and payload capacity are related as well as their effect on efficiency and flight behaviour.

- **Rotor Geometry:** More efficient rotor designs can generate the same lift with less power. For example, high aspect ratio blades can produce more lift, but require more power. The key is to find a balance that provides the necessary lift with the least power consumption. These statements are reflected in comparisons between theory (§3, P31) and experiments (§4.5, P53) , where it was shown that the shape, size, and pitch of the rotor blades significantly affect power consumption.
- **Payload Capacity:** From theory [14] it is shown a higher payload demands more power to counteract gravity and to maintain control authority required to perform manoeuvres (§3, P31). However, increasing payload capacity affects rotor solidity, (size and speed) leading to higher power consumption. An efficient design thus aims to maximize payload capacity without a significant increase in power demand.

6.1.2. Evaluation Aims & Analysis Scope

With an understanding of the interdependence of the variables outlined above, the evaluation framework is formulated to answer the following main questions.

4. Which rotor configuration provides the highest acceleration and vertical climb speed for the least power consumption?
5. How does payload capacity affect power demands and efficiency?
6. How does the control system and airframe response and behaviour change during flight?

6.2. Evaluation Methodology

Given the evaluation scope outlined earlier, methodology is formulated as follows.

- A single climb-to height (C2H) trajectory will be used to subject the quadrotor airframe to maximum accelerations and velocities and power demands.
- Three rotor geometry variants (§4.5, P53) will be evaluated according to two payload ($m_b = 9.0 \rightarrow 10kg$) scenarios respectively,
- Rotor speed will be constrained to $N_r = 2500\,rpm$ to matching tested speeds and to emulating the highest possible power demand condition.

It will be reminded that the BEMT rotor model (§4.4, P52) incorporated geometry from tested rotor blades (Table 4.2, P38) to ensure simulation performance was consistent with data obtained with rotor experimentation.

6.2.1. Flight Trajectory Generation

In the machine control field, ramp functions are frequently employed for situations here repeatability or point-to-point precision is affected by inertia under high accelerations. While numerous methods exist, the 5th Order Polynomial-Curve (Eq. 6.1) is selected for its simplicity and flexibility to modify trajectory for states.

$$H_b = s(t) = a_0 t + a_1 t^2 + a_2 t^3 + a_3 t^4 + a_4 t^5 \; where \; t = 5.0s \qquad 6.1$$

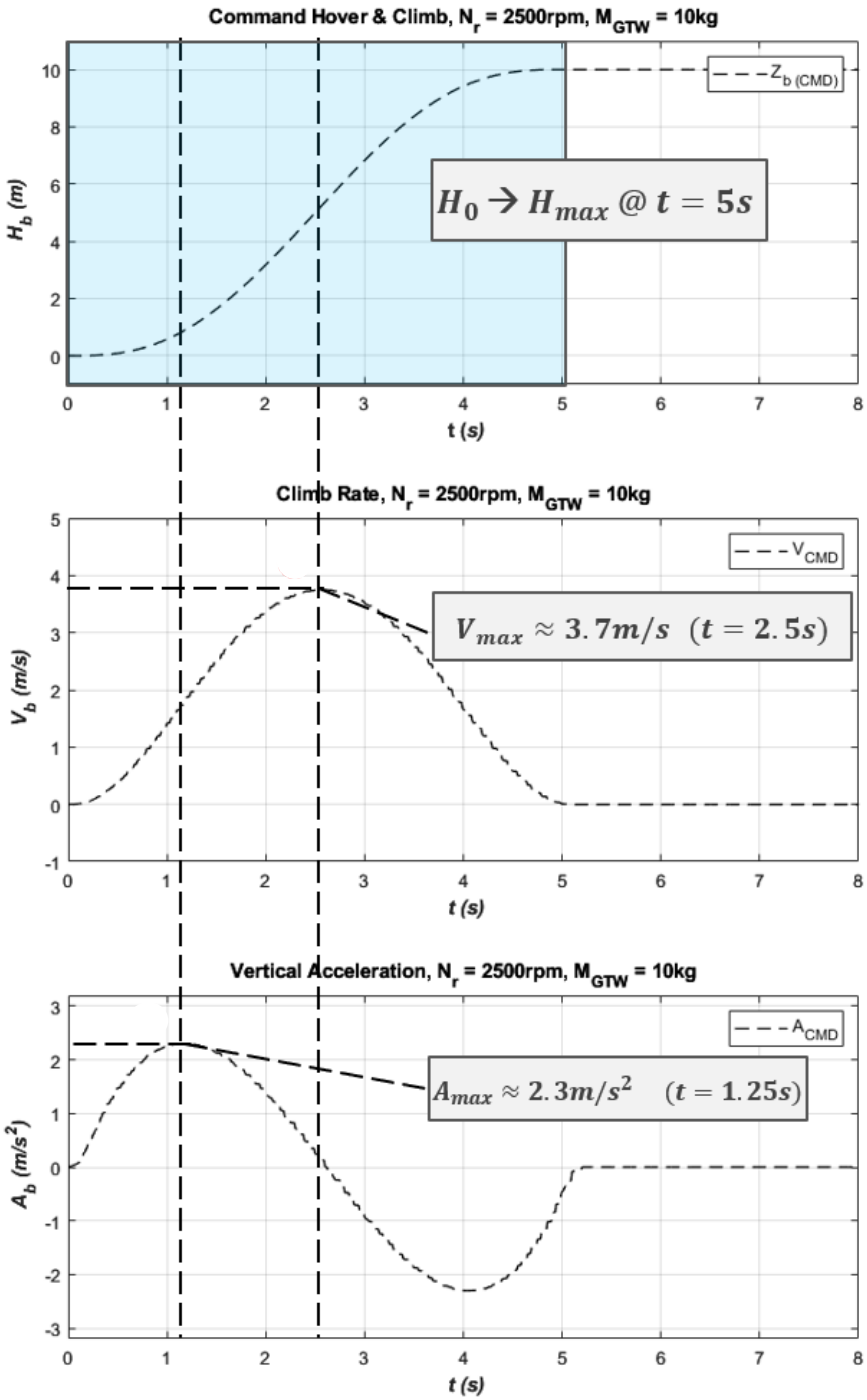

Figure 6.1: Simulated Climb Trajectory

In this work, the quadrotor body will be expected to climb to $H_b = 0.0 \rightarrow 10.0m \; for \; t_{sim} = 5.0s$. Curves are generated by first solving for a_{0-4} and then integrating to obtain velocity $\dot{s}(t)$ and acceleration $\ddot{s}(t)$. Boundary conditions are defined from $[s(0) = 0; s(t) = 10m; \dot{s}(0) = 0; \dot{s}(t) = 0; \ddot{s}(0) = 0; \ddot{s}(t) = 0]$. The body will be projected to reach $V_{max} = 3.7m/s$ and $A_{max} = 2.3m/s^2$ as shown in Figure 6.1.

It is important to emphasize that the control system in this work is designed to match commanded trajectories $[\phi_{cmd}, \theta_{cmd}, \varphi_{cmd}]$, accelerations and velocities observed are considered as raw output figures relative to idealized curves.

6.2.2. Boundary Conditions, Simulink Settings & Nomenclature

Flight Condition and Atmosphere: At $t_{sim} = 0.0$, the quadrotor is hovering at sea level ($H_b = 0.0m$) where ground affect is not considered. Rotor speed, relative air speed, airframe mass and air density $N_r, v_{rel}, m_b, \rho_{ISASL} \rightarrow const$. The airframe mass density, $\rho_b = uniform$ for estimation of mass inertia from §5.2, P59.

Stability Enhancement: To stabilize the simulation, $\theta_{r_{1-r_4}} = 6.9^o \; when \; t_{sim} = 0.0s$ which sets initial rotor coefficients in KT-UPDATE for the first increment of $t_{sim} = 0.01s$.

Simulink Settings And Sample Rate: Default solver mode is used**.** One minute of simulation t_{sim} is normalised to $t_{sim} = 60/i_{sim}$ so the sample rate is $i_{sim} = 0.01s$.

Variable Connotations:

- The definition for altitude can be considered $H_b = Z_{poly}$.
- Velocity $V_{max} = \dot{Z}_{poly}$ and acceleration terms $A_{max} = \ddot{Z}_{poly}$ are assumed ideal and denoted as "*poly*" to infer values originate from Eq. 6.1.
- Payload or body mass refers to gross take-off weight (GTW) will be considered $m_b = m_{GTW}$.

Rotor & Payload Configurations: For ease in explanation simulated quadrotor variants will be identified by "Bxx_{Tn}" in reference specifications listed from Table 4.2, P38. References specific to the payload scenario tested are denoted by the subscript "Tn" shown in Table 6.1.

6.3. Simulation Results

As mentioned before, two payload scenarios were simulated in Simulink where dynamic, thrust and power performance results are summarized in Table 6.1. For conciseness, figures shown in this section (Figure 6.2, Figure 6.3, Figure 6.5) considers $m_{GTW} = 9$kg, results for $m_{GTW} = 10$kg is shown in Appendix F – H.

Table 6.1: Summarized Simulation Results

Test (Tn)	m_{GTW} (kg)	$Rot.Var.$	V_{max} (m/s)	A_{max} (m/s^2)	T_{max} (N)	P_{max} (kW)
T1	9	B03	3.99	2.41	112.07	1.21
		B04	4.14	2.63	114.34	1.09
		B05	4.01	2.47	112.7	1.15
T2	10	B03	3.8	2.5	125	1.7
		B04	4.3	2.85	129	1.26
		B05	4.1	2.65	126	1.3

**Note: Performance is indicated from best to worst respectively as Green, Blue, and Red.

6.3.1. Dynamic Performance

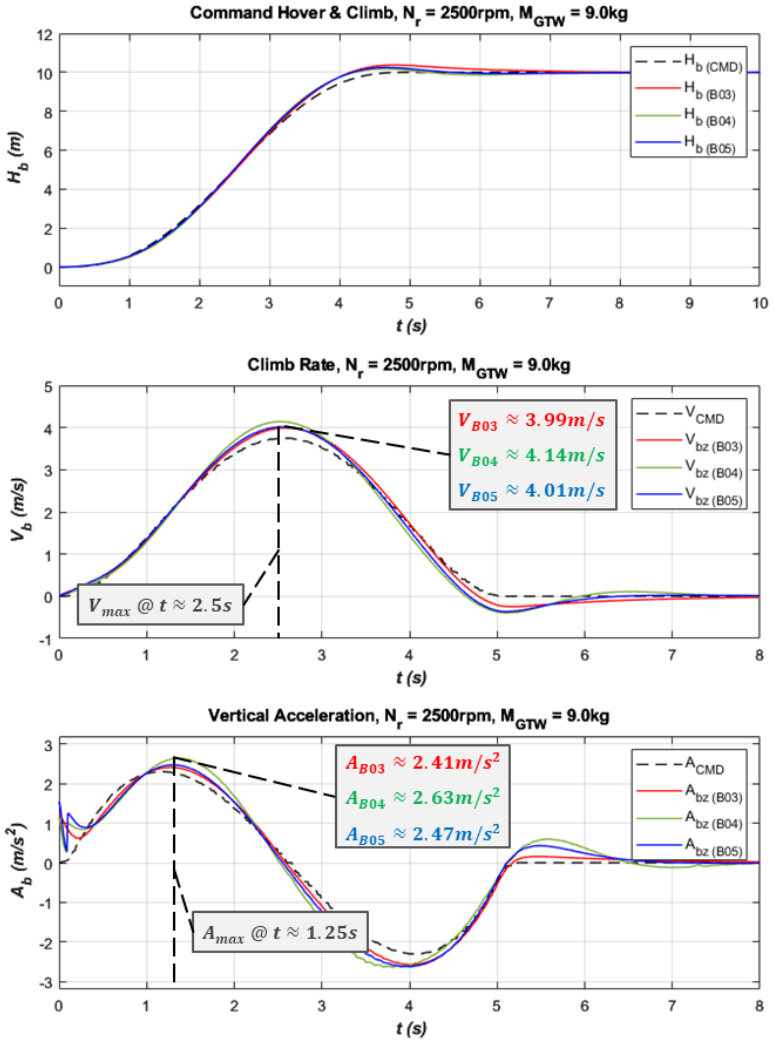

Figure 6.2: Dynamic Performance, Test Scenario 1

From Figure 6.2 and Figure 8.4 (Appendix F), the control system maintained robust performance when subjected to varying payloads and rotor geometries since no significant

trajectory overshoot was observed. In terms of climb rates, $V_{\mathrm{B04}} > V_{\mathrm{B03}}, V_{\mathrm{B05}}$ (Table 6.1) for both payload scenarios which was interesting since B05 has the largest solidity envelope (Eq. 3.9).

Furthermore, it's evident that B03 is operating close to its payload threshold since climb rate and acceleration correlations relative to B05 at $t_{sim} \approx 1.25s$ diverged further at higher payloads ($m_{GTW} = 10kg$). Furthermore, $\mathrm{B03_{T2}}$ was observed to overshoot $H_b = 10$, (Figure 8.5, App. F) showing that the control system was unable reduce acceleration in time ($t_{sim} \approx 4.5 \rightarrow 5s$). These examples clearly demonstrate how payloads and rotor geometry influence dynamic behaviour and control authority.

6.3.2. Thrust Performance

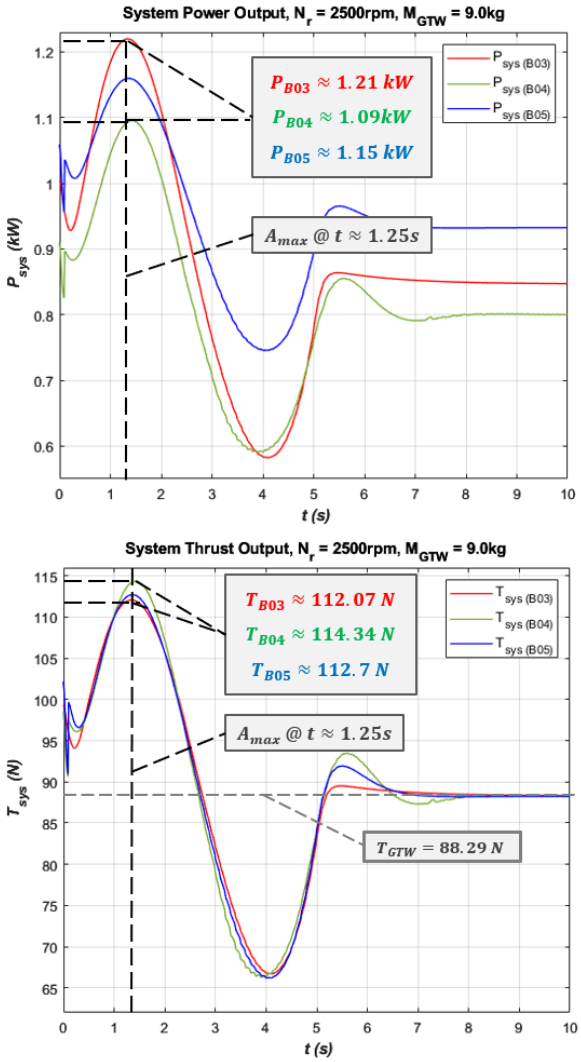

Figure 6.3: Thrust And Power Output, T1

In terms of thrust performance, its shown that $T_{\mathrm{B03}} < T_{\mathrm{B04}} > T_{\mathrm{B05}}$ in both payload scenarios during peak accelerations when $t_{sim} \approx 1.25s$. (Figure 6.3, Figure 8.5 – App. G) Variant B04 was also able to maintain higher thrust output over time yielding superior climb rates and accelerations as noted in findings mentioned earlier in this section.

Notably during peak acceleration is shown that $T_{B03} \approx 112.07N$ which is close to the theoretical maximum of $T_{B03_{max}} \approx 112{,}815kg$ ($\theta_{\mathrm{r_{B03}}} = 13^{o}$) which explains the diminished dynamic responses outlined earlier. In this case, the thrust capacity of B03 is considered as saturated and unable to respond to additional FCS authority if commanded.

As previously emphasized, the thrust output is directly proportional to the power required to induce acceleration. The larger the magnitude of acceleration, the more work is done to move air, which increases power demands. Simultaneously, payload configurations selected in this evaluation were intended to highlight performance aspects and limitations – as in the case for B03 above – between rotor variants are highly contingent upon the intended use case.

6.3.3. Power Consumption & Efficiency

The energy supply to the power system, being finite, has a significant influence on payload capacity and flight endurance, making efficient power use a critical consideration during early-stage design which is the main motivation this work aims to investigate. The efficiency conundrum is further complicated by the fact that rotorcraft must be optimized for low speed and hovering conditions which consumes significantly more power [14, 26] as the Figure 6.4 for a conventional helicopter system shows.

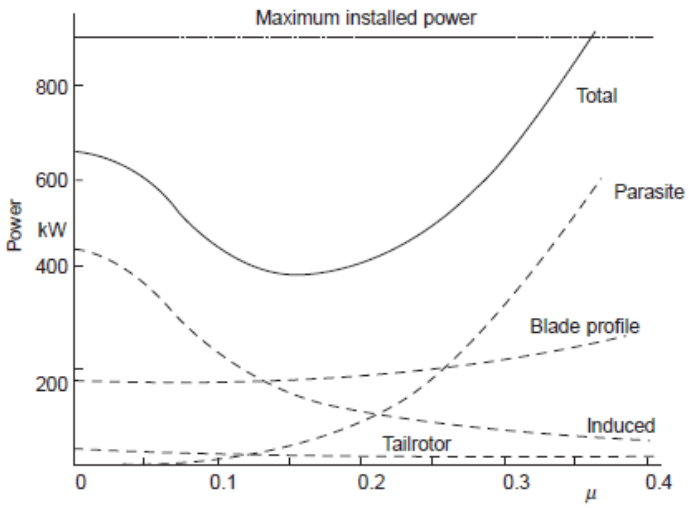

Figure 6.4: Variation of rotor power demand to forward flight speed [14]

Before outlining observations below, it is important to remember that the BEMT rotor model used in this work (§5.3, P65) emulates a rotor in a hovering condition as this is considered the worst-case scenario and is used to establish maximum power demands [14]. In dynamic manoeuvres, the increase in relative airspeeds lowers the effort required to move air, which leads to a decrease in power demands. In this work power comparisons for climb scenarios are merely used to demonstrate variances in static and dynamic flight profiles.

From Eq. 3.7, it is established that thrust is directly proportional to the power required to induce acceleration. A greater magnitude of acceleration necessitates more work to move air, thereby increasing power demands. This relationship is clearly demonstrated in Figure 6.3 and Appendix G, particularly during peak acceleration ($t_{sim} \approx 1.25s$) where it can be seen that $P_{\mathrm{B03}} > P_{\mathrm{B04}} < P_{\mathrm{B05}}$. This observation for P_{B04} is also seen at hover condition at $t_{sim} \approx 8 \rightarrow 10s$.

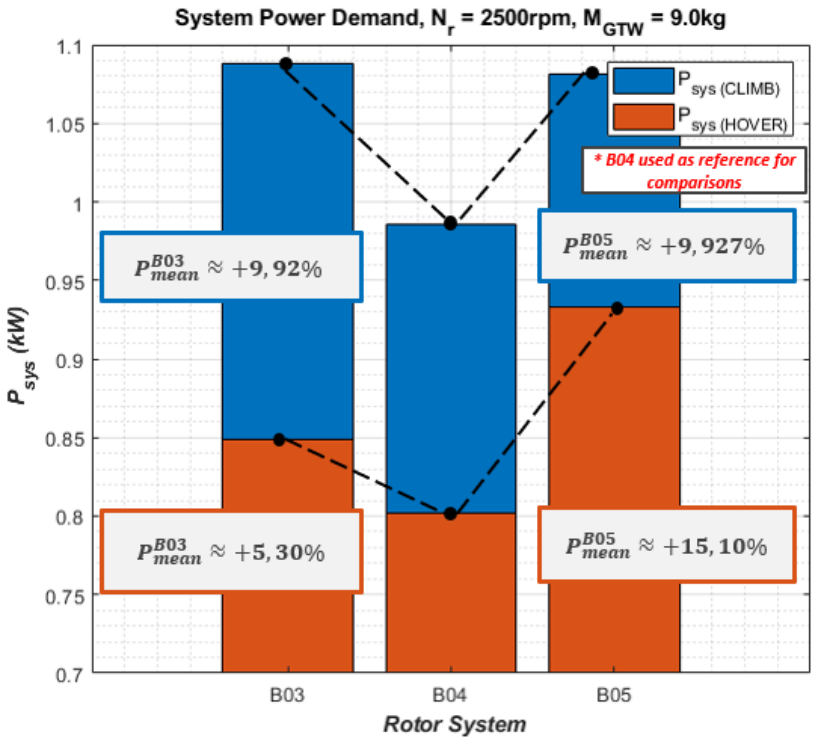

Figure 6.5: Power Output Comparison, T1

Using B04 as reference, the contrast in power efficiency can be highlighted by comparing mean power consumed during both flight phases as shown in Figure 6.5. Mean power consumption during climb P_{mean}^{climb} was averaged over the period of $t_{sim} \approx 0 \rightarrow 8s$ whereas P_{mean}^{hover} is considered from $t_{sim} \approx 8 \rightarrow 10s$. When $m_{GTW} = 9\text{kg}$, B04_{T1} consumed the least amount of power, outperforming B03_{T1} and B05_{T1} by 5 – 9% during climb and 12 – 15%. During hover these differences also increased further for $m_{GTW} = 10\text{kg}$ as can be seen in Appendix H.

Rotor efficiency is generally expressed as a *"figure of merit"* which is the ratio of induced power to the total power ($\bar{M} = Tv_i/P$), but this value does not consider numerous other parameters are involved which also affect comparisons according to Bramwell. [14]

For simplicity, comparisons will be made by normalizing mean power consumption per unit mass so that $\delta_{Bxx} = P_{mean}/m_{gtw}$ as shown in Figure 6.6. Applying this method, it can be seen that $\delta_{B04} \approx 2 - 3\%$ increase at higher payloads while consuming the least amount of power per unit mass relative to δ_{B03} and δ_{B05}. In contrast to δ_{B05} also shows little increase compared to δ_{B04} indicating that B05 is operating below is optimal power efficiency range at this payload capacity.

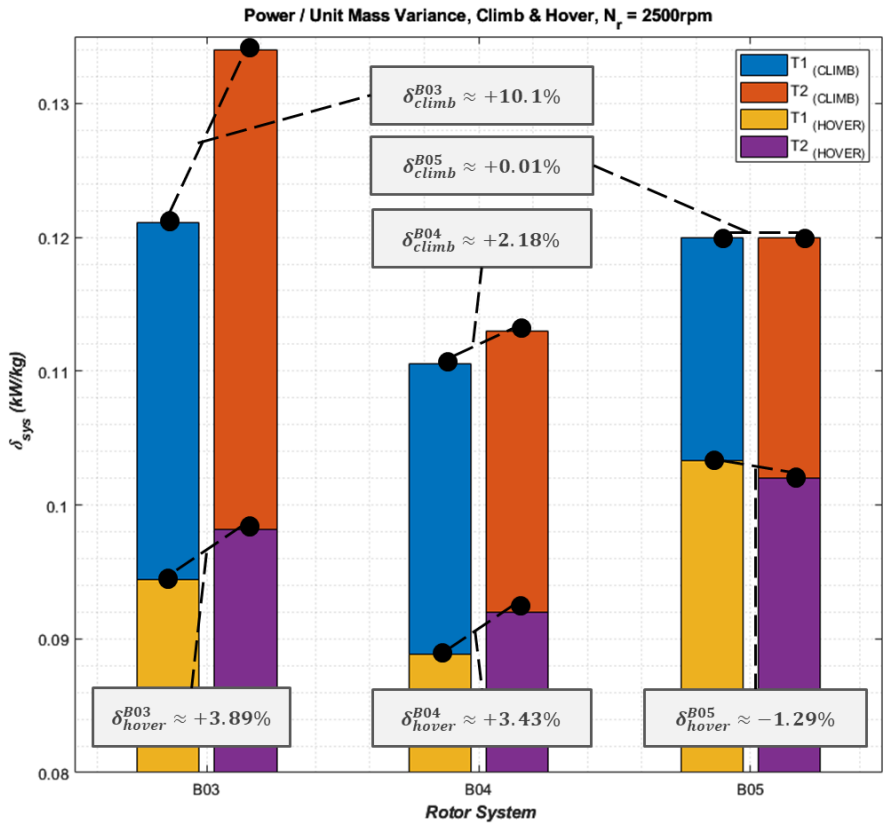

Figure 6.6: Power Per Unit Mass Comparison for Climb & Hover

As an example to emphasize the importance of power efficiency between payloads – using the quadrotor is hover state where $m_{GTW} = 10\text{kg}$ and the maximum power demand is assumed to be $P_{T2max}^{B0i} = P_{T2mean}^{B0i}$ over a period of $t = 60min$ – B03 is projected to consume $P_{T2max}^{B03} \approx 5.88\ kWh/kg$ compared to B04 with $P_{T2}^{B04} \approx 5.52\ kWh/kg$.

7. DISCUSSION

The output of this work has realized a functional model which enables the development of key insights into the adaptability of a control system given various scales and payloads.

As demonstrated in earlier sections (§6.3on page 73 P76), Empirical validation and simulation conducted in this work not only showed control system adaptability at various scales, but also illuminated the critical importance of rotor geometry and payload capacity selection, and that efficiency has a significant influence on endurance and flight behaviour in rotorcraft. Collected data and results (§6.3, P73) are used to abstract simple examples for the purposes of briefly discussing additional points following below which are relevant to quadrotor applications and control system design.

- Considerations for power system selection,
- Mission profile selection based on rotor geometry & efficiency limitations,
- Effects of PID response tuning,

7.1. Power System Selection

For aircraft in general the Gross Take-off Weight (GTW) consists of a fixed mass for the airframe, including avionics and hardware, and a variable mass for cargo and fuel. Given that fixed masses remain constant, an airframe optimized for high-endurance applications seeks to minimize energy losses from drag and drivetrain inefficiencies while maximizing the energy density of onboard fuel or power sources.

In fuel-powered platforms, fuel consumption reduces mass over time thereby decreasing the workload on the propulsion systems to maintain altitude and consequently improving endurance. This benefit is further amplified at higher altitudes, where air resistance is lower. In contrast, battery-powered platforms maintain their mass while experiencing a reduction in energy density as the charge depletes. To match the endurance of a comparable fuel-based system, a significant increase in mass is required, which in turn reduces the available cargo capacity. This concept will be further illustrated through a simple example below.

To understand how aforementioned efficiency factors for endurance and payload capacity are related, let’s consider quadrotor (based on parameters from, P74) with a drivetrain powered by a LiPo battery and carbon fuel.

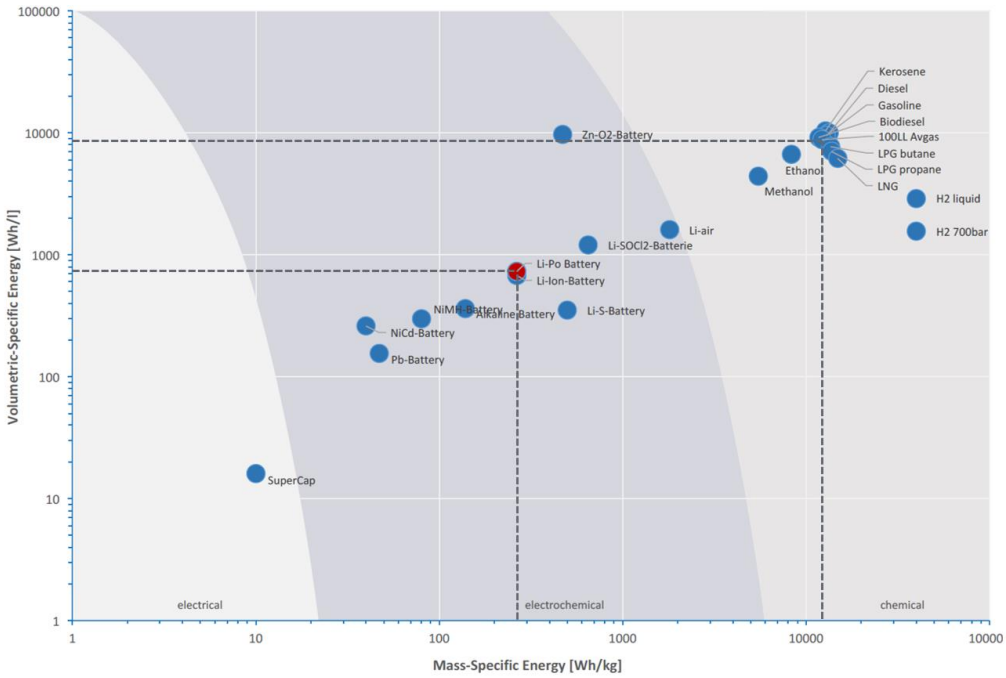

Figure 7.1: Energy Density battery chemistries and carbon fuels [5]

From §6.3.3 (P76), the quadrotor with $m_{GTW} = 10kg$ and requires $P_{T2mean}^{B03} \approx 0.98\,kW$ to maintain a stable hover condition. Assuming the mass of energy stored onboard is constant and constrained to $m_E = 5kg$, energy density G_x (Figure 6.4) and system efficiencies $n_{x_{sys}}$ for LiPo and fuel powered systems as the following;

- $G_{LiPo} \approx 0.200\,kWh/kg$ with $n_{LiPo\_sys} \approx 85\%$,
- $G_{fuel} \approx 12000\,kWh/kg$ with $n_{fuel\_sys} \approx 15\%$.

Hover time of a system LiPo battery will be approximated to reach an endurance of $t_{LiPo\_hover} \approx 52min$ whereas the fuel driven system $t_{fuel\_hover} \approx 551min$. Repeating the same scenario for B04 where $P_{T2mean}^{B04} \approx 0.90\,kW$, $t_{LiPo\_hover} \approx 56min$ with $t_{fuel\_hover} \approx 600min$. While this basic example considers highly ideal energy use for both cases, it does emphasise that efficiency is a fundamentally important performance indicator to consider when optimizing rotor geometry as its effect on endurance capability will constrain selection of mission profiles and payload capacity.

7.2. Geometry Considerations and Application Scope

From the example in §7.1 its evident that powertrain selection also contributes to affecting balance between payload capabilities and endurance limitations. This abstraction is formulated on the basis that experiments (§4, P35) and simulations (§6.3, P73) show how varying scales

rotor geometry (Table 4.2, P38) and payloads are interconnected, and that their combined effects yield varied flight behaviours. This outcome is favourable as it can be used as a basic framework which can be used to identify and develop basic mission profiles purely based on selection of hardware – As an example focusing on rotor variants tested in this work.

- Variant B04: Considered optimal for applications with moderately flexible payload configurations but prioritises higher endurances given this variant superior efficiency and dynamic performance in both payload classes.
- Variant B05: Recommended for applications requiring higher payload variability, with emphasis on prioritizing control authority, responsiveness and physical robustness over efficiency or cost savings.
- Variant B03: This variant is suboptimal in both payload classes in terms of dynamic behaviour, responsiveness, and efficiency but is expected provide better efficiency than larger rotor variants for applications requiring shorter endurances with smaller payloads.

7.3. PID Control Response Vs Acceleration

The "responsiveness" of a PID system is directly proportional response times to external disturbances. In simple terms, less responsive systems (underdamped/ under-tuned) lead to sluggish accelerations which compromises agility and responsiveness to pilot inputs. Conversely, highly responsive systems (overdamped / over-tuned) will enable more abrupt accelerations but can lead to excessive trajectory overshoot and oscillations.

In the case of this work, from Figure 6.2P (P74) when the simulation is initiated at $t_{sim} \approx 0 \rightarrow 2s$, the PID system attempts to stabilize the quadrotor resulting in an acceleration fluctuation of $A_{B05} \approx 0.5 \rightarrow 1.2 m/s^2$ within $t_{sim} \approx 0.2s$ and a power demand spike of $P_{B05} \approx 0.19$W. For quadrotors with higher mass inertia scenarios - abrupt accelerations will not only destabilize flight but also lead to excessive stress on drivetrain components and airframe fatigue from forces and torques. It is thus important to consider that fine-tuning PID controller responsiveness is not only crucial for achieving optimal accelerations which will mitigate component wear, improve flight performance, and enhance power usage efficiency.

8. CONCLUSION

Efficiency and endurance challenges in quadrotor platforms can be mainly attributed to payload constraints, which are directly related to the energy density of current battery-based power sources. The integration of variable-pitch rotor systems combined with fuel-based power delivery systems shows promise in overcoming challenges also similarly echoed in related works (§1.2, P19). Moreover, the scalability of control systems is pivotal for optimizing performance across different mission profiles and enhancing operational flexibility by allowing effective management of rotor geometry and payload capacity, while facilitating the integration of alternative power delivery methods. Empirical validation coupled with simulation has proven vital to illuminate how these collective factors dictate mission profiles and performance characteristics of quadrotor platforms, and how endurance and efficiency are critically dependent on choices related to rotor geometry, payload capacity.

8.1. Empirical Validation of Models and Simulations

The aerodynamic complexities of the variable-pitch systems integrated into the quadrotor's Flight Control System (FCS) are a notable aspect of this investigation. Since this work is mainly intended for practical utility – empirical assessments and simulations were key (§6, P70) to ensure accuracy of the theoretical BEMT rotor model given the scarcity of published data, while revealing that quadrotor flight characteristics are highly sensitive to changes in payload and rotor geometry.

Comparisons (§4.5, P53) suggest that the MATLAB-based BEMT rotor model's theoretical thrust approximations closely aligned with experimental data across a range of speeds and rotor pitch angles. This consistency implies the model's accuracy and dependability in predicting rotor system thrust performance. In contrast - theoretical power consumption estimates from the BEMT rotor model closely follow experimental results within a certain pitch range. However, the BEMT model tends to overestimate power outputs at larger pitch angles ($\theta_i \approx 7^o \rightarrow 13^o$). These conclusions further suggested that the BEMT rotor model demonstrated consistent performance across different scales and offers a high-fidelity emulation of real-world thrust performance but may require adjustments to enhance accuracy of power output predictions at larger pitch angles. Instability issues related to power deviations are further discussed in work published in parallel to this investigation focusing on evaluating the use of XFOIL for variable-pitch rotor systems [1].

It can thus be concluded that the substantial time and financial investments made to perform experiments was the correct choice as it proved vital in validating that the theoretical variable-pitch MATLAB model used in the FCS aligned with real-world performance. The insights gained are outlined in the sections below.

8.2. Rotor Geometry Affects Efficiency.

As mentioned before, this work aimed to investigate the critical role of efficient power use in determining payload capacity and flight endurance, especially during early-stage design. While it was logical to assume that thrust and power demands were expected to increase with rotor sizes tested during experimentation - observations from simulated output (§6.3, P73) suggest that relatively small differences in rotor geometry (Table 4.2, P38) yielded highly contrasting performance profiles and dynamic behaviours. Before discussing conclusions below – it will be noted that the payload boundary conditions for simulated scenarios were designed not only to show how performance scales with geometry but also to illustrate the risks of exceeding payload limitations.

During hover, payload saturation experienced by B03 resulted in considerable power demands attributed to drag produced at high blade pitch angles (Figure 6.3, P75). Accelerations further impacted FCS control authority to maintain the commanded trajectory as B03 was operating close to blade stall, unable to further increase thrust (§6.3.1, P74). Conversely, B04 consistently outperformed other rotor variants in terms of dynamic performance and power demands for both payload scenarios by 5-15% during climb and hover (Figure 6.5 (P78) and Appendix G). This observation was interesting as it demonstrates that disk loading capacity advantage of B05 is less efficient than B04 due to increased power demands imposed by parasitic drag losses and blade mass-inertia (§6.3.3, P76). In practical terms, this means that size does matter, and that efficiency performance does not necessarily scale with rotor size. Further practical implications and benefits of variable pitch rotor geometry on control system architecture are discussed further in the §8.3 below.

Based on these findings, it is evident that the impact of rotor geometry on efficiency is both complex and nuanced. However, this investigation successfully employed a combination of empirical and simulation methods to provide valuable insights. This approach facilitated a quantitative understanding of the interrelationships between rotor geometry and efficiency, thereby offering practical guidance for early-stage design considerations.

8.3. Control System Scalability

In the realm of quadrotor development, control system scalability is a critical factor for ensuring adaptability across various operational scenarios and configurations. This adaptability is particularly important for applications that require rapid reconfiguration or deployment in diverse environments, making control system scalability a key consideration in the design and optimization of quadrotors. Simulation tools such as MATLAB and Simulink were found to be vital software tools which enabled the investigating of all these aspects and illuminating key performance limitations before deployment to a hardware environment.

Performance comparisons from simulated scenarios suggest that the control system architecture combined with variable pitch rotor systems developed in this work offers the capability of seamless integration with different rotor geometries, payload capacities, and power systems, and offers to enhance quadrotor's versatility. In terms of dynamic performance (Figure 6.2, P74, and Appendix F), the control system was shown to maintain stable flight and responsive manoeuvring, from low-speed hovering to high-speed directional changes.

Focusing on the FCS: Given the idealized flight trajectory used (§6.2.1, P71), additional tuning of PID control loops aimed to enhance response stability issues found with B03 (§6.3.1, P74) showed no improvements. In this special case it was concluded that the issue can be relegated to performance limitations of the rotor configuration, rather than the control system itself. This observation further illustrated that Simulink and MATLAB models (§5, P56) emulated real flight behaviour consistently given the possibility that a payload capacity exceeded the thrust performance limitations rotor system.

8.4. Considerations and Opportunities for Future Work

In contrast for fixed pitch control methodology where FCS output states vary thrust in terms of rotor speed such that $\omega_i^2 = f_i/k_i$, the introduction of variable pitch control (§5.1.1, P58) enables FCS output states to modulate thrust magnitudes in terms of rotor pitch angle and speed ($\theta_i = f_i/\omega_i^2 k_i$). Practically this means that during a hovering flight, the control system can be adapted to prioritise for optimal efficiency and reducing power demands by altering both rotor speed and blade pitch angles, while trimming head speed and pitch angles in forward flight to reduce drag while also compensating for altitude. By adopting similar control architecture proposed in this work, quadrotor platforms can further leverage efficiency drag reduction benefits of higher altitudes, as the control system can be adapted trim, in contrast to fixed pitched rotors which

will be required to increase rotor speeds leading to efficiency penalties as shown in Figure 1.4 (P22) [32].

It's important to mention that the FCS architecture developed in this work is subject to further improvements in future work. As noted in §5.3.2 (P68) – when the simulation is initialized at $t_{sim} = 0.0 \rightarrow 0.01s$, initial conditions for pitch angle states output from FCS are $\theta_{\mathrm{r}_{1-\mathrm{r}_4}} = 0$, because torque and thrust coefficients $k_{r_1 \rightarrow r_3}, q_{r_1 \rightarrow r_3} = 0$ thus force vector states calculated in PLANT are $U_{1 \rightarrow 4} = 0.0N$. This means the quadrotor will accelerate along $-Z_B$ when the simulation is initialized, resulting in lagged and overcompensated PID responses to correct the commanded trajectory when the first iteration updates $k_{r_1 \rightarrow r_3}, q_{r_1 \rightarrow r_3} > 0$. The addition of IC constant blocks to set $\theta_{\mathrm{r}_{1-\mathrm{r}_4}} > 0$ (Figure 5.5, P61) in the PLANT model also did not improve stability.

To overcome the sequential calculation method of Simulink, rotor force blocks (identical to ones used in PLANT from Figure 5.5, P61) were added in parallel (grouped under KT-UPDATE) to FCS control block. Here, IC constant blocks set $\theta_{\mathrm{r}_{1-\mathrm{r}_4}} > 0$ when $t_{sim} = 0.0 \rightarrow 0.01s$ to ensure states $k_{r_1 \rightarrow r_3}, q_{r_1 \rightarrow r_3} > 0$. While this stability enhancement method is sensible to ensure simulation stability – it's also inefficient since rotor force vectors calculated in PLANT lags behind KT-UPDATE and could cause drift. Simultaneously, it must further be emphasised that this workaround does not alter physics components which emulate dynamics of the quadrotor in a real-world scenario.

Furthermore, the inclusion of power demand or efficiency optimization functionality in the current control system in its current state would be challenging. XFOIL coefficients for C_l, C_d in lookup tables for BEMT rotor models (Figure 5.5, P61) are based on Reynolds numbers which consider fixed speeds and altitudes. Future development efforts could focus on developing a non-linear function or system using advanced computational methods such as machine learning as a means to dynamically updating these values.

REFERENCES

[1] B. Nielsen and M. Gilpin, "XFOIL Performance Validation for Medium-Scale Variable Pitch UAV Rotor Systems," *R & D Journal of the South African Institution of Mechanical Engineering,* 2023, doi: http://dx.doi.org/10.17159/2309-8988/2019/v35aX.

[2] K. Mars. "115 Years Ago: Wright Brothers Make History at Kitty Hawk." https://www.nasa.gov/feature/115-years-ago-wright-brothers-make-history-at-kitty-hawk (accessed 2018-03-05.

[3] L. Wood. "Commercial Drones Market: Global Industry Trends, Share, Size, Growth, Opportunity and Forecast 2022-2027." Yahoo Finance. https://www.researchandmarkets.com/reports/5642337/commercial-drones-market-global-industry-trends (accessed 2022-09-18.

[4] S. UELAND. "Drone Delivery Companies." Practical Commerce https://www.practicalecommerce.com/8-commercial-drone-delivery-companies (accessed 2022-09-18.

[5] DRONEII. "Drone Energy Sources – Pushing the Boundaries of Electric Flight." DRONEII.com. https://www.droneii.com/drone-energy-sources (accessed 2018-06-26).

[6] L. R. Jenkinson, J. Marchman, and J. F. Marchman, *Aircraft Design Projects: For Engineering Students*. Butterworth-Heinemann, 2003.

[7] S. G. Kee, "Guide for conceptual helicopter design," Masters Degree, Monterey, California, Naval Postgraduate School, 1983. [Online]. Available: https://archive.org/details/guideforconceptu1094519825

[8] J. Stevens, J. Boer, W. Lammen, W. Vankan, and C. Sevin, "Helicopter pre-design strategy: design-to-mass or design-to-cost?," 2009. [Online]. Available: https://reports.nlr.nl/server/api/core/bitstreams/256c1718-e31c-48c8-91d6-e0e8c96cf184/content.

[9] J. Ilkko, J. Hoffren, and T. Siikonen, "Simulation of a helicopter rotor flow," *Rakenteiden mekaniikka,* vol. 44, pp. 186-205, 01/01 2011.

[10] DJI, "DJI Air2S," ed, 2022.

[11] J. G. Leishman, "Principles of Helicopter Aerodynamics," 2000.

[12] N. Atlas. "SOAPdrones variable pitch quadcopter uses petrol power for heavy-lifting endurance." New Atlas. https://newatlas.com/soapdrones-variable-pitch-multirotor-endurance/48202/ (accessed 2018-03-19.

[13] HEX. "Cube Orange Flight Control System." HEX. https://docs.px4.io/main/en/flight_controller/cubepilot_cube_orange.html (accessed 2023-02-15.

[14] A. R. S. Bramwell, D. Balmford, and G. Done, *Bramwell's Helicopter Dynamics*, 2 ed. Elsevier Science, 2001, p. 379.

[15] CATL. "CATL launches condensed battery with an energy density of up to 500 Wh/kg." https://www.catl.com/en/news/6015.html (accessed 2023-05-05).

[16] W. Cao, J. Zhang, and H. Li, "Batteries with high theoretical energy densities," *Energy Storage Materials,* vol. 26, pp. 46-55, 2020/04/01/ 2020, doi: https://doi.org/10.1016/j.ensm.2019.12.024.

[17] K. M. Abraham, "Prospects and Limits of Energy Storage in Batteries," *The Journal of Physical Chemistry Letters,* vol. 6(5), 830–844, 2015, doi: doi:10.1021/jz5026273

[18] R. C. Hibbeler, *Engineering Mechanics: Statics and Dynamics*. Pearson, 2015.

[19] A. Townsend, I. N. Jiya, C. Martinson, D. Bessarabov, and R. Gouws, "A comprehensive review of energy sources for unmanned aerial vehicles, their shortfalls and opportunities for improvements," *Heliyon,* vol. 6, no. 11, p. e05285, 2020/11/01/ 2020, doi: https://doi.org/10.1016/j.heliyon.2020.e05285.
[20] K. Mobariz, "Long endurance hybrid fuel cell-battery powered UAV," *World Journal of Modelling and Simulation,* vol. Vol. 11, no. No. 1, December 9 2014 2014. [Online]. Available: https://pdfs.semanticscholar.org/1828/.
[21] B. Coxworth. "Record-breaking hybrid quadcopter flies for over 10 hours." New Atlas. https://newatlas.com/drones/hybrix-hybrid-drone-10-hours/ (accessed 2020-01-10.
[22] N. Lavars. "Record-breaking hybrid drone stays aloft for over four hours." New Atlas. https://newatlas.com/quaternium-record-endurance-drone-flight/52758/?itm_source=newatlas&itm_medium=article-body (accessed 2018-08-24).
[23] J. Feist. "Gas powered drone – SOAPdrone's new idea with an old technology." Drone Rush. https://www.dronerush.com/gas-powered-drone-soapdrone-6600/ (accessed 2018-08-24).
[24] G. Aviation. "Griff 135." https://www.griffaviation.com/drones/griff-135/ (accessed 2022-10-03.
[25] F. Dragon, "Fly Dragon 20L AG," ed, 2020.
[26] W. Johnson, *Helicopter Theory*. Dover Publications, 1994.
[27] J. Seddon and S. Newman, *Basic Helicopter Aerodynamics: An Account of First Principles in the Fluid Mechanics and Flight Dynamics of the Single Rotor Helicopter*. Blackwell Science, 2002.
[28] S. Newman, "The Helicopter - Efficiency Or Efficacy?," *Aircraft Engineering and Aerospace Technology - AIRCRAFT ENG AEROSP TECHNOL,* vol. 78, pp. 15-19, 01/01 2006, doi: 10.1108/17488840610639636.
[29] I. C. Cheeseman, "The Effect of Ground the Helicopter Rotor in Forward Flight," Ministry Of Supply Aeronautical Research Council Reports And Memoranda, LONDON, 1955.
[30] H. H. Hurt, "Aerodynamics for Naval Aviators," ed, 1965.
[31] M. P. Bristeu P, "The Role of Propeller Aerodynamics in the Model of A Quadrotor UAV," 2009.
[32] T. Bingelis. "The Fixed Pitch Propeller Dilemma." EAA Sport Aviation. https://www.eaa.org/eaa/aircraft-building/builderresources/while-youre-building/building-articles/propellers-and-spinners/the-fixed-pitch-propeller-dilemma (accessed 2022-09-21.
[33] E. Kuantama, D. Craciun, I. Tarca, and R. Tarca, "Quadcopter Propeller Design and Performance Analysis," Cham, 2017: Springer International Publishing, in New Advances in Mechanisms, Mechanical Transmissions and Robotics, pp. 269-277.
[34] X. Wu, "Design And Development Of Variable Pitch Quadcopter For Long Endurance Flight," Master Of Science, Mechanical and Aerospace Engineering, Oklahoma State University, Stillwater, OK, 2018. [Online]. Available: https://core.ac.uk/download/pdf/215247607.pdf
[35] T. Pang, K. Peng, F. Lin, and B. M. Chen, *Towards Long-endurance Flight: Design and Implementation of a Variable-pitch Gasoline-engine Quadrotor*. 2017.
[36] A. Abhishek *et al.*, *Design, Development, and Closed-loop Flight-Testing of a Single Power Plant Variable Pitch Quadrotor Unmanned Air Vehicle*. 2017.

[37] M. J. Cutler, "Design and control of an autonomous variable-pitch quadrotor helicopter," S m, Massachusetts Institute of Technology, 2012. [Online]. Available: http://hdl.handle.net/1721.1/77106

[38] R. G. E. Al., "Design, Development, and Closed-loop Flight-Testing of a Single Power Plant Variable Pitch Quadrotor Unmanned Air Vehicle," 2017. [Online]. Available: https://www.researchgate.net/publication/317380103_Design_Development_and_Closed-loop_Flight-Testing_of_a_Single_Power_Plant_Variable_Pitch_Quadrotor_Unmanned_Air_Vehicle?enrichId=rgreq-73a1285dfbbd4402f6dca719eb220088-XXX&enrichSource=Y292ZXJQYWdlOzMxNzM4MDEwMztBUzo1MDI1NDA4NjczMDEzNzZAMTQ5NjgyNjQ4Nzk2Nw%3D%3D&el=1_x_2&_esc=publicationCoverPdf.

[39] M. Cutler and J. P. How, "Analysis and Control of a Variable-Pitch Quadrotor for Agile Flight," *Journal of Dynamic Systems, Measurement, and Control,* vol. 137, no. 10, 2015, doi: 10.1115/1.4030676.

[40] IOM. "International Organisation of Migration." https://unitedkingdom.iom.int/ (accessed 2018-11-15.

[41] N. S. The Telegraph, - UK, "Up to 90 migrants feared to have drowned off Libyan coast," ed: The Telegraph UK, 2018.

[42] T. Verge, "A drone has rescued two people from rough seas off the coast of Australia," ed: The Verge, 2018.

[43] S. Geek. "Eastern Aero Marine KSE-35 Aircraft Life Vest." http://www.skygeek.com/eastern-aero-marine-kse-35-life-vest.html (accessed 2018-05-01.

[44] S. K. Dehghan, "Migrant sea route to Italy is world's most lethal," ed: The Guardian, 2017.

[45] A. Seeni and P. Rajendran, "Analysis of Pressure Coefficient Around Three Airfoils Operating at Different Reynolds Number Using CFD and XFOIL," in *Proceedings of International Conference of Aerospace and Mechanical Engineering 2019*, Singapore, P. Rajendran, N. M. Mazlan, A. A. A. Rahman, N. M. Suhadis, N. A. Razak, and M. S. Z. Abidin, Eds., 2020: Springer Singapore, pp. 127-137.

[46] F. J. Bailey, Gustafson, F. B., "Charts for Estimation of the Characteristics of a Helicopter Rotor in Forward Flight. I -Profile Drag-Lift Ratio for Untwisted Rectangular Blades.," in "LangleyMemorialAermautical Langley Field,Va. Laboratory," 1944. [Online]. Available: https://digital.library.unt.edu/ark:/67531/metadc61833/m2/1/high_res_d/19930093083.pdf

[47] J. Morgado, R. Vizinho, M. A. R. Silvestre, and J. C. Páscoa, "XFOIL vs CFD performance predictions for high lift low Reynolds number airfoils," *Aerospace Science and Technology,* vol. 52, pp. 207-214, 2016/05/01/ 2016, doi: https://doi.org/10.1016/j.ast.2016.02.031.

[48] I. Berezin, P. Sarkar, and J. Malecki, "Fluid–Structure Interaction Simulation," in *Recent Progress in Flow Control for Practical Flows: Results of the STADYWICO and IMESCON Projects*, P. Doerffer, G. N. Barakos, and M. M. Luczak Eds. Cham: Springer International Publishing, 2017, pp. 263-281.

[49] M. Drela. "XFOIL." MIT. https://web.mit.edu/drela/Public/web/xfoil/ (accessed 2022-02-06).

[50] N. Ferry, "Quadcopter Plant Model and Control System Development With MATLAB Simulink Implementation," Master Of Science, Department Of Electrical

and Microelectronic Engineering, Rochester Institute of Technology, Rochester, New York, 2017.
[51] G. Carrillo, *Quad Rotorcraft Control. Vision-Based Hovering and Navigation*. 2012.
[52] M. Cavcar, "The international standard atmosphere (isa)," p. 7.
[53] T. Luukkonen, "Modelling And Control Of A Quadcopter," 2011. [Online]. Available: https://pdfs.semanticscholar.org/a3a8/dcfaae7afd971c24bd033fb0f7310e8fc741.pdf.
[54] *XFoil*. (1986). [Online]. Available: https://web.mit.edu/drela/Public/web/xfoil/
[55] B. V. R. Nielsen. Thesis_Project_Assets [Online] Available: https://drive.google.com/drive/folders/1EPPLc4FiMs0PDdWVSFS8WrZRImmxQbI6?usp=drive_link
[56] W. E. B. I. C. CHEESEMAN, "The Effect of Ground the Helicopter Rotor in Forward Flight," MINISTRY OF SUPPLY, AERONAUTICAL RESEARCH COUNCIL REPORTS AND MEMORANDA. , LONDON, 1955. [Online]. Available: https://reports.aerade.cranfield.ac.uk/bitstream/handle/1826.2/3590/arc-rm-3021.pdf?sequence=1&isAllowed=y
[57] J. Seddon, *Basic Helicopter Aerodynamics*. American Institute of Aeronautics and Astronautics, 1990.
[58] W. E. TW, "Hall Effect Base Linear Current Sensor." [Online]. Available: http://www.winson.com.tw/uploads/images/WCS1500.pdf
[59] M. Electronics. https://www.mauch-electronic.com/apps/webstore/products/show/6626809 (accessed.
[60] S. A. "WCS1500 Current Sensor Arduino Library " https://robojax.com/using-winson-wcs-hall-effec-current-sensor-arduino (accessed.
[61] MAUCH. "HS-200-HV." https://www.mauch-electronic.com/apps/webstore/products/show/6626809 (accessed 2021-01-14.
[62] APD. "APD 200-F3 ESC." https://shop.powerdrives.net/?product=200f3x (accessed 2022-05-28.
[63] MAVIN, "MAVIN NA50 Load Cell." [Online]. Available: https://www.ingelsoft.com/docs/mavin/mavin_NA5.pdf
[64] Sparkfun, *HX711 Load Cell Amplifier*. 2022.
[65] T-MOTOR. "T-MOTOR V10L " https://store.tmotor.com/goods.php?id=1112 (accessed 2022-04-27.
[66] J. R. Hendershot, *Design of Brushless Permanent-Magnet Machines*. 2010.
[67] S. Bell. "Analysis of a Rotor Blade System using Blade Element Momentum Theory." https://ww2.mathworks.cn/matlabcentral/fileexchange/21994-analysis-of-a-rotor-blade-system-using-blade-element-momentum-theory (accessed 2022-10-23.
[68] Spektrum, "iX12 12-Channel DSMX Transmitter Only," ed, 2023.
[69] AutomationPrimer, "PID Control," PIDControl, Ed., ed, 2013.
[70] MATLAB. "PID Tuner." https://www.mathworks.com/help/control/ref/pidtuner-app.html (accessed.

APPENDIX A: XFOIL LIFT & DRAG

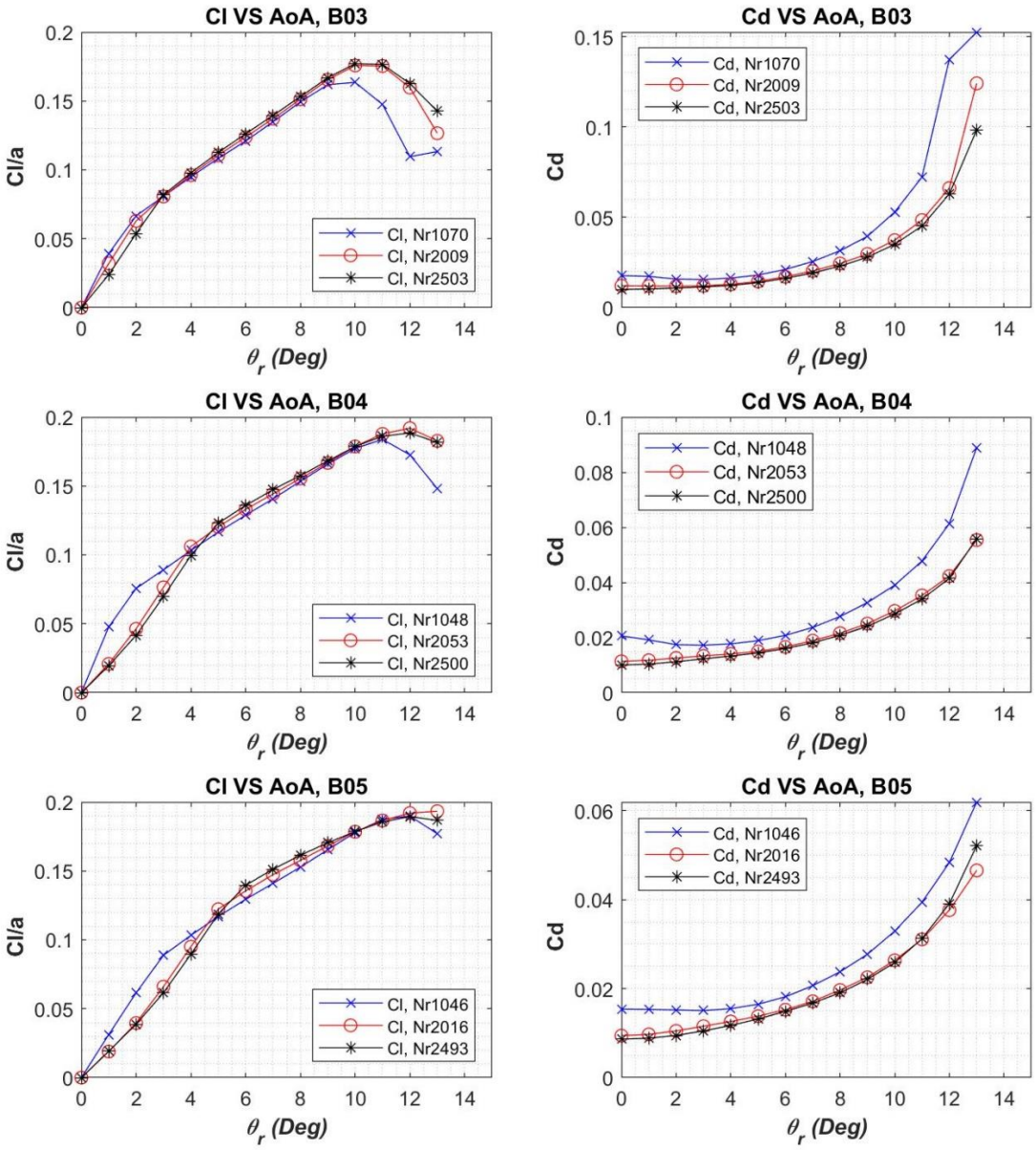

Figure 8.1: XFOIL Lift & Drag Polar Accumulation Plots

APPENDIX B: ROTOR PERFORMANCE COMPARISON, B03

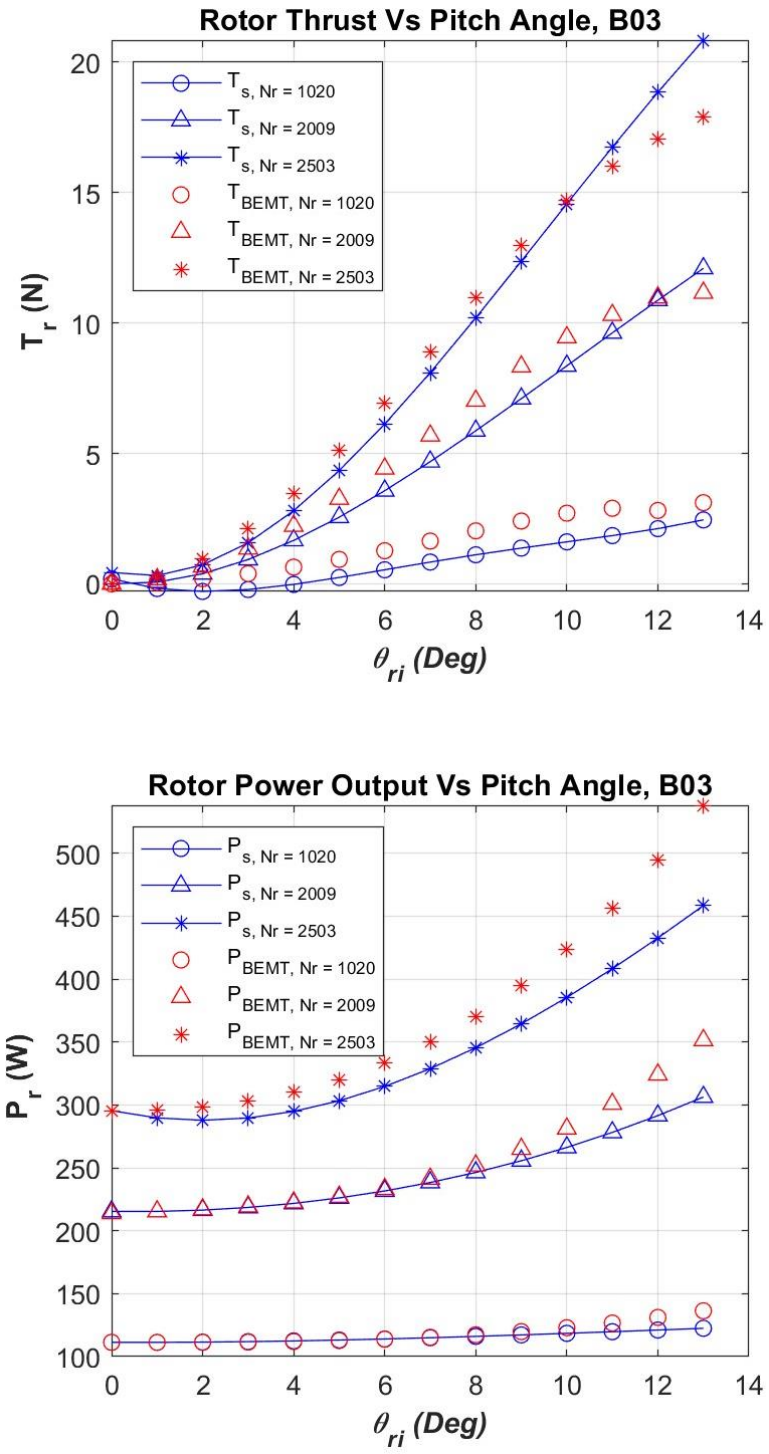

Figure 8.2: Rotor Performance Comparison, B03

APPENDIX C: ROTOR PERFORMANCE COMPARISON, B04

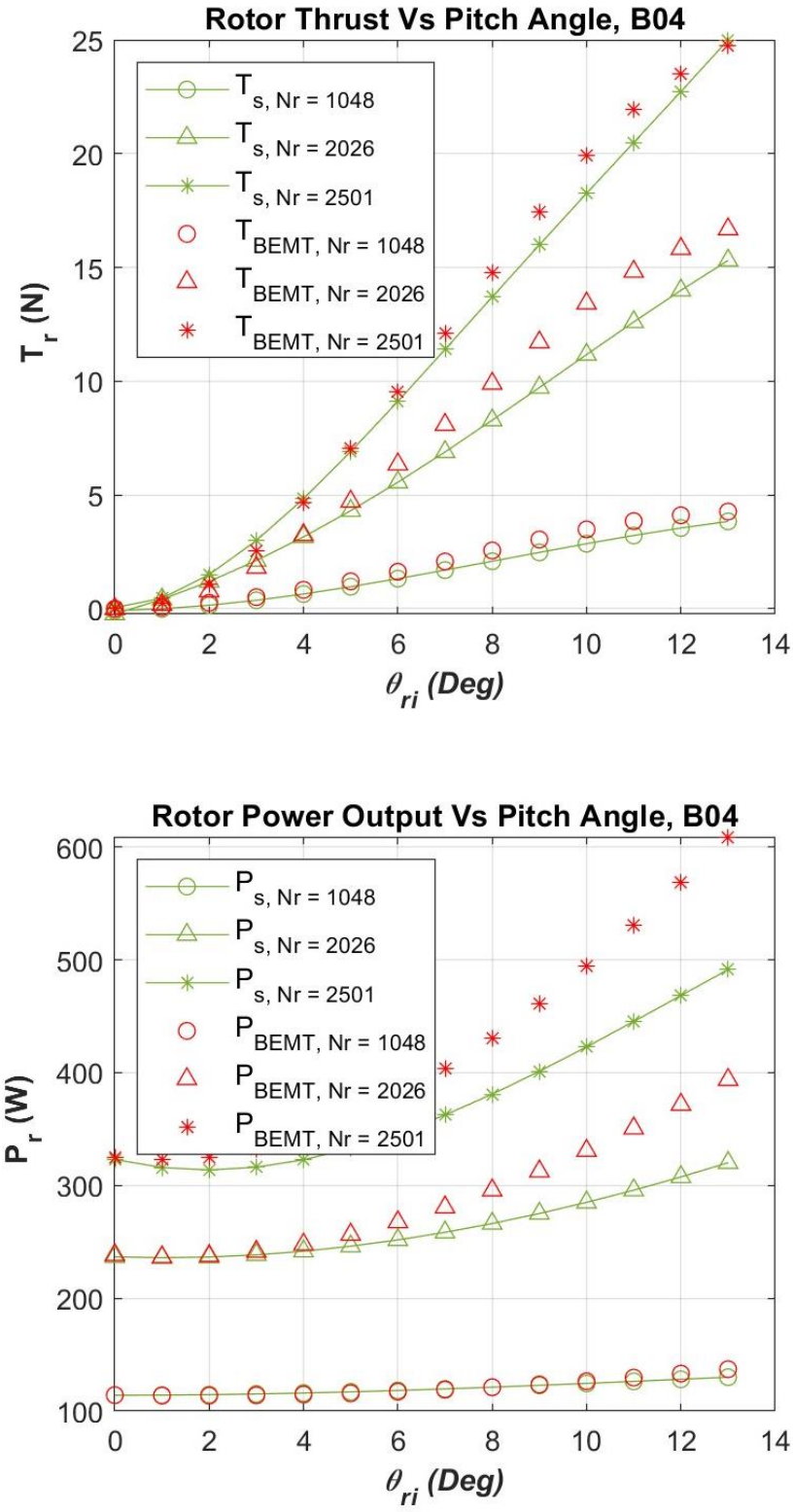

Figure 8.3: Rotor Performance Comparison, B04

APPENDIX F: DYNAMIC PERFORMANCE, TEST SCENARIO 2

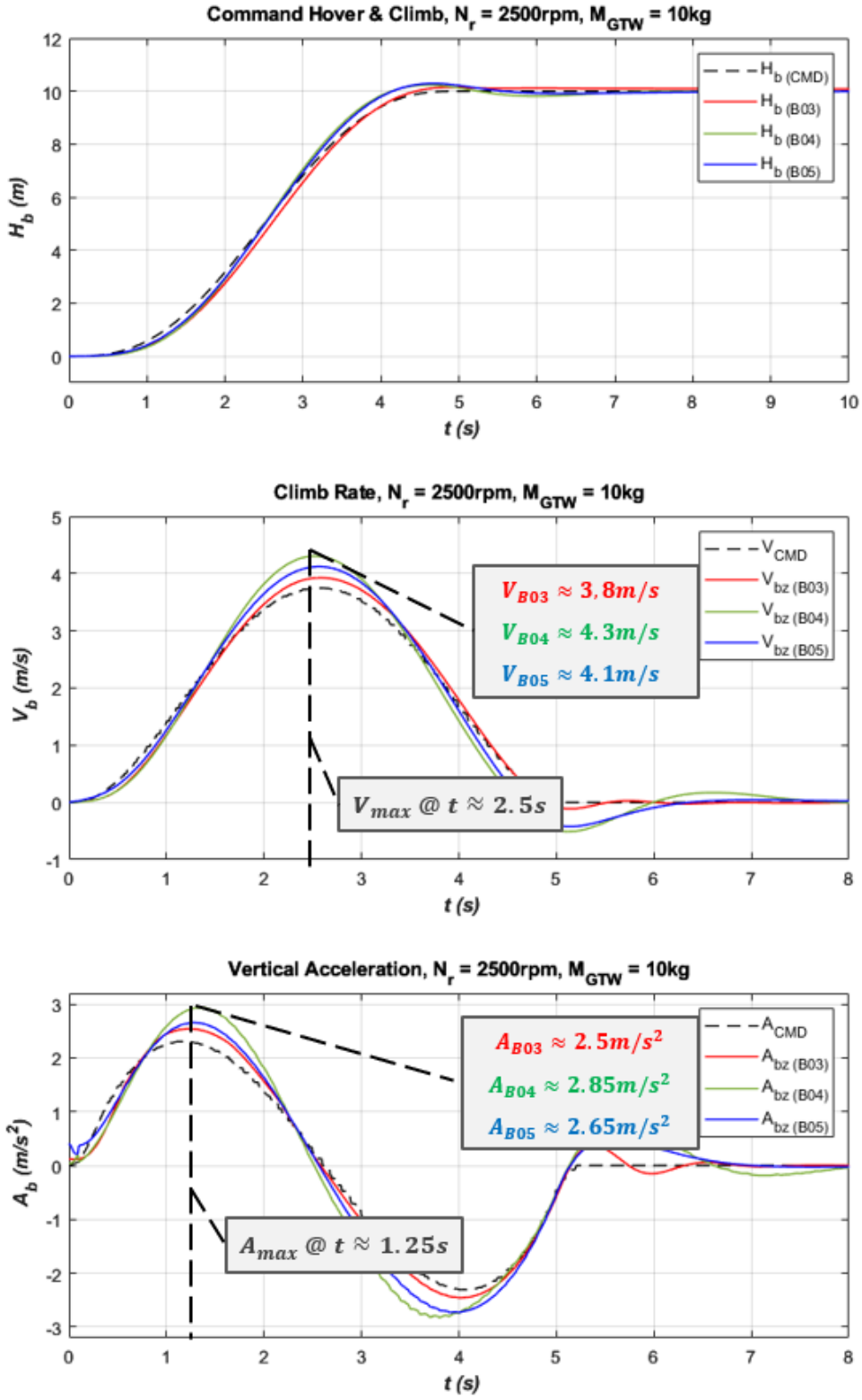

Figure 8.4: Dynamic Performance, Test Scenario 2

APPENDIX G: THRUST AND POWER OUTPUT, TEST SCENARIO 2

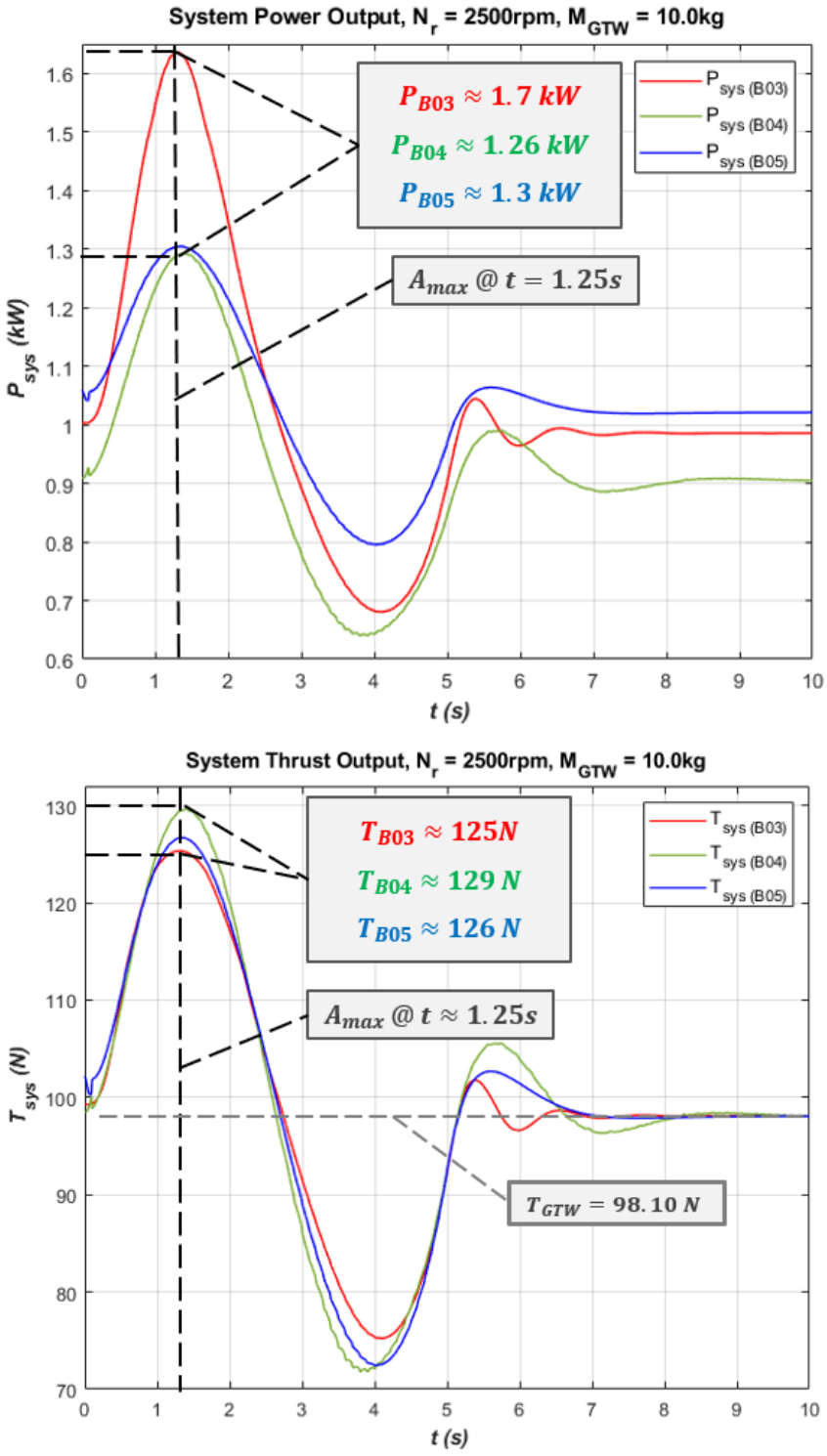

Figure 8.5: Thrust And Power Output, Test Scenario 2

APPENDIX H: POWER OUTPUT COMPARISON, TEST SCENARIO 2

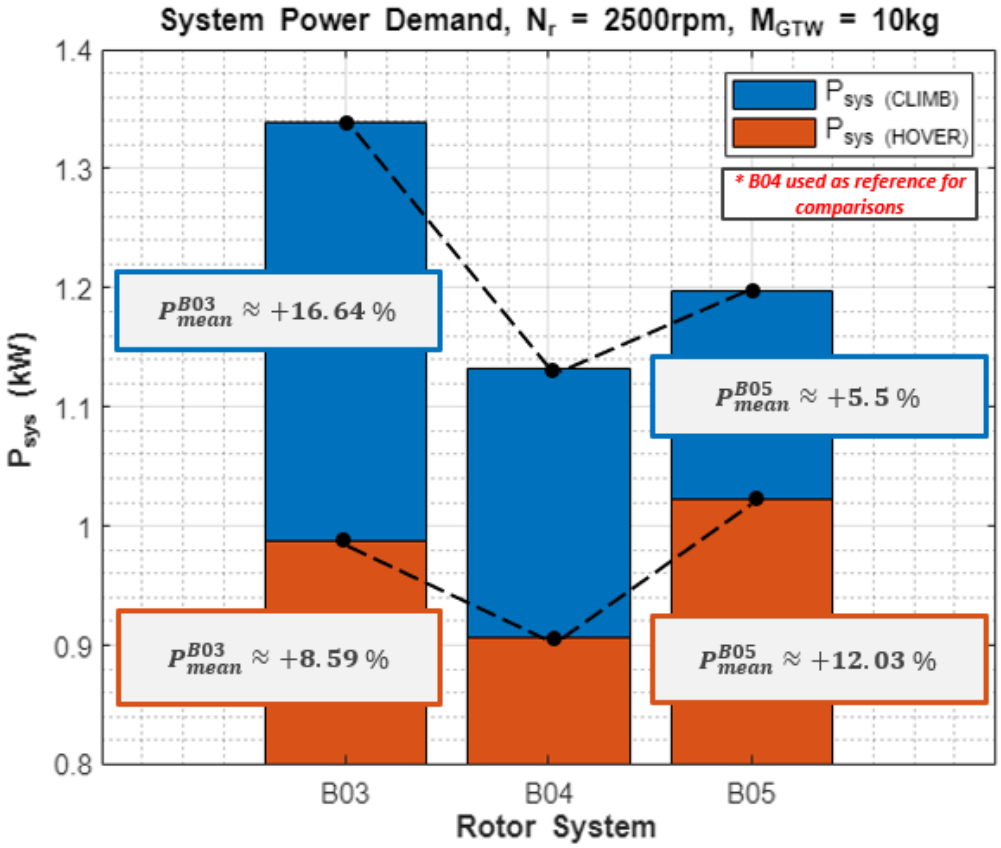

Figure 8.6: Power Output Comparison, Test Scenario 2

APPENDIX I: PROPERTIES OF ROTOR SYSTEMS CALCULATED IN SOLIDWORKS

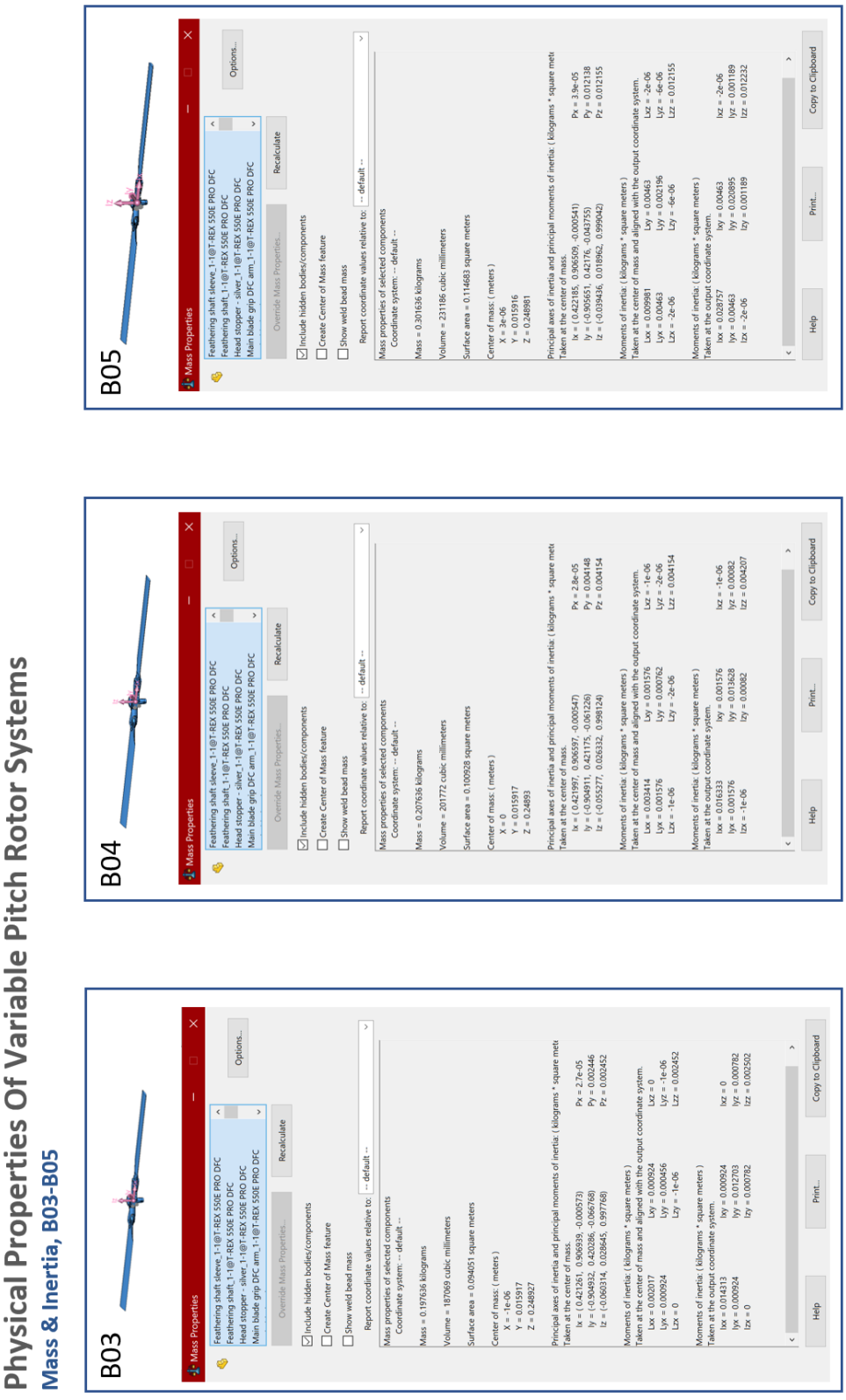

APPENDIX J: PROPERTIES OF AIRFRAMES CALCULATED IN SOLIDWORKS

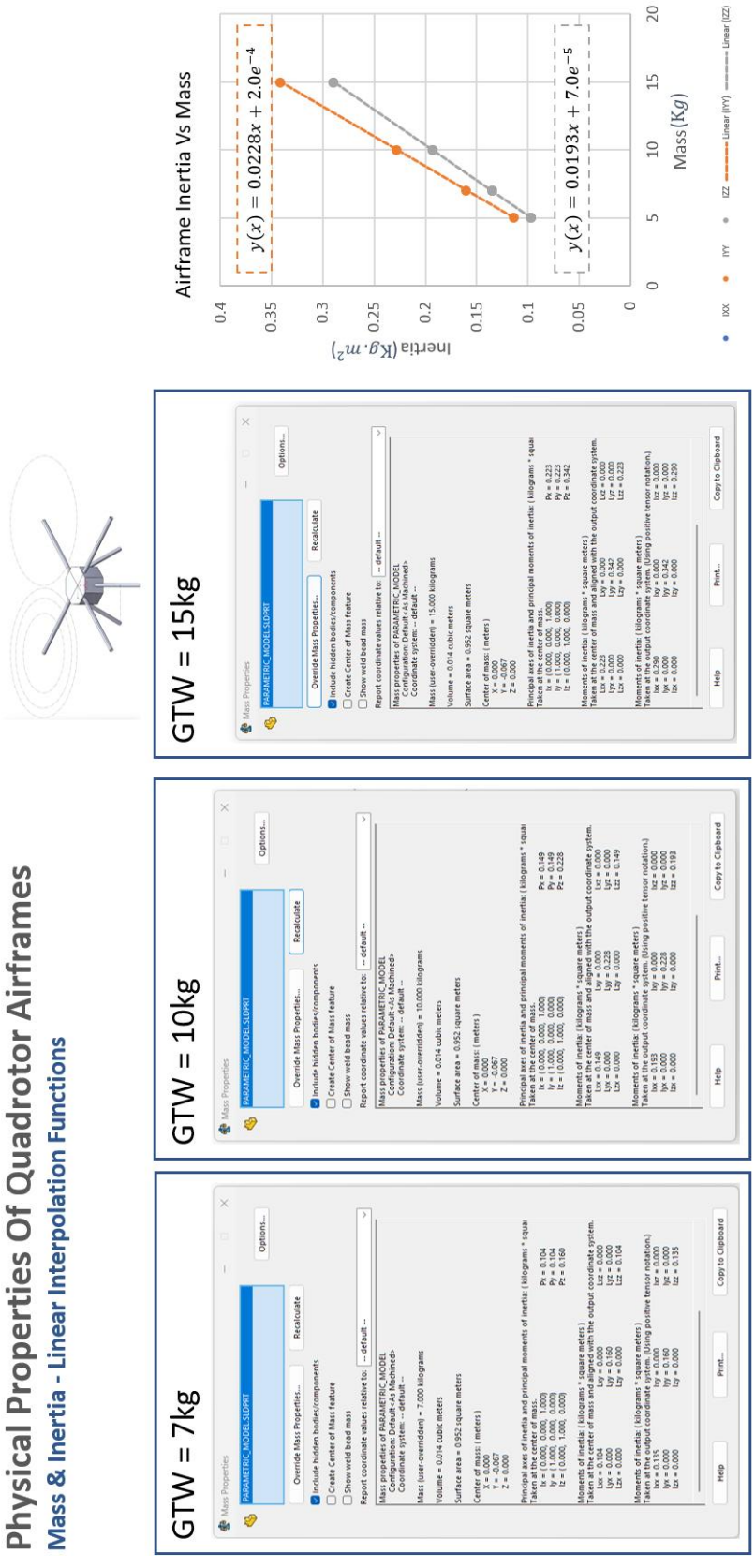

APPENDIX K: SIMULING PID AUTO-TUNER ILLUSTRATION